UNIVERSITY OF CALIFORNIA

Santa Barbara

Investigation of Morphology and Proton Conductivity in Proton Exchange Membranes under Variable Operating Conditions by Atomic Force Microscopy

A dissertation submitted in partial satisfaction of the

requirements for the degree Doctor of Philosophy

in Chemistry

by

Nicholas John Economou

Committee in charge:

Professor Steven K. Buratto, Chair

Professor Quyen Nguyen

Professor Craig Hawker

Professor Horia Metiu

December, 2014

The dissertation of Nicholas John Economou is approved.

_____

Prof. Quyen Nguyen

_____

Prof. Craig Hawker

_____

Prof. Horia Metiu

_____

Prof. Steven K. Buratto, Committee Chair

December, 2014

Investigation of Morphology and Proton Conductivity in Proton Exchange Membranes under Variable Operating Conditions by Atomic Force Microscopy

by

Nicholas John Economou

ACKNOWLEDGEMENTS

First and foremost I'd like to thank Steve Buratto, my advisor and mentor and without whom none of this would have been possible. Steve provided me with countless opportunities to expand my skills and pursue new projects as well as the freedom to explore whatever research avenues I was most interested in. This freedom made graduate school fun, exciting and rewarding and really allowed me to figure out on my own how to do good science. I also owe a lot to my senior graduate student, Jimmy O'Dea. Much of the work you are about to read about was based on some initial experiments done by him during his graduate work. He also passed on his expertise at AFM techniques and impressed on me his attention to detail and high standards for his data and the interpretation thereof. I'd also like to thank Jon Burk for being a great lab mate and an awesome friend. He was always great at cheering me up when I was in a crappy mood and was a good person to discuss ideas for experiments with. I'd like to thank my undergraduate students, Andrew Wheat and Thomas McConnaughy for their contributions to this research, as well as for the fun experience of being a mentor and getting to show others how to do research. I'd also like to thank the rest of the Buratto Group for being supportive, friendly, and just a general pleasure to work with and be around.

I'd like to thank Mrs. Scott, my high school chemistry teacher for introducing me to chemistry and making it exciting enough to keep an easily distracted high school student engaged. I'd also like to give thanks to my undergraduate advisor Dr.

Elizabeth Harbron for introducing me to research, getting me hooked on it and providing me with a path to UCSB. The experience in her research group gave me practice planning experiments, writing, and presenting, and really let me hit the ground running once I got here.

I'd like to thank my thesis committee; Craig Hawker, Horia Metiu, and Quyen Nguyen for the awesome guidance and helping me figure out the details of my project.

I'd also like to thank Syed Mubeen and Eric McFarland for coming to me and starting the collaboration on photoelectrochemical cells. It was a great treat to work on something a little outside of my area and broaden my experience. I'd also like to thank Mubeen for sharing his knowledge of semiconductor physics and for all the work he did making samples for me to characterize.

I'd like to the thank Than Do, Christian Bleiholder, Xueyun Zheng and Mike Bowers. This collaboration was extremely rewarding, and I hope that going forward it continues to bring many more exciting results.

I couldn't have done this without support from my family, my dad for getting me in to science at an early age and always being there to answer various questions about grad school and everything else. To my mom for always being sweet and checking up on me and making sure I didn't go crazy from the long hours in lab. To my brother Mike for always voicing his support, believing in me, and helping me stay positive. I'd also like to thank my grandmother Helen for her constant love and support even though I'm so far away.

I'd like to thank all of the graduate students who came on the Mammoth ski trips, those were a vital stress relief mechanism that helped me stay motivated over the long run. Similarly, I'd like to thank the intramural badminton team, especially Peter Chua, Sean Cheah, and Jon Napel, who have been there the whole time I've been at UCSB. I'd also like to thank my mountain biking friends, Ryan Kintz, Eric White, Baird King and Jon Hall for giving me yet another way to get outside and have fun after work. I'd like to thank Santa Barbara's small but loyal heavy metal scene and especially Leslie Castro for coming with me down to LA for the occasional show to let out some of the latent aggression that builds up over the course of grad school.

I'd also like to thank by friends back home, Andrew Bruss, Andy Reiner, Dan Goodman, Kate Parhiala, Serge Subach, Mike Pellegrini, Jon Nestico, Sasha Panasyuk and Jack Wolfe and anyone else I forgot. You guys were always great at checking in with me from afar, hanging out when we were all home for break, and just generally being extremely supportive. I'd also like to acknowledge all of the other friends, which are too many to name, that I've made over the course of graduate school that have been there to talk to in the hallways, at the bar, at the beach, over the internet and wherever else. You are all awesome and you made this grad school experience infinitely better through your presence. Thank you!

VITA OF NICHOLAS JOHN ECONOMOU

September 2014

EDUCATION

Bachelor of Science in Chemistry with High Honors, College of William and Mary, Williamsburg, Virginia, June 2008
Doctor of Philosophy in Chemistry, University of California, Santa Barbara, Expected September 2014

PROFESSIONAL EMPLOYMENT

Graduate Student Researcher, University of California, Santa Barbara, December 2009-Present

General Chemistry Laboratory Teaching Assistant, University of California, Santa Barbara, September 2009- June 2011

Undergraduate Student Researcher, College of William and Mary, June 2007- June 2008

Research Intern, Palomar Medical Technologies Incorporated, June 2006-September 2006

PUBLICATIONS

Economou, N. J.; Mubeen, S.; Buratto, S. K.; McFarland, E. W. Investigation of Arrays of Photosynthetically Active Heterostructures Using Conductive Probe Atomic Force Microscopy. Nano Lett. 2014.

Singh, N.; Upham, D. C.; Liu, R.-F.; Burk, J.; Economou, N.; Buratto, S.; Metiu, H.; McFarland, E. W. Investigation of the Active Sites of Rhodium Sulfide for Hydrogen Evolution/Oxidation Using Carbon Monoxide as a Probe. Langmuir 2014.

Economou, N. J.; O'Dea, J. R.; McConnaughy, T. B.; Buratto, S. K. Morphological Differences in Short Side Chain and Long Side Chain Perfluorosulfonic Acid Proton Exchange Membranes at Low and High Water Contents. RSC Adv. 2013, 3, 19525-19532

O'Dea, J. R.; Economou, N. J.; Buratto, S. K. Surface Morphology of Nafion at Hydrated and Dehydrated Conditions. Macromolecules 2013, 46, 2267–2274.

Do, T. D.; LaPointe, N. E.; Economou, N. J.; Buratto, S. K.; Feinstein, S. C.; Shea, J.-E.; Bowers, M. T. Effects of pH and Charge State on Peptide Assembly: The YVIFL Model System. J. Phys. Chem. B 2013, 117, 10759–10768.

Bleiholder, C.; Do, T. D.; Wu, C.; Economou, N. J.; Bernstein, S. S.; Buratto, S. K.; Shea, J.-E.; Bowers, M. T. Ion Mobility Spectrometry Reveals the Mechanism of Amyloid Formation of Aβ(25-35) and Its Modulation by Inhibitors at the Molecular Level: Epigallocatechin Gallate and Scyllo-inositol. J. Am. Chem. Soc. 2013, 45, 16926-16937

Do, T. D.; Economou, N. J.; LaPointe, N. E.; Kincannon, W. M.; Bleiholder, C.; Feinstein, S. C.; Teplow, D. B.; Buratto, S. K.; Bowers, M. T. Factors That Drive Peptide Assembly and Fibril Formation: Experimental and Theoretical Analysis of Sup35 NNQQNY Mutants. J. Phys. Chem. B 2013, 117, 8436–8446.

Harbron, E. J.; Davis, C. M.; Campbell, J. K.; Allred, R. M.; Kovary, M. T.; Economou, N. J. Photochromic Dye-Doped Conjugated Polymer Nanoparticles: Photomodulated Emission and Nanoenvironmental Characterization. J. Phys. Chem. C 2009, 113, 13707–13714.

Economou, N. J. Wheat, A. J. Hamrock, S. J. Schaberg, M.S. Buratto S. K. Atomic Force Microscopy Investigation of Nano-Scale Swelling Behavior in Multi Acid Sidechain Ionomers *In preparation*

Burk, J. J. Economou, N. J. Cooper, C. D. Rich, S. S. Majid S. S. Spin-Cast Thin Film Electrodes for Improved Performance in Proton Exchange Membrane Fuel Cells. Fuel Cells. *In preparation*

PRESENTATIONS

Economou, N. J. Morphological Differences in Short Side Chain and Long Side Chain Perfluorosulfonic Acid Proton Exchange Membranes at Low and High Water Contents. Oral. 246th Meeting of the American Chemical Society. Indianapolis
September 9, 2013

Economou, N. J. Understanding Fuel Cell Operation at the Nano-Scale Using Atomic Force Microscopy. Oral. Chemical Sciences Student Seminar. University Of California, Santa Barbara
November 30, 2012

AWARDS AND HONORS

National Science Foundation Graduate Research Fellowship, April 2011

Undergraduate Research Fellowship, June 2007

ABSTRACT

Investigation of Morphology and Proton Conductivity in Proton Exchange Membranes under Variable Operating Conditions by Atomic Force Microscopy

by

Nicholas John Economou

Nafion represents the most commonly employed and well characterized proton exchange membrane (PEM) used in fuel cells, however structural models which explain its physical properties are oversimplified and incomplete. In this work we use a combination of tapping mode and conductive probe (cp) Atomic Force Microscopy (AFM) to investigate the nanoscale morphology and proton conductivity of Nafion. By conducting imaging at a wide range of relative humidity, we were able to characterize Nafion from extensively dehydrated to liquid equilibrated states. Rather than an even swelling of hydrophilic clusters, we see an uneven dehydration of the surface at low hydration and a rearrangement to form a network of cylindrical inverted micelles at high water content. A statistical analysis of these features allowed us to match them with previous x-ray scattering data and develop a model of Nafion which is valid at large length scales and consistent over a wide range of water contents.

Comparison of this model system to new membrane materials has allowed us to better understand the structure-property relationship in these systems. We next investigated Hyflon, a short side chain analog of Nafion and found that in contrast to Nafion it is able to swell reversibly through a dilation and contraction of hydrophilic clusters with minimal rearrangement and retain more hydrophilic character at the surface at dehydrated conditions. Investigation of new multi-acid sidechain membranes was also conducted and showed that while these membranes have excellent water retention and proton conductivity, they swell and form a continuous hydrophilic phase at the surface which may be problematic during fuel cell operation. In addition to these characterization efforts, a number of advances to the cp-AFM technique were demonstrated which allowed for the investigation of new operating conditions and the extraction of new information on electrical and mechanical properties of the membrane.

TABLE OF CONTENTS

Chapter 1: Introduction

1.1 Introduction to Proton Exchange Membrane Fuel Cells

Fuel Cells are versatile power sources which convert chemical energy in the form of an energy-rich fuel molecule into electrical energy which can used to power a variety of devices. Fuel cells have the inherent advantages of high chemical to electrical efficiency relative to internal combustion engines, environmentally benign byproducts, low noise, no moving parts, and potentially low operating temperatures. There are several different types of fuel cells, which are differentiated by the type of electrolyte employed. Solid oxide fuel cells (SOFC's) utilize an inorganic electrolyte and are operated at higher temperatures, making them ideal for stationary power generation. Alkaline fuel cells (AFC's) use a liquid potassium hydroxide solution as an electrolyte and are thus suited best for stationary applications where weight and volume are less of an issue. Proton exchange membrane fuel cells (PEMFC's), the subject of this work, use a solid polymer as an electrolyte and operate at lower temperature. This solid electrolyte allows for a compact, lightweight and mechanically rigid cell which makes it ideal for automotive and portable device applications.

This type of cell was first developed by General Electric in the 1960's,[1] it was then adopted as the power source for the NASA Gemini spacecraft. Due to their high expense, these systems were only used in niche applications. It was not until the late 1980's and early 1990's that PEM fuel cell research made large strides in reducing costs and pushing this systems towards large scale commercial viability. These were accomplished primarily from the reduction of platinum loading, from several milligrams per square centimeter down to ~0.4 mg/cm^2.[2,3] Despite the progress that has been made in this regard, PEM fuel cells are still not cost-competitive with many other technologies, and further research and development is necessary to achieve this end.[4–6]

These solid polymer electrolytes have a unique chemical structure which provides them with excellent physical properties for fuel cell operation. PEM's are almost exclusively random and block copolymers which consist of a rigid hydrophobic block paired with a hydrophilic block which contains an acidic functionality, these are often referred to as ionomers due to their ionic character. Phase separation during membrane casting causes the formation of a hydrophilic ion conducting phase inside of a rigid polymer matrix, imparting good mechanical strength and high cationic conductivity. The most commonly employed and most studied polymer is Nafion ®, a perfluorosulfonic acid (PFSA) polymer trademarked by DuPont. This polymer consists of a Teflon-like fluorocarbon backbone which provides the hydrophobic block and a sulfonic acid sidechain which in combination with absorbed water forms the ion conducting phase. Most other membranes also use

sulfonic acid groups as a proton conducting moiety, but a number of different polymer backbones exist. To date PFSA type membranes are the best performing systems, though there is continued research interest in developing PEM's with hydrocarbon backbones.[7]

Inside of a fuel cell, Nafion or another PEM is pressed between two carbon gas diffusion electrodes forming a membrane electrode assembly (MEA). The outermost layer of these electrodes is the gas diffusion layer (GDL), which allows for reactant gases to flow to the catalytically active regions of the cell and whose hydrophobic nature aids in simultaneously removing water and preventing flooding. Painted on the GDL is the microporous layer, a conductive layer of porous carbon and polymeric binding agent such as Teflon. On top of this is the catalyst layer, another layer of conductive carbon which contains platinum nanoparticles which catalyze the hydrogen oxidation reaction at the anode and the oxygen reduction reaction at the cathode.

Hydrogen Oxidation Reaction	$2H_2 \longrightarrow 4H^+ + 4e^-$	$E^0 = 0\,V_{SHE}$
Oxygen Reduction Reaction	$O_2 + 4H^+ + 4e^- \longrightarrow 2H_2O$	$E^0 = 1.229\,V_{SHE}$
Net	$\boldsymbol{2H_2 + O_2 \longrightarrow 2H_2O}$	$E^0 = 1.229\,V_{SHE}$

Figure 1.1: Electrochemical reactions of a PEM fuel cell.

The catalyst layer also contains Nafion or another ionomer which allows for ionic conductivity in addition to the electrical conductivity provided by the carbon. The catalyst layer composition is crucial, as it must simultaneously allow for reactant gases to diffuse to the platinum catalyst as well as provide a pathway for electrons to reach the catalyst and for ions to reach the PEM. This 3-phase reaction zone is crucial for cell operation, and a large number of studies have focused on the design and optimization of catalyst layers in order to increase efficiency of the cell.

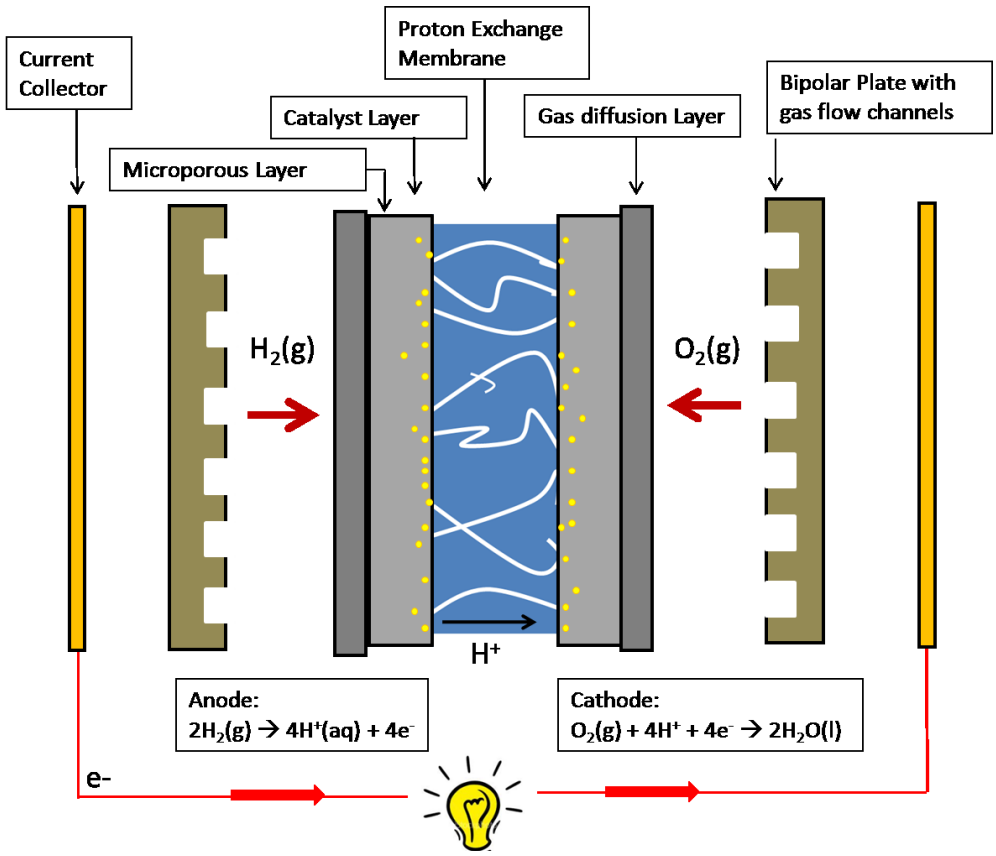

Figure 1.2: Schematic representation of a cross section of an operating PEM fuel cell.

The MEA is placed inside of a cell enclosure where graphite bipolar plates are placed on either side which contain gas flow channels which introduce fuel (hydrogen) and oxidant (air or oxygen) to the gas diffusion layer. Hydrogen is oxidized in the anode catalyst layer, forming protons which are then conducted through the PEM. At the same time, the high acidity of the PEM inhibits anionic conductivity and forces the free electrons generated in this reaction through an external current collector where they can be used to power the device. At the cathode side, the oxidant is introduced where it recombines with hydrogen and electrons to form water. The use of gaseous fuel and oxidant allows for good gravimetric energy density, and the formation of water as the sole byproduct makes these systems attractive from an environmental perspective. Additionally, these electrochemical reactions represent a direct chemical to electrical pathway, and have a much higher thermodynamic efficiency than internal combustion engines.

Current collecting plates sit outside of the bipolar plates and allow for power to be extracted from the system. In most fuel cell systems, several MEA's are connected in parallel or in series in order to meet the current and voltage needs of the application. The result is an extremely versatile and lightweight power source that can be tailored to applications ranging from small portable electronics to large, stationary power generation for buildings.

These two half reactions provide a theoretical voltage of 1.229 V relative to the standard hydrogen electrode, which is reduced to 1.19 V in the presence of water at

typical cell operating conditions. This is further reduced by various resistances inside of the cell which lower the actual voltage further from its ideal value. Fuel cell performance is generally represented as a polarization curve where the cell is run under a variable load while the voltage is measured. At low currents, activation losses occur due to the activation potential required for both half reactions. At moderate currents, ohmic losses occur due to resistance to proton transport through the cell, a large contributing factor to these losses is the resistance of the PEM itself. Finally, at high currents, mass transport losses occur due to reactants being consumed more quickly than they can be resupplied at the catalyst.

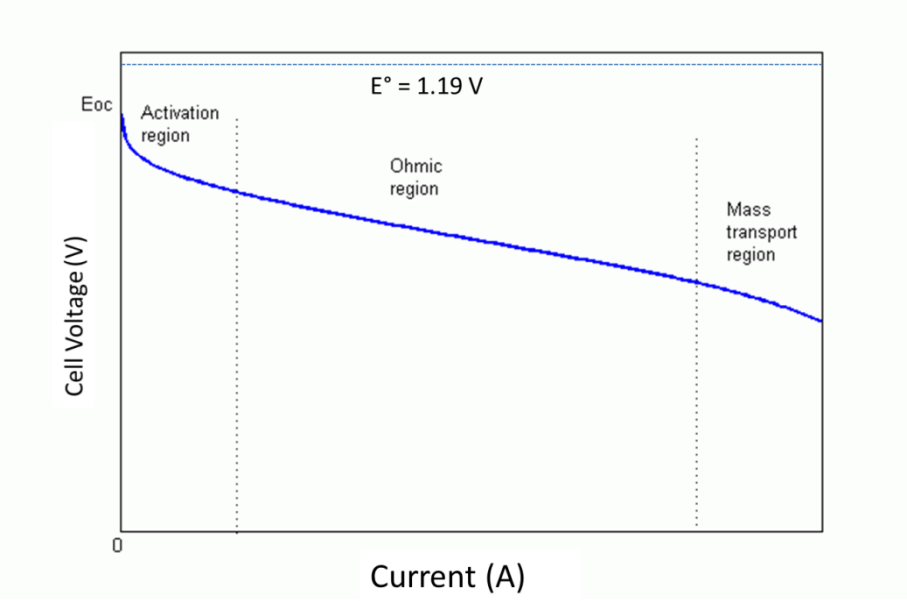

Figure 1.3: Typical Polarization curve for a PEM fuel cell, showing voltage losses which occur during cell operation.

As a result, much of the efforts geared towards improving the performance of fuel cells have involved lowering the resistance of various components, most notably

the membrane, as well as improving electrode structure to allow for better transport of reactants. These efforts will be discussed in greater detail in the following section.

1.2 Challenges to PEM commercialization

The first and foremost challenge to the widespread adoption of PEMFC's is the overall system cost of the cell; they are still more expensive per kW of power than an internal combustion engine. Due to various improvements in cell design and the manufacturing of components, the cost has decreased rapidly in the past 10 years and is now on the verge of becoming cost competitive. The ultimate target to compete with an internal combustion engine is $30 per kW, and the current state of the art fuel cells are about $55 per kW based on a production volume of 500,000 units.

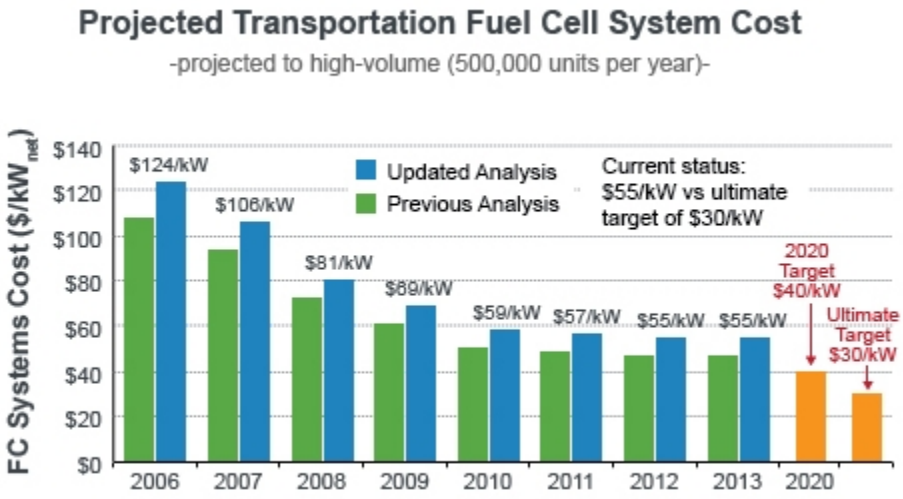

Figure 1.4: Projected system cost per kW of a commercial fuel cell system, given fixed production volume. Calculated by the US department of energy fuel cell program.

Despite the promise inherent in PEMFC's, there remain a number of challenges to be solved before these systems can become commercially adopted on a wide scale. The US department of energy (DOE) has conducted extensive efforts towards decreasing the cost of fuel cells[8] and has targeted a number of areas such as creating new membrane materials, reducing platinum loading and creating new hydrogen storage systems.

One of the largest hurdles for PEMFC technology is the use of precious metal catalysts (generally platinum and platinum/ruthenium) at the anode and cathode respectively. These make up a large percentage of the cost of a fuel cell; up to 40% depending on the application and production volume.[9] In addition to being expensive, these catalysts are extremely scarce, and there is likely not enough of them on the planet to power billions of fuel cells on top of its existing uses. A major improvement to electrodes was achieved by using thin film catalyst layers which effectively localize platinum where it is utilized most efficiently and decreases the loading to a few hundred micrograms of platinum per centimeter of cell active area.[2,3] Optimization of the platinum particle size to maximize catalytically active surface area have also allowed great reductions in loading to be achieved. However, even with these improvements, it is unlikely that the use of platinum on such large scales would be possible.[10] As a result there is great interest in developing new non-precious metal catalysts which can catalyze the HOR and ORR.[11–14]

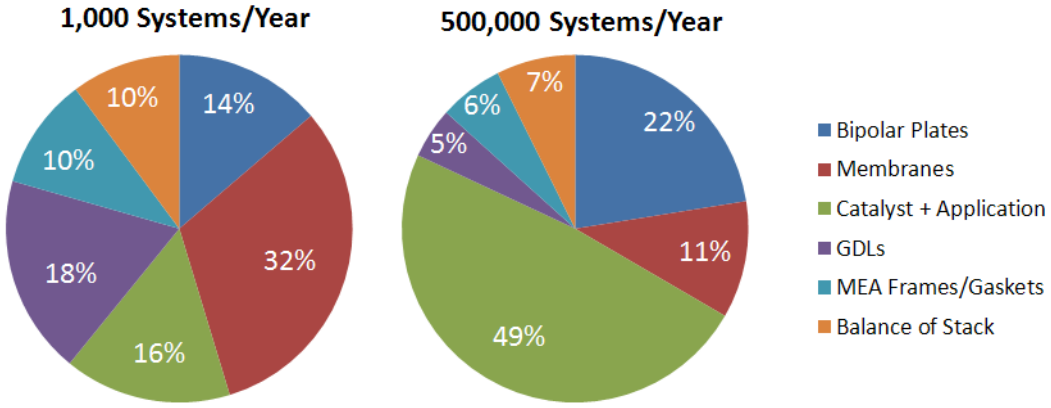

Figure 1.5: Predicted cost breakdown of a commercial PEM fuel cell system by component at different production volumes. From the 2013 DOE Fuel Cell Systems Cost Report.

Another set of technical challenges arises in regard to the production and storage of hydrogen for fuel cell systems. While extremely light, hydrogen is difficult to compress and achieve acceptable volumetric energy density for the entire system. A number of approaches have been taken to address this such as using compounds which can reversibly bind hydrogen gas in order to occupy a smaller volume.[13,14]

Hydrogen production poses another interesting question, as the current source of hydrogen is largely from the reforming of fossil fuels. Reforming creates carbon monoxide which is very difficult and expensive to separate from the hydrogen produced and can bind to platinum. This "CO poisoning" reduces available catalyst sites and decreases performance. The environmental impact of this technique is also dependent on continued use of fossil fuels, and as such numerous systems to generate hydrogen from renewable sources, e.g. photoelectrolysis of water are under development.[15,16]

The PEM itself also poses a number of unique challenges regarding cell cost and cell durability, and the focus of this work is on identifying routes to improve upon these factors. Fluorinated polymers such as Nafion are expensive to produce and while costs of membrane fabrication decrease greatly with scaling up, there is interest in investigating alternative PEM systems.[7] Additionally, Nafion and other PEM's suffer from having a proton conductivity which is heavily dependent on water content. If water is removed from the membrane, proton conductivity decreases drastically. This necessitates the use of humidified gas feeds and effective water management inside of the cell to prevent dehydration. There is great interest in developing membranes which can maintain proton conductivity under dry conditions as this would greatly reduce the size and complexity of the entire system. Such a membrane would also allow for higher temperature operation which carries with it a number of important performance advantages. These include increased proton conductivity at high temperature, reduced CO poisoning when using reformed fuels, improved ORR kinetics at the cathode,[17,18] and better heat ejection from the cell. The DOE target temperature is 120° C as it allows for significant improvements in all of these areas. A number of cell design approaches have been explored in order to allow membranes to retain water at high temperature and realize these benefits.[19,20]

In addition to being able to retain water, membranes need to be stable to a humid environment, and many membranes which show good water retention suffer from excessive swelling at high water contents. The ideal membrane will undergo minimal swelling across a wide range of water contents, allowing the cell to operate stably

across variable operating conditions. Many different techniques have been used to stabilize existing PEM polymers, such as forming inorganic composites,[21–23] reinforcing with Teflon fiber,[24] and using cross-linkable membranes.[25,26] However, there is still much room for improvement in these materials in regard to simultaneously achieving high proton conductivity and high mechanical stability.

The PEM is a performance limiting component of any fuel cell system, and for this reason a large amount of research has been devoted to understanding the physical properties of these materials such as mechanical strength and ionic conductivity.[27] All of these properties are intimately tied to the nanoscale morphology of these systems caused by the phase separation of hydrophilic and hydrophobic segments of polymer which makes the accurate determination of this structure a valuable research goal in and of itself. All of these properties are crucial to cell operation and often are dependent on hydration, and a detailed understanding of how and why this variation occurs is important for improving existing fuel cell systems. In this thesis we employ Atomic Force Microscopy as a tool to contribute to these efforts and investigate the nanoscale morphology and electrochemical properties of various PEM's as a function of water content.

1.3 Atomic Force Microscopy as a Polymer Characterization Tool

Atomic Force Microscopy (AFM) was first demonstrated in 1986 at IBM laboratories[28], with much of the early work being done at Stanford[29] UC Santa Barbara[30]. Since its inception, AFM has been used to characterize a wide variety of

samples on the nanometer scale. In this technique an extremely sharp silicon probe which protrudes from a silicon "cantilever" or "chip" is used to effectively "feel" the sample and generate a topographic map of the surface. A laser is focused on the back side of the tip which is then reflected to a photodiode where the deflection of the laser spot is recorded. The tip is then raster scanned in the *x* and *y* direction to generate an image while a piezoelectric actuator above the tip raises and lowers the tip in response to the feedback from the detector. While there are a huge range of AFM techniques that can be used, they can be generally separated into contact mode and tapping mode (also referred to as AC-mode or AM-mode.) In contact mode, the tip is brought into physical contact with the surface. Then, during scanning, the deflection of the laser spot is used as the feedback mechanism, and the z-piezo raises and lowers during scanning to maintain a constant deflection. While there are certain advantages to contact mode, it generally involves large tip-sample contact forces and can result in the damaging of the tip or sample.

Tapping mode AFM is conducted by using a piezoelectric actuator to oscillate the AFM cantilever at its resonant frequency and bringing into "intermittent contact" with the sample. This technique was first developed by digital instruments in 1993, and led to an increased interest in AFM as a characterization tool for soft materials.[31] When the tip is brought close to the sample, the amplitude of the cantilever oscillation is damped by both attractive, long range forces and repulsive short range forces. This damped amplitude is used as the feedback mechanism and the z-piezo then moves the AFM tip up and down in order to maintain constant amplitude. This

technique has the advantage of extremely low contact force with the sample, minimal lateral forces during scanning, and high resolution relative to contact mode. This makes it ideal for imaging soft polymer and biological samples where sample damage is an issue.

Another advantage to using AC-mode AFM is that in addition to the amplitude of the cantilever oscillation, the phase of this oscillation can also be monitored. This phase signal gives information about the nature of the interaction between the AFM tip and the sample. Specifically, the phase signal can be directly related to the power dissipated during the tip-sample interaction[32]. The mathematical relationship is shown below, and requires the assumption that a high quality factor cantilever is being operated in a non-damping environment.

$$P_{tip-sample} = \frac{1}{2}\frac{kA^2\omega_0}{Q}\left[\left(\frac{A_0}{A}\right)\sin\varphi - 1\right]$$

k = cantilever spring constant (N/m)
A = amplitude of cantilever interacting with sample
ω_o = cantilever frequency of oscillation
A_o= amplitude of freely oscillating cantilever
Q = cantilever quality factor
φ = phase angle

Figure 1.6: Equation relating the phase angle of the cantilever oscillation to the power dissipated during contact.

The result is that contrast can be achieved between softer and harder areas of the sample. This makes it extremely useful for characterizing copolymers, polymer blends, and biological systems where differences in stiffness are important for assigning the identity of various components. The lateral resolution of all AFM techniques is dependent on the geometry of the AFM tip, but in AC-mode with a sharp, commercially available silicon tip, resolution of single nanometer lengths is routinely possible. In this work we employ AC-mode AFM to resolve the hydrophilic and hydrophobic segments of PEM's which have sizes on the order of 5 nm.

In addition to revealing information about the topography and mechanical properties, AFM is an effective technique for probing the electrical properties of a variety of samples. Numerous imaging modes exist which operate in either tapping or contact mode and supply spatially resolved electrical measurements. These include conductive AFM, scanning kelvin probe microscopy, electrostatic force microscopy, scanning capacitance microscopy, and investigate conductivity, surface potential, surface charge, and capacitance respectively. For an in-depth review of these techniques the reader is directed to the following review article.[33] Conductive AFM remains the only technique capable of measuring the conductivity of materials on the nanometer scale, and is employed here to investigate proton conductivity in various PEM's.

Conductive AFM has been used previously to characterize conducting and semiconducting samples such as carbon nanotubes[34], inorganic semiconductors[35],

organic semiconductors[36] and conductive biomolecules.[37] With electrically conductive samples, this technique is straightforward, and current is measured directly through the tip at conductive regions of the sample. In the case of PEMFC's a property of key import is the proton conductivity of the membrane, and because these membrane are electronically insulating, conventional conductive AFM cannot be employed. For this reason, our group has developed a variant of this technique which we call conductive probe AFM (cp-AFM).[38] In this technique, we attach the PEM to a commercial fuel cell electrode which acts as the anode catalyst layer. We then supply hydrogen at the anode and supply air at the tip while scanning, which allows us to measure through-membrane proton current directly. The result is that we have a half fuel cell where the tips acts as a nanoscale moving cathode. Similar techniques have also been employed by other research groups and have demonstrated the ability to measure spatially resolved proton conductivity in these materials. [39–41]

The goal of this work is to utilize tapping mode and conductive probe AFM to investigate the phase-separated morphology and proton conductivity of PEM's under varying relative humidity operating conditions. This began by developing these techniques on Nafion; a well characterized model system, and then expanding them to various new polymers which are either under development or are commercially available. Through these studies, we developed a detailed structure-property relationship of these systems and were able to discern structural factors which can lead to improved performance. We also worked to expand the capabilities of cp-AFM by expanding it to new ranges of operating conditions, using it to image proton

conductivity inside of the catalyst layer and by using various techniques to increase spatial resolution and obtain quantitatively accurate current readings. Lastly, we conducted experiments aimed at optimizing the composition of the catalyst layers for PEMFC's in order to better understand platinum utilization and develop electrodes with reduced loading and higher performance. All of these efforts are geared towards gaining a better understanding of nanoscale properties of fuel cell materials and their effect on the performance of the cell. It is our hope that this understanding can lead to the design of new, higher performing membranes and electrodes for PEMFC's.

References

(1) Grubb, W.; Niedrach, L. Batteries with Solid Ion-Exchange Membrane Electrolytes .2. Low-Temperature Hydrogen-Oxygen Fuel Cells. *J. Electrochem. Soc.* **1960**, *107*, 131–135.

(2) Wilson, M.; Gottesfeld, S. Thin-Film Catalyst Layers for Polymer Electrolyte Fuel-Cell Electrodes. *J. Appl. Electrochem.* **1992**, *22*, 1–7.

(3) Wilson, M.; Valerio, J.; Gottesfeld, S. Low Platinum Loading Electrodes for Polymer Electrolyte Fuel-Cells Fabricated Using Thermoplastic Ionomers. *Electrochim. Acta* **1995**, *40*, 355–363.

(4) Mock, P.; Schmid, S. A. Fuel Cells for Automotive Powertrains-A Techno-Economic Assessment. *J. Power Sources* **2009**, *190*, 133–140.

(5) Bar-On, I.; Kirchain, R.; Roth, R. Technical Cost Analysis for PEM Fuel Cells. *J. Power Sources* **2002**, *109*, 71–75.

(6) Lipman, T. E.; Edwards, J. L.; Kammen, D. M. Fuel Cell System Economics: Comparing the Costs of Generating Power with Stationary and Motor Vehicle PEM Fuel Cell Systems. *Energy Policy* **2004**, *32*, 101–125.

(7) Hickner, M. A.; Ghassemi, H.; Kim, Y. S.; Einsla, B. R.; McGrath, J. E. Alternative Polymer Systems for Proton Exchange Membranes (PEMs). *Chemical Reviews* **2004**, *104*, 4587–4612.

(8) Epping Martin, K.; Kopasz, J. P. The U.S. DOEs High Temperature Membrane Effort. *Fuel Cells* **2009**, *9*, 356–362.

(9) DOE Fuel Cell Technologies Office Record 13012: Fuel Cell System Cost - 2013 - 13012_fuel_cell_system_cost_2013.pdf.

(10) Two Fuel Cell Cars in Every Garage? *Electrochem. Soc. Interface (USA)* **2005**, *14*, 24–3535.

(11) Chen, Z.; Higgins, D.; Yu, A.; Zhang, L.; Zhang, J. A Review on Non-Precious Metal Electrocatalysts for PEM Fuel Cells. *Energy Environ. Sci.* **2011**, *4*, 3167–3192.

(12) Feng, Y.; Alonso-Vante, N. Nonprecious Metal Catalysts for the Molecular Oxygen-Reduction Reaction. *Phys. Status Solidi B-Basic Solid State Phys.* **2008**, *245*, 1792–1806.

(13) Liu, G.; Li, X.; Ganesan, P.; Popov, B. N. Development of Non-Precious Metal Oxygen-Reduction Catalysts for PEM Fuel Cells Based on N-Doped Ordered Porous Carbon. *Applied Catalysis B: Environmental* **2009**, *93*, 156–165.

(14) Wood, T. E.; Tan, Z.; Schmoeckel, A. K.; O'Neill, D.; Atanasoski, R. Non-Precious Metal Oxygen Reduction Catalyst for PEM Fuel Cells Based on Nitroaniline Precursor. *J. Power Sources* **2008**, *178*, 510–516.

(15) Kudo, A.; Miseki, Y. Heterogeneous Photocatalyst Materials for Water Splitting. *Chem. Soc. Rev.* **2009**, *38*, 253–278.

(16) Bak, T.; Nowotny, J.; Rekas, M.; Sorrell, C. C. Photo-Electrochemical Hydrogen Generation from Water Using Solar Energy. Materials-Related Aspects. *Int. J. Hydrog. Energy* **2002**, *27*, 991–1022.

(17) Liu, Y.; Murphy, M. W.; Baker, D. R.; Gu, W.; Ji, C.; Jorne, J.; Gasteiger, H. A. Proton Conduction and Oxygen Reduction Kinetics in PEM Fuel Cell Cathodes: Effects of Ionomer-to-Carbon Ratio and Relative Humidity. *J. Electrochem. Soc.* **2009**, *156*, B970–B980.

(18) Parthasarathy, A.; Srinivasan, S.; Appleby, A. J.; Martin, C. R. Temperature Dependence of the Electrode Kinetics of Oxygen Reduction at the Platinum/Nafion[registered Sign] Interface---A Microelectrode Investigation. *J. Electrochem. Soc.* **1992**, *139*, 2530–2537.

(19) Berg, P.; Promislow, K.; St. Pierre, J.; Stumper, J.; Wetton, B. Water Management in PEM Fuel Cells. *Journal of The Electrochemical Society* **2004**, *151*, A341.

(20) Ji, M.; Wei, Z. A Review of Water Management in Polymer Electrolyte Membrane Fuel Cells. *Energies* **2009**, *2*, 1057–1106.

(21) Adjemian, K. T.; Lee, S. J.; Srinivasan, S.; Benziger, J.; Bocarsly, A. B. Silicon Oxide Nafion Composite Membranes for Proton-Exchange Membrane Fuel Cell Operation at 80-140[degree]C. *J. Electrochem. Soc.* **2002**, *149*, A256–A261.

(22) Adjemian, K. T.; Dominey, R.; Krishnan, L.; Ota, H.; Majsztrik, P.; Zhang, T.; Mann, J.; Kirby, B.; Gatto, L.; Velo-Simpson, M.; et al. Function and Characterization of Metal Oxide−Nafion Composite Membranes for Elevated-Temperature H2/O2 PEM Fuel Cells. *Chemistry of Materials* **2006**, *18*, 2238–2248.

(23) Kim, Y. S.; Wang, F.; Hickner, M.; Zawodzinski, T. A.; McGrath, J. E. Fabrication and Characterization of Heteropolyacid (H3PW12O40)/directly Polymerized Sulfonated Poly(arylene Ether Sulfone) Copolymer Composite Membranes for Higher Temperature Fuel Cell Applications. *Journal of Membrane Science* **2003**, *212*, 263–282.

(24) Patankar, K.; Dillard, D.; Case, S.; Ellis, M.; Lai, Y.-H.; Budinski, M.; Gittleman, C. Hygrothermal Characterization of the Viscoelastic Properties of Gore-Select® 57 Proton Exchange Membrane. *Mechanics of Time-Dependent Materials* **2008**, *12*, 221–236.

(25) Guo, Q. H.; Pintauro, P. N.; Tang, H.; O'Connor, S. Sulfonated and Crosslinked Polyphosphazene-Based Proton-Exchange Membranes. *J. Membr. Sci.* **1999**, *154*, 175–181.

(26) Ye, Y.-S.; Yen, Y.-C.; Cheng, C.-C.; Chen, W. Y.; Tsai, L.-T.; Chang, F.-C. Sulfonated Poly(ether Ether Ketone) Membranes Crosslinked with Sulfonic Acid Containing Benzoxazine Monomer as Proton Exchange Membranes. *Polymer* **2009**, *50*, 3196–3203.

(27) Mauritz, K.; Moore, R. State of Understanding of Nafion. *CHEMICAL REVIEWS* **2004**, *104*, 4535–4585.

(28) Binnig, G. Atomic-Force Microscopy. *Phys. Scr.* **1987**, *T19A*, 53–54.

(29) Albrecht, T.; Quate, C. Atomic Resolution Imaging of a Nonconductor by Atomic Force Microscopy. *J. Appl. Phys.* **1987**, *62*, 2599–2602.

(30) Marti, O.; Drake, B.; Hansma, P. Atomic Force Microscopy of Liquid-Covered Surfaces - Atomic Resolution Images. *Appl. Phys. Lett.* **1987**, *51*, 484–486.

(31) Zhong, Q.; Inniss, D.; Kjoller, K.; Elings, V. Fractured Polymer Silica Fiber Surface Studied by Tapping Mode Atomic-Force Microscopy. *Surf. Sci.* **1993**, *290*, L688–L692.

(32) Cleveland, J.; Anczykowski, B.; Schmid, A.; Elings, V. Energy Dissipation in Tapping-Mode Atomic Force Microscopy. *APPLIED PHYSICS LETTERS* **1998**, *72*, 2613–2615.

(33) Oliver, R. A. Advances in AFM for the Electrical Characterization of Semiconductors. *Rep. Prog. Phys.* **2008**, *71*, 076501.

(34) Bachtold, A.; Fuhrer, M. S.; Plyasunov, S.; Forero, M.; Anderson, E. H.; Zettl, A.; McEuen, P. L. Scanned Probe Microscopy of Electronic Transport in Carbon Nanotubes. *Phys. Rev. Lett.* **2000**, *84*, 6082–6085.

(35) Wang, Z. L.; Song, J. Piezoelectric Nanogenerators Based on Zinc Oxide Nanowire Arrays. *Science* **2006**, *312*, 242–246.

(36) Coffey, D. C.; Reid, O. G.; Rodovsky, D. B.; Bartholomew, G. P.; Ginger, D. S. Mapping Local Photocurrents in Polymer/Fullerene Solar Cells with Photoconductive Atomic Force Microscopy. *Nano Letters* **2007**, *7*, 738–744.

(37) Cohen, H.; Nogues, C.; Ullien, D.; Daube, S.; Naaman, R.; Porath, D. Electrical Characterization of Self-Assembled Single- and Double-Stranded DNA Monolayers Using Conductive AFM. *Faraday Discuss.* **2006**, *131*, 367–376.

(38) Bussian, D. A.; O'Dea, J. R.; Metiu, H.; Buratto, S. K. Nanoscale Current Imaging of the Conducting Channels in Proton Exchange Membrane Fuel Cells. *Nano Letters* **2007**, *7*, 227–232.

(39) Aleksandrova, E.; Hiesgen, R.; Andreas Friedrich, K.; Roduner, E. Electrochemical Atomic Force Microscopy Study of Proton Conductivity in a Nafion Membrane. *Phys. Chem. Chem. Phys.* **2007**, *9*, 2735.

(40) Takimoto, N.; Wu, L.; Ohira, A.; Takeoka, Y.; Rikukawa, M. Hydration Behavior of Perfluorinated and Hydrocarbon-Type Proton Exchange Membranes: Relationship between Morphology and Proton Conduction. *Polymer* **2009**, *50*, 534–540.

(41) He, Q.; Kusoglu, A.; Lucas, I. T.; Clark, K.; Weber, A. Z.; Kostecki, R. Correlating Humidity-Dependent Ionically Conductive Surface Area with Transport Phenomena in Proton-Exchange Membranes. *J. Phys. Chem. B* **2011**, *115*, 11650–11657.

Chapter 2: Imaging Nafion Under Varying Relative Humidity and in Aqueous Solution

2.1 Introduction

As mentioned in the previous chapter, the polymer electrolyte membrane in a PEM fuel cell remains perhaps the most performance limiting component of the entire fuel cell stack. This membrane must be mechanically robust, chemically inert, and have high cationic (proton) conductivity and low anionic (electron) conductivity. Nafion has long been the polymer of choice as it excels in all of these areas, however, its relatively high cost has prompted interest in alternative membrane systems. Additionally, a major drawback of Nafion specifically as well as many polymer electrolytes in general is the dependence of proton conductivity on water content of the membrane.[1] Because of this, much research has focused on the development of new polymers and polymer-composite systems which can operate stably at a wide range of relative humidity, with a specific focus on water retention at low relative humidity.

In addition to designing membranes which can operate at high temperature, there are reasons to understand how a broader range of operating conditions can affect

membrane performance. The water content of PEMs can vary considerably during cell operation; the cathode can become flooded due to water production and electro-osmotic drag while the anode can become relatively dehydrated.[2] This is of particular concern at high current densities or in extreme operating conditions, where the resulting changes in hydration can lead to mechanical deformation which can decrease fuel cell performance substantially and even lead to cell failure. Considerable engineering effort has focused around water management and the mitigation of this problem, however this typically involves adding extra weight and complexity to the fuel cell stack.[3] For this reason, in addition to being able to operate under dehydrated conditions, membranes which can stably and reversibly undergo changes in water content are highly desirable.

The first steps towards designing new membrane materials are to understand how the morphology of current membranes react to changes in water content and temperature. Then, by comparing different membranes we can begin to develop a structure-property relationship and understand how elements of the chemical structure of the polymer lead to favorable morphology and ultimately allow for operation under higher temperature and reduced relative humidity.

In order to develop an understanding of PEM's in general, we began our studies with a well characterized model system: Nafion®. Nafion is a perfluorosulfonic acid (PFSA) proton exchange membrane and is trademarked by DuPont. It has been extensively studied using a wide range of techniques[1,4–18] and remains the most

commonly employed PEM to date. The fluorocarbon backbone is especially chemically stable and mechanically robust, while the fluorine atoms in the sidechains provide an electron withdrawing moiety which renders the sulfonic acid group extremely acidic (pKa = -6). This leads to membranes with high proton conductivity and good chemical and mechanical stability under fuel cell operating conditions. PFSA polymers such as Nafion phase separate upon casting such that the fluorocarbon backbone forms a hydrophobic polymer matrix and the sulfonic acid side chains form a proton conducting network. For a comprehensive review of the relevant work on Nafion, the reader is directed to the following review article.[19]

Despite these favorable attributes, Nafion, and indeed all PEM's, suffer from decreasing proton conductivity at low RH due to dehydration of sulfonic acid groups. It has been shown that the proton conductivity of Nafion and other PEM's is closely tied to the arrangement of proton conducting pathways inside of the membrane, so a major goal of this work is to characterize the phase separated nanostructure of these materials.

Much of the structural data on Nafion has been obtained via small angle X-ray and neutron scattering (SAXS and SANS) studies.[4,7,12,20–22] While SAXS and SANS experiments have been instrumental in characterizing the structure of PFSA materials, they give an incomplete picture of membrane structure due to bulk averaging of data. In order to analyze scattering data it is also necessary to make simplified assumptions about the shape, size distribution and spatial orientation of

scattering objects. Additionally, for highly disordered polymeric materials, there are few, distinct scattering peaks. In the case of Nafion, a single peak representing ionic clusters in the membrane is the only distinct peak in the scattering curve along with a broader peak representing fluorocarbon crystallites. Using the data in these studies, a number of structural models of Nafion have been proposed which fit the scattering data and explain properties such as water sorption, diffusion coefficients, and proton conductivity.[4,7,8,12,23] These structural models generally focus on the nanometer length scale where SAXS data are most easily interpreted and do not fully explain large scale morphology, particularly at lengths above 100 nm.

For this reason, Atomic Force Microscopy is an attractive option for gaining additional structural information on these polymer membranes. The averaging effects and uncertainty present in scattering measurements are avoided, and the surface can be imaged directly. While AFM techniques are limited to the surface of the membrane, many properties of importance to fuel cell operation, such as proton conduction, are tied to the morphology at the surface. Tapping Mode or AC-mode AFM has been shown to be especially effective for polymeric samples, because of the small lateral forces imparted on the sample result in minimal sample damage. Another advantage of AFM is that we are able to investigate a variety of length scales, with resolution in the single nanometer range, and a maximum scan size of 100μm on our instrument.

Previous AFM characterization of Nafion has shown that the hydrophilic and hydrophobic segments of the polymer can be visualized due to differences in tip-sample power dissipation.[24] We use this technique here to map the hydrophilic and hydrophobic domains over a wide range of water contents in order to determine how membrane structure changes in response to hydration and dehydration.

2.2 Experimental Methods for Membrane Characterization

For our initial work on Nafion, as well as subsequent work involving new types of proton exchange membrane we used a similar series of AFM experiments in order to learn about the morphology and electrochemical properties of each membrane. These procedures are outlined here, but are generally employed for all of the membrane characterization discussed in this work.

All topography and phase images were acquired simultaneously with an atomic force microscope (Asylum Research MFP-3D-SA). Nafion 212 was purchased from Clean Fuel Cell Energy LLC and Hyflon Ion® E87-05 was obtained from Solvay Solexis, and 3M membranes were obtained from 3M. Membranes were pretreated by boiling in 5 wt% H_2O_2 for 1 hour, 0.5 M H_2SO_4 for 1 hour, followed by boiling in DI water for 1 hour. All membrane samples were mounted on double sided tape on a glass slide for phase imaging. Membranes imaged under dry conditions were then heated in a vacuum oven for 3 days at 90°C. Membranes under humidified conditions and under water were equilibrated in liquid water at room temperature for 5 days prior to imaging.

Images in air were taken using a silicon probe (NSC15 or XSC11, MikroMasch) with a nominal resonance frequency of 300 kHz and spring constant of 40 N/m. A closed fluid cell (modified PolyHeater, Asylum research) was used to achieve varying relative humidity; either dry or humidified nitrogen was supplied resulting in a 3% and 95% RH atmosphere in the cell, respectively. Membranes were allowed to equilibrate in the cell for 1 hour prior to imaging.

Images in water and methanol were taken in tapping mode using a triangular silicon nitride probe (Olympus TR400PSA, short lever) with a nominal spring constant of 0.08 N/m and a resonant frequency of 34 kHz. Samples were mounted on a Teflon-coated glass slide with a bare circular patch for the sample. Several drops of DI water or methanol were placed on top of the sample in order to form a bead of solution which covered the entire sample. Free amplitudes of approximately 50 nm for the NSC15 cantilever and 200 nm for the TR400PSA were used to image samples in air and liquid, respectively. An amplitude setpoint ratio R/R_o = 70-80% was chosen to optimize tracking of the surface and phase contrast. All scans were conducted at 1 Hz, at 512 x 512 pixels. A first-order flatten was applied to all height images in order to remove any drift in the Z-piezo during scanning. No image modification was used in phase or current images.

Macroscopic swelling was measured by immersing 8 mm circular sections of membranes in the appropriate solvent for 2 weeks and then measuring the diameter of sections with digital calipers.

Conductive images were taken in a closed fluid cell (modified PolyHeater, Asylum research) using a platinum coated tip (Budget Sensors, ElectriMulti or MikroMasch DPER XSC11) with spring constants of 3 N/m and 0.2 N/m. Images were acquired in contact mode with typical contact forces of ~20 nN. Membranes were hot pressed at 130° C onto a small patch of commercial carbon cloth electrode (ELAT-A6) with Nafion solution (Fuel Cell Store) added to the catalyst layer prior to pre-treatment. Humidified hydrogen was supplied via a gas flow channel under the electrode and humidified air was supplied over the membrane surface while scanning. A bias of +1 V was applied to the sample and the heating stage was used to adjust the sample temperature. At the gas flow rates used, we determined with a relative humidity sensor that this resulted in ~80% relative humidity inside of the cell.

Hydrophilic surface area and hydrophilic domain analysis were determined using Igor Pro software by applying a threshold to the sample using the iterative method.[25] For low RH images the threshold often required adjustment from the iterative value to give better visual agreement with phase contrast. Roughness values were calculated from 5 μm x 5 μm height images using the built in analysis in Igor Pro. Correlation length analysis was conducted using the SPIP™ image processing program. Correlation lengths were determined by applying an autocorrelation to 5 μm x 5 μm height images and determining the horizontal distance that has the fastest decay to one standard deviation. For images with anisotropic correlation lengths, the

smallest value was used and the reported correlation lengths represent the average of at least 10 images.

2.3 Imaging Nafion Under Varying Relative Humidity

Using our AFM apparatus, and a closed fluid cell, we were able to access a wide range of relative humidity simply by flowing either dry or humidified nitrogen gas at different rates. While there exist many variants of Nafion with different thicknesses and ion exchange capacities, we chose Nafion 212 for our studies as it is one of the most common membranes for PEM fuel cells. This membrane is 50 microns thick, has a 1050 gram equivalent weight (gram polymer per mol SO_3^- groups) and is solution cast in sulfonate from, in contrast to some membranes which are melt extruded in sulfonyl fluoride form and then ion exchanged to acid form. Since thermal history has been shown to affect properties in these membranes, this is an important consideration.

It has been shown in previous work by O'Dea et al. that the frequency and size of hydrophilic domains is highly dependent on the imaging mode being used. Hydrophilic domains were found to appear more frequently and cover more area when imaging in repulsive mode (phase shifts < 90) as compared to attractive mode (phase shifts >90).[26] This makes sense intuitively, since repulsive mode has been shown to probe mechanical properties further below the sample surface (~5nm depth) whereas attractive mode imaging is confined to the first <1nm below the surface. This results in a greater likelihood that hydrophilic character exists under

the tip at a given point when imaging in repulsive mode and thus a higher apparent hydrophilic surface area. For these studies, we are primarily interested in the morphology directly at the surface of the membrane, as this has the greatest effect on proton conduction, as such we image in attractive mode when possible in order to probe the very surface of the membrane locally and avoid contributions from further below the surface.

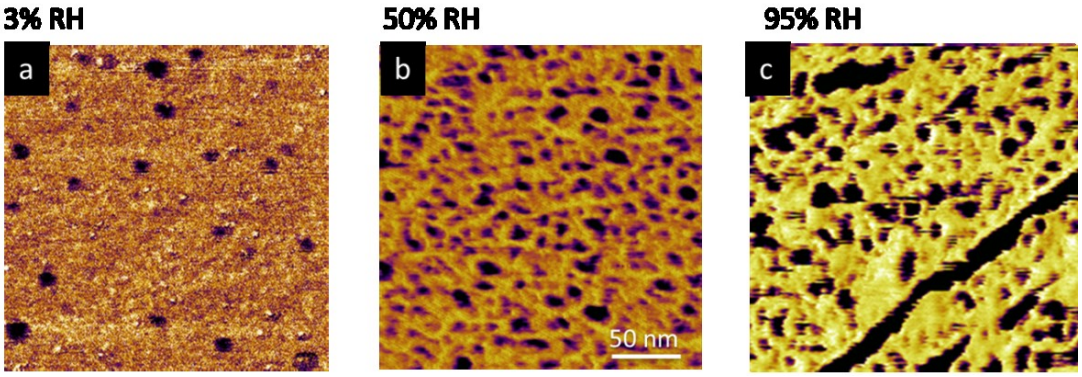

Figure 2.1: Representative AFM Phase images of Nafion 212 under dehydrated, ambient, and hydrated conditions. This was after an initial thermal pre-treatment step. Imaging was conducted with an NSC15 cantilever with a scan size of 250 nm.

For Nafion we found that at the range of relative humidity found in our lab (30-60%) roughly 20% of the surface of Nafion is covered by hydrophilic domains. This number is an approximate average from several attractive mode phase images, the image shown in figure 2.1b is representative of these and shows 19.4% hydrophilic surface area. To probe morphology at different water contents we employed a closed fluid cell, which by flowing either dry or humidified nitrogen gas at varying flow rates, we were able to create environments from 3 – 98% relative humidity inside the

chamber. At dehydrated conditions, and in the attractive imaging regime, we observe no phase contrast indicating that the surface of the membrane has been left completely dehydrated. Under repulsive mode, however, we see isolated domains of positive phase contrast, which in this case indicates increased power dissipation, or a softer area under the tip. We interpret this as hydrophilic domains present in the first few nanometers below the membrane surface. Interestingly, these domains appear much less frequently than at ambient conditions, implying an inhomogeneous dehydration of domains, or a rearrangement of the surface to accommodate the decrease in water content.

Lastly, at high RH conditions, which ranged from (95-99%) we observe the formation of large wormlike structures which cover much of the surface. These worm or fiber-like features also show negative phase contrast, indicating that they are highly dissipating and thus water rich. Due to their shape, physical properties, and the fact that they coincide with a higher membrane water content, we assign these as cylindrical inverted micelles which form parallel to the surface. This is in contrast to the through-plane inverted micelle or parallel pore structure which is predicted for lower water contents. These features are much larger than individual hydrophilic domains, and in most cases even larger than fluorocarbon crystallites expected size based on SAXS measurements. While these features cover much of the surface, the areas between them retain the original parallel pore morphology which is present under ambient conditions. It appears then that there are two forms of swelling

occurring, a dilation of individual hydrophilic domains accompanied by a coalescence or rearrangement of domains to form these larger, cylindrical structures.

We next employed conductive probe AFM under similar, high RH conditions in order to observe the potential effect that these features have on proton conductivity and fuel cell performance. These experiments were conducted at 80% RH, although similar experiments were also performed up to 95% RH. Resolution can become problematic in the extremely high RH regime due to condensation at the AFM tip which decreases lateral resolution and increases current readings. Figure 2.2 shows topographic and conductivity images and shows an example of a cylindrical fiber feature under fuel cell operating conditions.

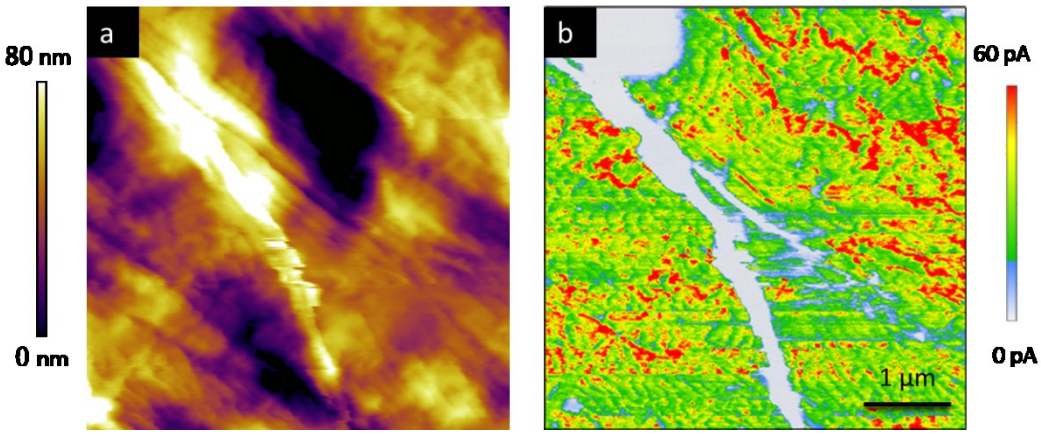

Figure 2.2: Topographic (a) and Conductive (b) images of Nafion 212 hot pressed onto a commercial electrode and imaged at 50C and 80% RH. Flow rates are 0.05 L/min humidified hydrogen and 0.3 L/min humidified air, +1V sample bias.

We see the raised cylindrical shape of the feature, as well as a completely insulating character in the conductivity image. This indicates that although these

features are water rich, they do not conduct protons in the through-plane direction. It is likely that the fluorocarbon layer prohibits an effective connection between the AFM tip and the internal hydrophilic phase, or between the fiber feature and the rest of the hydrophilic phase inside of the membrane. Due to the high relative humidity employed and the fact that cp-AFM requires operation in contact mode, resolution was limited and only larger fiber features could be well resolved in conductivity images.

Previous work has shown that in membrane electrode assemblies containing Nafion, the elevated temperature and humidity during pretreatment induces the formation of Nafion fibers.[6] These fibers were theorized to increase performance of the fuel cell by providing proton conducting paths into the catalyst layer. The insulating nature of these features in our images suggests that while they may allow for proton transport along their length, parallel to the surface, the external fluorocarbon layer does not provide a conductive path through the membrane. This implies that factors other than proton conduction in the polymer phase may be responsible for the improved performance. Our images are of a flat membrane surface, whereas in an actual fuel cell the membrane electrode interface extends in three-dimensions and is considerably more complex. This is an important limitation of our technique and future work in our group is focused on refining our conductive imaging technique to answer questions regarding proton transport inside the catalyst layer.

2.4 Imaging Nafion in Liquid Environment

As a continuation of our work at high RH atmosphere, it was desirable to investigate the effect of equilibration with liquid water on the structure of the membrane. During fuel cell operation, it is possible for significant water to accumulate at the electrodes of the cell, especially the cathode. At the pressures being employed, this causes conditions where the activity of the water is essentially 1. Additionally, previous work has shown that Nafion undergoes significantly different water uptake behavior when exposed to liquid water versus saturated or heavily humidified water vapor. For this reason we decided to investigate Nafion under liquid water to determine if these conditions led to any further changes in morphology. While liquid imaging is routine for many samples, the only prior example of its application to Nafion has been in the work of Bass et al.[16]

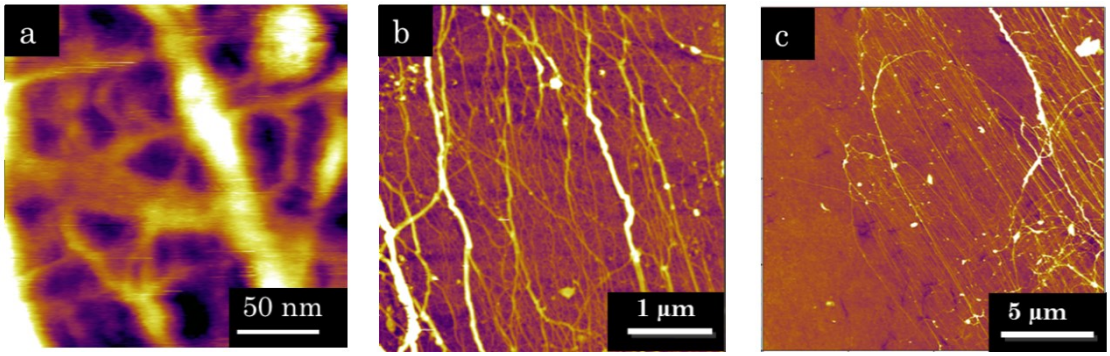

Figure 2.3: Representative topographic images of Nafion 212 in deionized water, scan sizes are 250 nm (a) 5 µm (b) and 20 µm (c).

When Nafion 212 is imaged under DI water, the number of worm-like features is increased compared to membranes equilibrated at 95% RH[27] . Under water, features as small as 20 nm in diameter can be resolved and connectivity between worm-like

features appears to increase. This is most likely caused by the increased volume fraction of water in our liquid-equilibrated samples compared to our vapor equilibrated samples. Other groups have reported a significant increase in water content when relative humidity is increased from 95% to 100%.[1,14] We attribute the higher density of worm-like features in the liquid-equilibrated sample to this higher water content. Under water, higher resolution of these features is attainable due to the lack of condensation affecting the AFM tip as was observed in humid atmosphere.

Figure 2.3 shows topographic AFM images of Nafion 212 collected under DI water for three separate scan sizes. At small scales, we can see the cylindrical shape, as well as high degree of branching in these features creating a randomly oriented, interconnected network of features. At larger scales, a local directionality often emerges with long fibers adopting a parallel configuration. Analysis of a large number of images ($n > 50$) shows a large variation in the surface coverage of fiber features; anywhere from 1-15% of the membrane surface in a given 20 μm x 20 μm area. This could be related to the randomness of the Nafion polymer and slightly different densities of sidechains on the 100 nanometer to micron length scale. Worm-like features were found in excess of 10 μm in length and often show a local alignment, however images at different locations on the same sample show different directions of alignment indicating that there is no preferred orientation. On even larger length scales, clustering of features was observed, with large portions of worm-like morphology existing between featureless regions of the membrane.

Figure 3c shows a large scale (20 μm x 20 μm) topographic image of Nafion 212 with this clustering of worm-like features.

These features were only observed in pre-treated membranes, implying that they may represent a structural rearrangement induced by the elevated temperatures and high degree of swelling during thermal pre-treatment (boiling). This agrees with work by Kim et al. and Alberti et al. where the water uptake of Nafion increased considerably with increasing hydrothermal treatment temperatures.[289] It was observed that, to some extent, these features persisted several months after pre-treatment in membranes exposed to ambient conditions, implying that once this rearrangement occurs the new morphology is relatively stable. This is consistent with the work done by Onishi et al.[29] describing the extremely slow equilibration times that Nafion membranes exhibit with regards to water sorption and desorption. These features were only observed in pre-treated membranes, implying that structural rearrangement may be induced by the elevated temperatures and high degree of swelling during pre-treatment (boiling). Figure 2.4 shows a topographic image of a Nafion membrane that has been thermally pretreated, liquid equilibrated, and then finally dehydrated and imaged under dry conditions. We see that the larger worm-like features persist, but the occurrence of smaller features decreases drastically. It may be that a limited amount of rearrangement back towards a neat surface does occur, but that larger features are either thermodynamically stable or kinetically trapped due to a prohibitively high energy barrier for the reverse rearrangement to occur.

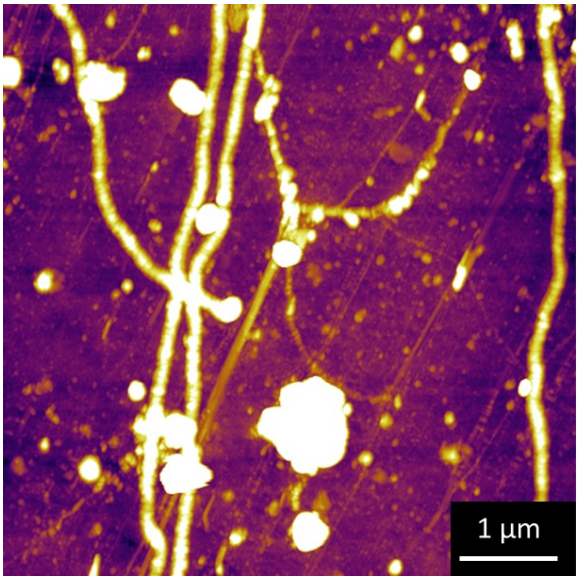

Figure 2.4: Topographic image of Nafion 212 after thermal pretreatment, liquid equilibration, and subsequent dehydration. Imaged under 5% RH dry nitrogen atmosphere.

One challenge to imaging in liquids is that the relatively simple relationship between tip-sample power dissipation and phase contrast does not hold true in water. While dissipative forces are still present, the highly damping liquid environment greatly reduces the phase contrast associated with these forces. It has been found that in liquids, conservative or elastic forces play a much larger role in determining the relative phase values.[30] For this reason, we found very little contrast between hydrophilic domains and the surrounding hydrophobic surface when imaging in water. Figure 5 shows an example of a topographic and phase image collected under water in an area where no fiber features were present. While phase contrast is visible, its extremely small magnitude (< 0.5°) and high degree of coupling to topography make it difficult to accurately assign hydrophilic and hydrophobic area. Different

cantilevers and imaging conditions were experimented with, but it was not possible to sufficiently increase phase contrast. The resolution of phase images was also lower than is desired for assigning hydrophilic surface area, and thus did not allow for an accurate statistical analysis of hydrophilic domains. What we can gather from our phase images, however, is that the parallel pore morphology is largely retained in these sections of membrane.

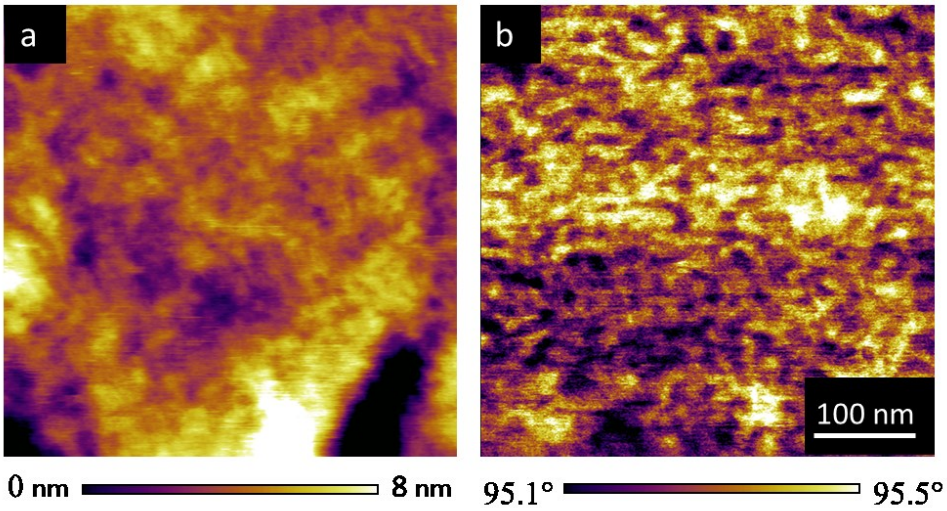

Figure 2.5: Topography (a) and Phase (b) of Nafion 212 imaged under deionized water. Image was selected at a location with a flat membrane surface.

We had greater success achieving reliable phase contrast on areas of the membrane which exhibited worm-like features. This required the optimization of imaging conditions and the use of the proper cantilever resonance. As mentioned in the experimental section, the fundamental peak for the TR400PSA cantilevers used for imaging is nominally 34 kHz in air which is decreased to around 10 kHz in the highly dissipative fluid environment. Imaging was usually conducted at one of a few

higher resonances which occur in the 20-40 kHz range. These specific resonances vary between levers and are likely also affected by the specific orientation of the AFM chip inside of the tip holder. In certain levers, we noticed an especially low frequency (~21KHz) and high quality factor (q = 40) resonance peak which gave much better phase contrast. We found that this resonance allowed for imaging in the repulsive regime, which was nearly impossible for lower quality factor resonances. Figure 6 shows two series of images, the left column using a low q factor resonance, and the right using the higher q factor. Both topographic images show good resolution, but the low-q phase image exhibits contrast which is essentially identical to the derivative of the topographic image shown below. This behavior has been demonstrated previously by O'Dea et al. and indicates that topography, not mechanical properties are causing this contrast; this is not surprising given the large surface roughness.[26] Using the high-q resonance and operating in repulsive mode, we are able to see a marked negative phase contrast which is independent of topography. As mentioned previously, the dissipative model for phase contrast does not hold in fluids with a soft cantilever. Melcher and coworkers have shown experimentally that in liquids, conservative or elastic forces play a much larger role in determining phase contrast.[30] If we apply their interpretation to our images, this negative contrast coincides with a lower elasticity at these locations. This is likely a consequence of the confined water inside of these features yielding a less elastic response than the surrounding polymer surface. We also see a region along the outside of fiber features which exhibit positive phase contrast which may indicate

that we are observing the increased stiffness and elasticity of the fluorocarbon layer on the outside of these inverted micelles.

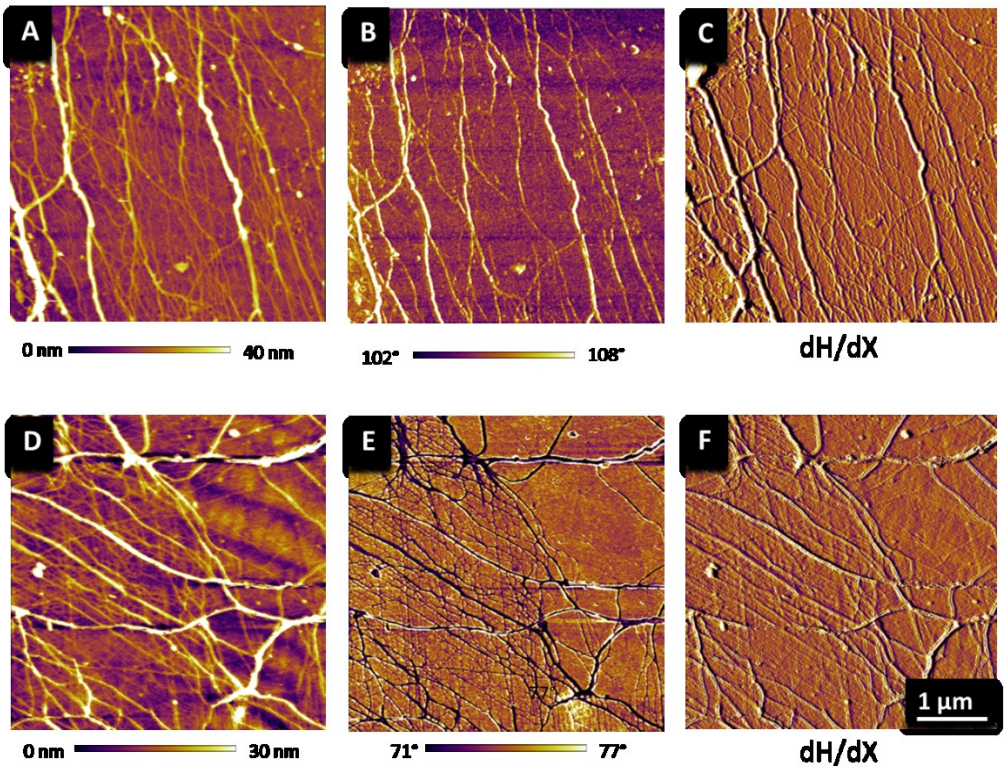

Figure 2.6: Topography (a,d), phase (b, e), and first derivative of topography(c,f) using a low quality factor resonance (a-c) and high quality factor resonance (d-f).

2.5 Comparing AFM to SAXS Data

We have convincing evidence supporting these features being cylindrical inverted micelles, we now need to examine how these features relate to data collected from SAXS and structural models created from this data. Schmidt-Rohr and Chen proposed a structural model of Nafion consisting of locally parallel water channels which fits experimental scattering data very well at large q-values (>0.01 Å^{-}

[1]) and low water contents.[8] At high water contents and in solution, it has been shown that rod-like aggregates are the primary morphology of Nafion.[7] In our work, we can visualize directly the transition from the normal parallel water channel morphology to the rod like morphology; the raised, worm-like features at high degrees of swelling. We have also noticed that once the membrane forms this rod-like morphology, it is stable and the return to the parallel water channel morphology happens slowly if at all, implying that this is not a reversible transition. This in itself is an important consideration for fuel cell operation, where cycling between wet and dry environments is a common occurrence.

Bass et al. reported that the surface of Nafion increases in roughness when moving from saturated water vapor to a liquid water environment due to a rearrangement of ionic clusters near the surface.[16] The only factor which changes in our observations is the increased presence of worm-like features, which increases the root mean square (rms) roughness of the surface from 6.5 nm to 8 nm. Our interpretation based on our images is that the increased surface roughness is caused by the formation of more worm-like features (large inverted micelles) parallel to the surface as opposed to (non-inverted) micelles normal to the surface. Our rms roughness values were in general, much higher than those reported by Bass (~7 nm vs. ~1 nm) most likely owing to the spin casting and high temperature annealing used in their study. Because of the different casting and thermal history, it is not surprising that different morphological features are observed in each case.

The formation of worm-like features at high relative humidity and the increased presence of these features in Nafion membranes imaged under liquid water is consistent with previous small angle X-ray scattering (SAXS) data which revealed hydration dependent scattering at this length scale. SAXS is a bulk technique and thus provides information about morphology and crystallinity from the entire volume of the membrane whereas AFM characterizes only the first few nanometers near the surface. Since morphology at the surface of the membrane and in the bulk can both affect the performance of the resulting fuel cell, it is important to examine both sets of data independently and compare the information from each. Rubatat and coworkers used SAXS to characterize the structural evolution of Nafion from dehydrated to swollen states.[7] The USAXS upturn was absent at low membrane water contents and increased in intensity with increasing membrane water content, implying that a large length scale (>50 nm) inhomogeneity in electron density appears and becomes more pronounced with an increasing volume fraction of water. We believe that it is a non-uniform distribution of water at large length scales caused by these large worm-like features which results in the enhanced scattering in the USAXS upturn. To compare our AFM data to previous scattering data we conducted a correlation length analysis. Correlation length represents the average distance between scattering objects – in this case the worm-like features. This number is inversely related to the scattering vector, which allows us to determine which region in reciprocal space these features should cause scattering. After analyzing twenty separate 5 μm x 5 μm images, the average correlation length of worm-like features

was found to be 77.4 nm with a standard deviation of 54.4 nm. Due to local alignment, correlation lengths were often anisotropic for a given image. Figure X shows a topographic image, alongside the resulting autocorrelation image. The arrows in the autocorrelation image highlight the directional dependence of the correlation length in this image.

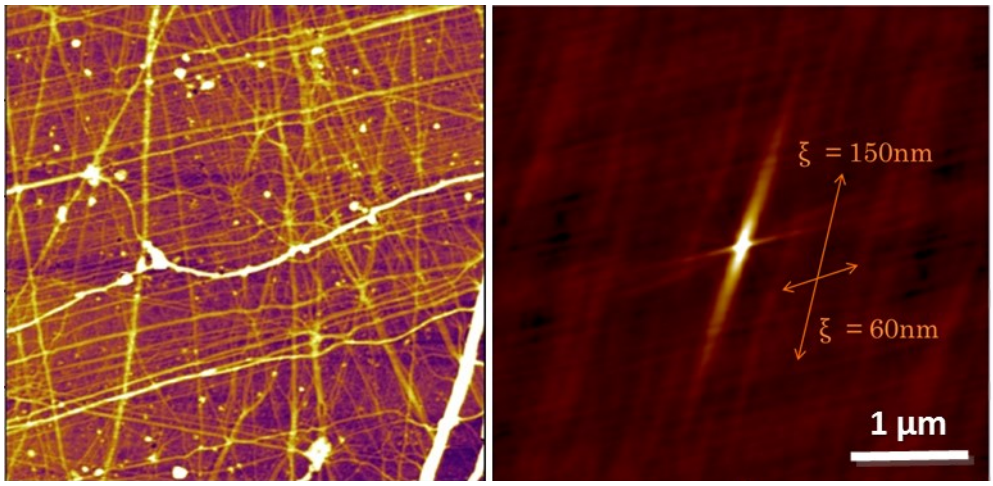

Figure 2.7: Topographic (a) and autocorrelation image (b) of Nafion 212 in deionized water. Arrows indicate correlation length in each direction. The reported correlation length values were averaged from the minimum length found in 20 such images.

Because SAXS experiments generally involve radial averaging of data, we can assume that because of the different directionality of different parts of the membrane surface that this directional dependence is averaged out. As such, the shortest correlation length was used as it best represents the true spacing of features and the radial average.

Since the spacing between features and the scattering vector are related by a factor of 2π, our correlation length yields a theoretical scattering vector of

0.00785 $Å^{-1}$, corresponding roughly to the position of the USAXS upturn with the greatest increase in scattering. This correlation length, along with the broad distribution of correlation lengths agree well with the position and shape of the USAXS upturn. Using a simple Debye-Beuche model, Rubatat et al. determined that a 60-100 nm correlation length provided a good fit to the experimental scattering data,[7] which is also consistent with our AFM data.

Despite this good general agreement, there are some important differences between what we observe by AFM and what Rubatat and coworkers were able to deduce from SAXS. It has been noted previously that SAXS data is necessary to generate an accurate structural model, but is not sufficient on its own as many conflicting models can accurately reconstruct the same SAXS curve. The model constructed by Rubatat et al. consists of spheres of water between large polymeric and relatively hydrophobic ribbons or fibrillar features. According to our AFM data, we see the opposite, water rich cylindrical inverted micelles surrounding regions of parallel pore morphology which have lower water content. To assess the low angle scattering of these features, we employed an equation for modeling the scattering of cylindrical inverted micelles which was first put forth by Bardez et al.[31] This equation uses different parameters and required assumptions about the hydrophilic volume fraction that the micelles take up. In the range of 5-20% we achieved curves which fit the experimental scattering data very well. We used 80nm as the theoretical diameter of fiber features which is shown as the red trace in figure 7a.

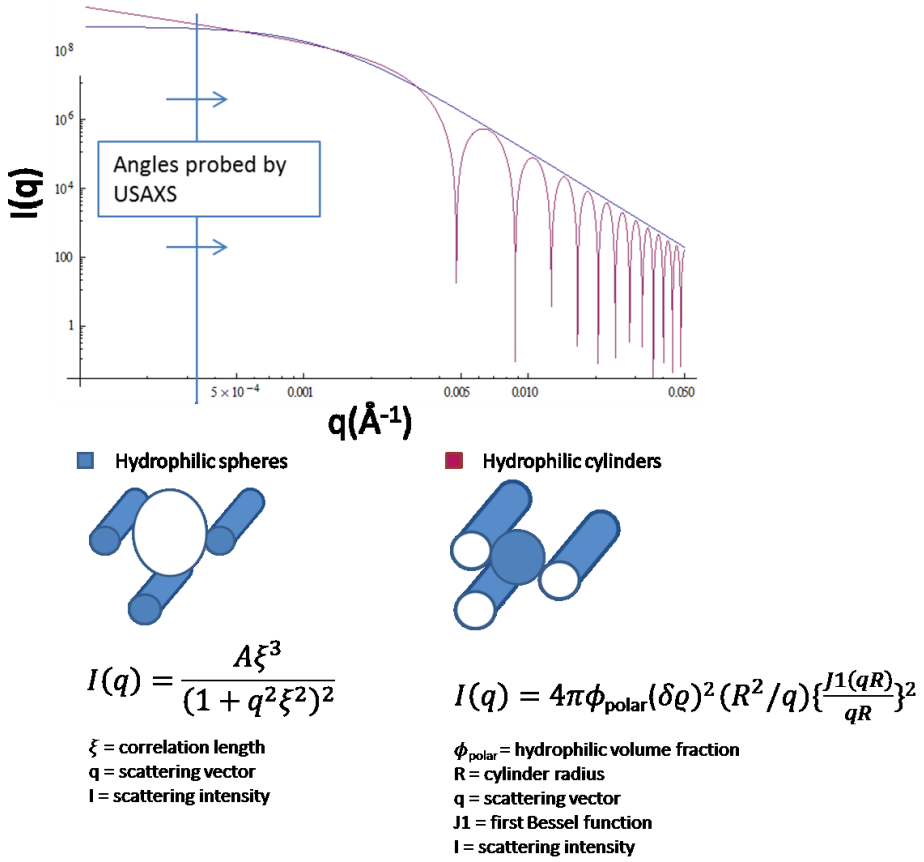

Figure 2.8: Theoretical scattering intensity for a network of hydrophilic spheres versus hydrophilic cylinders. Modelling equations and a schematic of each model are shown below.

As is apparent, both models give an almost identical theoretical scattering curve and agree very well with the SAXS data collected by Rubatat et al. The periodic oscillation at higher scattering vectors in our cylindrical model can be explained by the monodisperse radius used, which results in gaps in scattering intensity. If a broad distribution of values (as is observed in AFM images) was used then a smooth curve would be expected. From this we can see that our cylindrical inverted micelle model not only satisfies our AFM data, but also gives good agreement with SAXS data collected by other groups under similar conditions.

In order to fully compare scattering data with AFM, it is necessary to collect structural information from the interior of the membrane as well as the surface. SAXS is a bulk technique and thus probes the entire volume of the membrane, and while surface morphology does have a contribution, it likely cannot account for the strong USAXS upturn which is observed. We conducted a series of experiments where pretreated membranes were cryofractured using liquid nitrogen and then imaged under deionized water. Figure 8 shows the image previously shown of the neat membrane surface under water alongside a cryofractured cross section imaged under water as well. We noticed that cryofractured samples also exhibit the worm-like morphology that we see at the surface as is shown in the worm-like features extending left to right across the image. We also see circular negative height features which may correspond to worm-like features that have been cut along their short axis. Because of the roughness that is introduced during fracturing, a meaningful correlation length could not be extracted from these images, however, we can see qualitative evidence of similar morphology.

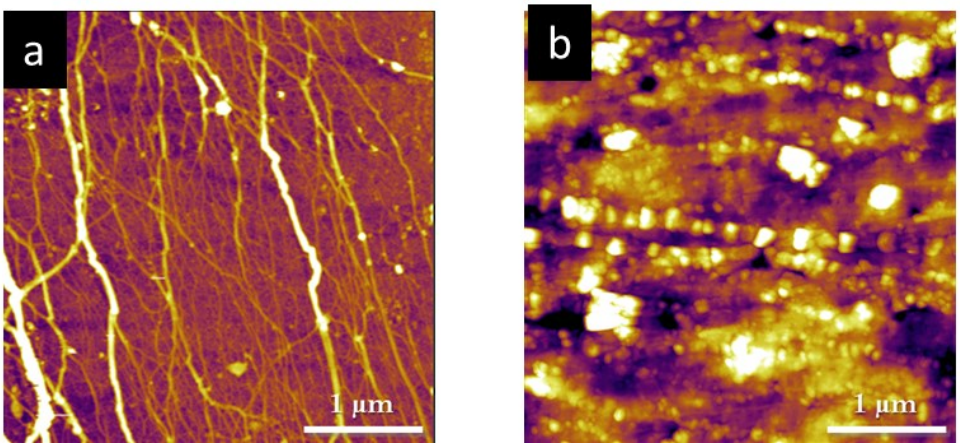

Figure 2.9: Topographic images of the surface (a) and cryofractured cross-section (b) of Nafion 212 imaged in deionized water.

We also experimented with microtoming membrane samples to obtain cross-sections, and while these samples were less rough, they suffered from shearing in the blading direction. Cryomicrotoming is probably an ideal method to obtain clean, unaltered cross sections and future experiments will investigate the utility of this method.

2.6 Imaging Nafion in Alcohol Solutions

To further probe the swelling behavior of Nafion in the context of direct methanol fuel cells (DMFC's), we conducted a series of imaging experiments equilibrating Nafion in different aliphatic alcohol solutions. In DMFC's, a liquid fuel mixture is fed at the anode side which consists of low concentrations (1-2 M) of methanol which are then effectively in equilibrium with the membrane. PFSA membranes have been shown to swell to an even greater degree in aliphatic alcohols

than in water, so this also provides an extension of the swelling characterization conducted so far. We conducted experiments in isopropanol, methanol and ethanol, and observed qualitatively similar behavior in each. At concentrations typical for DMFC operation, there was no discernable difference in morphology, but as concentrations were increased the swelling became detectable by AFM. In the methanol solution, we see an increase in the spacing of worm-like features as the methanol concentration is increased while the worm-like features themselves were not observed to change in diameter. The average correlation length of worm-like features increases from 77.4 nm to 128 nm as the concentration is increased from 0 to 50 vol%. These correlation lengths were also determined by averaging several (n = 10) images. We attempted to conduct imaging under even higher methanol concentrations but were unable to due to excessive swelling of the membrane and its delamination from the substrate. Even at 50% methanol, evaporation of solution becomes a substantial issue and care must be taken to continuously add new solution to keep a stable imaging environment.

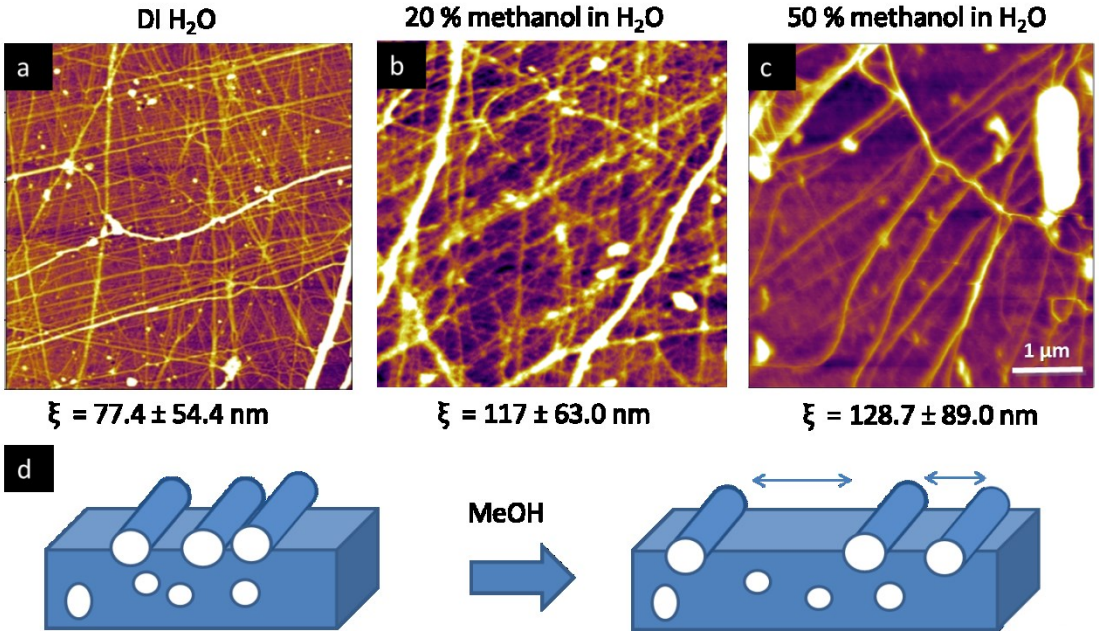

Figure 2.10: Topographic images of Nafion 212 under DI water (a), 20% aqueous methanol solution (b) and 50% aqueous methanol (c). Correlation lengths obtained from the average of 10 images are reported under each image and (d) shows the increase in fibril spacing schematically.

The type of swelling we observe is consistent with the work of Haubould et al. who theorized that methanol should preferentially solvate hydrophobic segments of Nafion, expanding the polymer matrix but leaving the volume of the hydrophilic core unchanged.[32] Chomakovahaefke et al. also proposed a similar type of swelling based on AFM data where fibril features similar to the worm-like features we observe were found to unwind and reorient with increasing water content.[33] We do not observe a significant decrease in surface roughness between methanol solution and the water equilibrated samples as reported by Affoune et al.[34,35] That study, however,

equilibrated Nafion membranes in pure alcohols and imaged them in air which could create a different morphology than was observed here.

In order to compare our AFM data to bulk swelling measurements, we equilibrated sections of membrane in methanol solution and compared the bulk in-plane swelling to our AFM observations. We saw that Nafion increased in area 22% moving from water to a 50% methanol solution. This is a smaller increase than the increase in correlation lengths would suggest, possibly due to the increase in spacing of features, but not their size. This also indicates that the swelling behavior is likely more complex than an isotropic spreading of fiber features and that fiber features may reorient during swelling.

2.7 Conclusions

In summary, we have characterized the surface morphology of Nafion 212 over a wide range of relative humidity, and in aqueous solution. We have shown that at dehydrated conditions, most of Nafion's surface hydrophilicity is lost and surface reorganization occurs to form fewer aqueous domains. At high degrees of swelling we see the formation of large fiber-like features which cover much of the surface. Phase and conductive probe AFM of these features allows us to determine their chemical makeup; i.e. cylindrical inverted micelles. This structural rearrangement at the extremes of relative humidity explains many of the adverse effects that these conditions have on cell performance.

Imaging in water and methanol solutions provides a further degree of swelling, and we observe increased fibril formation under these conditions. By conducting a statistical analysis of images, we are able to directly relate our AFM images to SAXS data collected by other groups. We used this to reconcile areas where structural models based on SAXS data are oversimplified and incomplete, and have constructed a model which better explains all available data. With this understanding of Nafion, we now seek to investigate novel membrane systems which seek to improve on its performance.

References

(1) Zawodzinski, J.; Springer, T. E.; Davey, J.; Jestel, R.; Lopez, C.; Valerio, J.; Gottesfeld, S. A Comparative Study of Water Uptake By and Transport Through Ionomeric Fuel Cell Membranes. *J. Electrochem. Soc.* **1993**, *140*, 1981–1985.

(2) Li, H.; Tang, Y.; Wang, Z.; Shi, Z.; Wu, S.; Song, D.; Zhang, J.; Fatih, K.; Zhang, J.; Wang, H.; et al. A Review of Water Flooding Issues in the Proton Exchange Membrane Fuel Cell. *Journal of Power Sources* **2008**, *178*, 103–117.

(3) Two Fuel Cell Cars in Every Garage? *Electrochem. Soc. Interface (USA)* **2005**, *14*, 24–3535.

(4) Kim, M.; Glinka, C.; Grot, S.; Grot, W. SANS Study of the Effects of Water Vapor Sorption on the Nanoscale Structure of Perfluorinated Sulfonic Acid (NAFION) Membranes. *MACROMOLECULES* **2006**, *39*, 4775–4787.

(5) Kong, X.; Schmidt-Rohr, K. Water-Polymer Interfacial Area in Nafion: Comparison with Structural Models. *Polymer* **2011**, *52*, 1971–1974.

(6) Snyder, J. D.; Elabd, Y. A. Nafion® Nanofibers and Their Effect on Polymer Electrolyte Membrane Fuel Cell Performance. *Journal of Power Sources* **2009**, *186*, 385–392.

(7) Rubatat, L.; Gebel, G.; Diat, O. Fibrillar Structure of Nafion: Matching Fourier and Real Space Studies of Corresponding Films and Solutions. *Macromolecules* **2004**, *37*, 7772–7783.

(8) Schmidt-Rohr, K.; Chen, Q. Parallel Cylindrical Water Nanochannels in Nafion Fuel-Cell Membranes. *Nat Mater* **2007**, *7*, 75–83.

(9) Alberti, G.; Narducci, R.; Sganappa, M. Effects of Hydrothermal/thermal Treatments on the Water-Uptake of Nafion Membranes and Relations with Changes of Conformation, Counter-Elastic Force and Tensile Modulus of the Matrix. *Journal of Power Sources* **2008**, *178*, 575–583.

(10) Laporta, M.; Pegoraro, M.; Zanderighi, L. Perfluorosulfonated Membrane (Nafion): FT-IR Study of the State of Water with Increasing Humidity. *Physical Chemistry Chemical Physics* **1999**, *1*, 4619–4628.

(11) Hiesgen, R.; Helmly, S.; Galm, I.; Morawietz, T.; Handl, M.; Friedrich, K. A. Microscopic Analysis of Current and Mechanical Properties of Nafion® Studied by Atomic Force Microscopy. *Membranes* **2012**, *2*, 783–803.

(12) Gierke, T. D.; Munn, G. E.; Wilson, F. C. The Morphology in Nafion Perfluorinated Membrane Products, as Determined by Wide- and Small-angle X-ray Studies. *Journal of Polymer Science: Polymer Physics Edition* **1981**, *19*, 1687–1704.

(13) Gebel, G.; Aldebert, P.; Pineri, M. Swelling Study of Perfluorosulphonated Ionomer Membranes. *Polymer* **1993**, *34*, 333–339.

(14) Morris, D. R.; Sun, X. Water-sorption and Transport Properties of Nafion 117 H. *Journal of Applied Polymer Science* **2003**, *50*, 1445–1452.

(15) P. J. James, J. A. Elliott, T. J. McMaster, J. M. Newton, A. M. S. Elliott, S. Hanna and M. J. Miles. Hydration of Nafion® Studied by AFM and X-Ray Scattering. *Journal of Materials Science* **2000**, *35*, 5111–5119.

(16) Bass, M.; Berman, A.; Singh, A.; Konovalov, O.; Freger, V. Surface-Induced Micelle Orientation in Nafion Films. *Macromolecules* **2011**, *44*, 2893–2899.

(17) Chaabane, L.; Dammak, L.; Grande, D.; Larchet, C.; Huguet, P.; Nikonenko, S. V.; Nikonenko, V. V. Swelling and Permeability of Nafion®117 in Water-Methanol Solutions: An Experimental and Modelling Investigation. *Journal of Membrane Science* **2011**, *377*, 54–64.

(18) Chen, C.; Fuller, T. F. The Effect of Humidity on the Degradation of Nafion® Membrane. *Polymer Degradation and Stability* **2009**, *94*, 1436–1447.

(19) Mauritz, K.; Moore, R. State of Understanding of Nafion. *CHEMICAL REVIEWS* **2004**, *104*, 4535–4585.

(20) Hsu, W. Y.; Gierke, T. D. Ion Transport and Clustering in Nafion Perfluorinated Membranes. *Journal of Membrane Science* **1983**, *13*, 307–326.

(21) Roche, E. J.; Pineri, M.; Duplessix, R. Phase Separation in Perfluorosulfonate Ionomer Membranes. *J. Polym. Sci. Polym. Phys. Ed.* **1982**, *20*, 107–116.

(22) Starkweather, H. W. Crystallinity in Perfluorosulfonic Acid Ionomers and Related Polymers. *Macromolecules* **1982**, *15*, 320–323.

(23) Elliott, J. A.; Hanna, S.; Elliott, A. M. S.; Cooley, G. E. Interpretation of the Small-Angle X-Ray Scattering from Swollen and Oriented Perfluorinated Ionomer Membranes. *Macromolecules* **2011**, *33*, 4161–4171.

(24) McLean, R. S.; Doyle, M.; Sauer, B. B. High-Resolution Imaging of Ionic Domains and Crystal Morphology in Ionomers Using AFM Techniques. *Macromolecules* **2000**, *33*, 6541–6550.

(25) Picture Thresholding Using an Iterative Selection Method. *IEEE Transactions on Systems, Man, and Cybernetics* **1978**, *8*, 630–632.

(26) O'Dea, J. R.; Buratto, S. K. Phase Imaging of Proton Exchange Membranes under Attractive and Repulsive Tip−Sample Interaction Forces. *The Journal of Physical Chemistry B* **2011**, *115*, 1014–1020.

(27) O'Dea, J. R.; Economou, N. J.; Buratto, S. K. Surface Morphology of Nafion at Hydrated and Dehydrated Conditions. *Macromolecules* **2013**.

(28) Kim, Y. S.; Dong, L.; Hickner, M. A.; Pivovar, B. S.; McGrath, J. E. Processing Induced Morphological Development in Hydrated Sulfonated Poly(arylene Ether Sulfone) Copolymer Membranes. *Polymer* **2003**, *44*, 5729–5736.

(29) Onishi, L. M.; Prausnitz, J. M.; Newman, J. Water−Nafion Equilibria. Absence of Schroeder's Paradox. *J. Phys. Chem. B* **2011**, *111*, 10166–10173.

(30) Melcher, J.; Carrasco, C.; Xu, X.; Carrascosa, J. L.; Gómez-Herrero, J.; José de Pablo, P.; Raman, A. Origins of Phase Contrast in the Atomic Force

Microscope in Liquids. *Proceedings of the National Academy of Sciences* **2009**, *106*, 13655–13660.

(31) Bardez, E.; Vy, N. C.; Zemb, T. Counterion-Driven Sphere to Cylinder Transition in Reverse Micelles: A Small Angle X-Ray Scattering and Conductometric Study. *Langmuir* **1995**, *11*, 3374–3381.

(32) Haubold, H.-G.; Vad, T.; Jungbluth, H.; Hiller, P. Nano Structure of NAFION: A SAXS Study. *Electrochimica Acta* **2001**, *46*, 1559–1563.

(33) Chomakovahaefke, M.; Nyffengger, R.; Schmidt, E. Structure Reorganization in Polymer Films of Nafion Due to Swelling. *Applied Physics A - Materials Science and Processing.* **1994**, *59*, 151–153.

(34) Affoune, A. M.; Yamada, A.; Umeda, M. Surface Observation of Solvent-Impregnated Nafion Membrane with Atomic Force Microscopy. *Langmuir* **2004**, *20*, 6965–6968.

(35) Affoune, A. M.; Yamada, A.; Umeda, M. Conductivity and Surface Morphology of Nafion Membrane in Water and Alcohol Environments. *Journal of Power Sources* **2005**, *148*, 9–17.

Chapter 3: Imaging Short Side Chain Perfluorosulfonic Acid Membranes; Hyflon Ion

3.1 Introduction

After our initial work on Nafion, we wanted to investigate how the morphology and proton conductivity of Nafion compares to other PFSA membranes that are commercially available or under development. These membranes have similar chemical composition, and understanding how small changes in the chemical structure of the polymer can affect the morphology of the resulting membrane and ultimately fuel cell performance is one of the primary goals of this research.

The first structural feature investigated was the length of the sulfonic acid sidechains in the PFSA polymer. Nafion represents a long side chain (LSC) PFSA polymer with a four carbon ether side-chain and is the most commonly used membrane for fuel cell applications. Short side chain (SSC) PFSA membranes with two carbon ether side-chains such as Hyflon Ion® have gained interest as a Nafion replacement because they have been shown to outperform Nafion in fuel cells.[1,2,3]

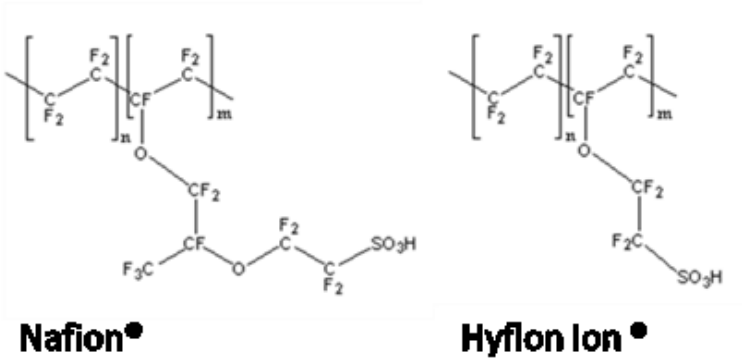

Figure 3.1: Chemical structures of Nafion and Hyflon Ion polymers.

Structures of both Nafion and Hyflon are shown in Figure 3.1. The chemical structures differ only in the length of side chains, however this small difference has been shown to cause a significant effect on the thermal, mechanical and ion transport properties of the membrane.[2,4]

Interest in shorter side chain PFSA variants initially began in the 1980's when DOW chemical company began developing alternative membranes based on this structure. However despite reports of the improved performance they exhibited,[4,5] these materials were not pursued commercially, possibly due to a complicated and costly synthetic route. In the early 2000's, Solexis started using a simplified synthesis and began to distribute these materials under the trade name Hyflon Ion.[3,6,7] Small angle X-ray scattering analysis has been previously employed to characterize these membranes[2,8,9], but as with Nafion, the spatial averaging inherent to this technique

limit the usable structural information which can be extracted. Here we compare Nafion 212, which is the current state of the art LSC membrane to Hyflon Ion E87-05, a similar SSC membrane. These membranes differ only in terms of their chemical structure, as outlined in figure 3.1 and their equivalent weight or ion exchange capacity. Hyflon has an equivalent weight of ~860 g/mol whereas Nafion has an equivalent weight of 1050 g/mol. The decreased equivalent weight of the Hyflon membrane imparts higher proton conductivity, however due to the shorter side chain yields a similar crystallinity. This is not surprising as these respective equivalent weights lead to an almost identical graft density on the polymer backbone - approximately 1 side chain for every 14 backbone carbon atoms. Because these membranes have been shown to be near the optimal equivalent weight that balances proton conductivity and mechanical stability, they were chosen as good candidates to more broadly compare the two classes of polymer.

3.2 Imaging Hyflon under Varying Relative Humidity

To begin with, we collected phase images of Hyflon Ion under three different regimes of water content and compare to our previous data on Nafion 212. Compared to previous scanned probe studies of Nafion over a range of humidities,[10] there is little qualitative difference between the structure of Nafion and Hyflon when equilibrated at ambient conditions. Hyflon shows an average domain size of 110 nm^2 at ambient conditions, comparable to the 93.6 nm^2 reported for Nafion. Domains cover 25.6% of the surface compared to 19% for Nafion and the density of domains

was lower, ranging from 1.1 to 1.5 per 1000 nm^2 instead of 2.0 to 2.7 per 1000 nm^2 in Nafion[10,11] The lower equivalent weight (higher ion exchange capacity) of Hyflon yields a larger volume fraction of water and is expected to confer a larger amount of hydrophilic surface area, which our results confirm.

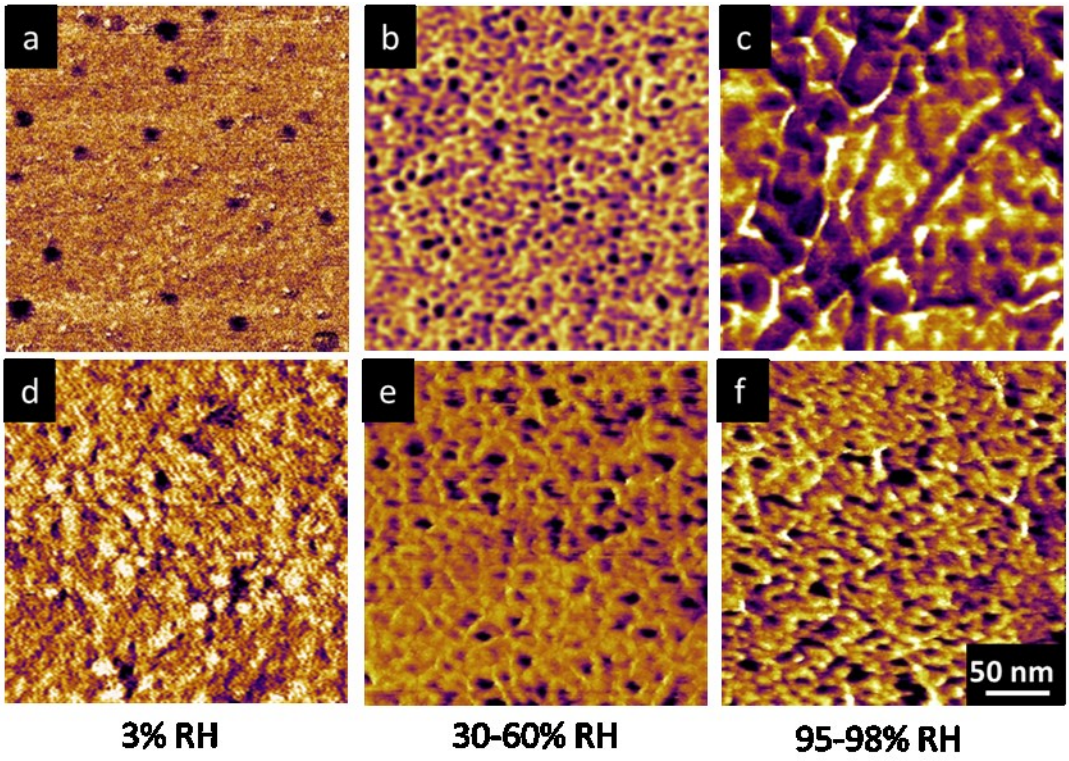

Figure 3.2 AFM phase images of Nafion 212 (a-c) and Hyflon Ion E87-05 (d-f) at dehydrated (a,d), ambient (b,e), and hydrated (c,f) states. Dehydrated images were collected in repulsive mode while all other images were collected in attractive mode.

Hyflon E87-05 has an equivalent weight of 870 g/mol whereas Nafion 212 has an equivalent weight of 1050 g/mol. Our results equate to a ~30% increase in hydrophilic surface area for a ~20% increase in ion exchange capacity. Additionally, the cluster-network model proposed by Gierke predicts a linear relationship between

the equivalent weight of the polymer and the volume of individual ionic clusters. [12,13] This fits well with the larger size of individual hydrophilic domains that we observe. The higher room temperature proton conductivity observed in similar SSC membranes is a product of this reduced equivalent weight.[5] The reduced occurrence of domains is likely tied to the larger size and broader distribution of domain sizes in Hyflon as compared to Nafion. This result is consistent with X-ray scattering data obtained by Kreuer et al. which shows a broader ionomer peak at lower scattering vectors for Dow 858, a SSC membrane similar to Hyflon Ion.[9]

Images of Nafion® 212 equilibrated with a high RH atmosphere show the formation of large fiber or worm-like features covering much of the surface[10]. Remarkably, few if any of these features are observed in Hyflon. The only change observed in Hyflon at high relative humidity is an increase in the amount of hydrophilic surface area from 25.6% to 31.1%. This increase agrees well with the increase in volume fraction of water observed over a similar range of humidity.[9] This increase appears to be caused by an increase in size of the hydrophilic domains rather than a reorganization of domains (i.e. swelling.) Kreuer et al. also observed a smaller shift in the ionomer peak with increasing water content for Dow 858 relative to Nafion,[9] implying a smaller average change in size of individual ionic clusters. This is consistent with the reduced amount of rearrangement we observe by AFM.

At low water contents we see a pronounced loss of hydrophilic surface area for Hyflon Ion as was observed in Nafion. The hydrophilic surface area of Hyflon drops

to 11.6%; whereas our study of Nafion yielded a value of only 5%.[10] Membrane water content is typically expressed as λ where λ is the molar ratio of H_2O to SO_3^- groups in the membrane. In previous water sorption experiments, both membranes were shown to have a similar λ value at low RH conditions[9]. The same λ value corresponds to a larger volume fraction of water in Hyflon® due to its lower equivalent weight. This may partially explain the greater area of hydrophilic surface domains in dehydrated Hyflon compared to dehydrated Nafion, and implies better water retention in Hyflon. In addition to a greater surface coverage of hydrophilic domains, we notice a different average size and occurrence of domains in Hyflon. In contrast to Nafion, Hyflon undergoes a shrinking of hydrophilic domains, while they maintain a similar occurrence. This implies that the mechanism of dehydration is more uniform in Hyflon and that less rearrangement of the surface is occurring, likely due to the reduced side chain mobility in Hyflon. Our observations suggest that in Hyflon, the network of hydrophilic domains is better preserved at low RH which explains the higher bulk proton conductivity of Hyflon at low RH as compared to Nafion.[6]

We next took cross sections of each membrane by the same cryofracture technique described earlier in order to compare the interior morphology of both membranes to their surface morphology. We notice a distinct difference in the interior morphology for both membranes. The average hydrophilic domain size increases significantly which in turn reduces the occurrence of domains. The average hydrophilic surface area is also higher in the interior of the membrane relative to the

surface (33 vs 25% for Hyflon and 31 vs 21% for Nafion). This is not surprising, as the air interface is more hydrophobic than the water and polymer in the interior of the membrane. This causes a surface with a relatively higher hydrophobic character to form when these membranes are dispersion cast. This is an important consideration, as this smaller surface hydrophilicity will likely limit the proton current in the through-plane direction during operation. We also notice that in the interior of the membrane, there is a joining of adjacent hydrophilic domains to form bands which stretch in the through membrane direction. This could explain the often anisotropic proton conductivity and water diffusion coefficients that are observed in these materials.

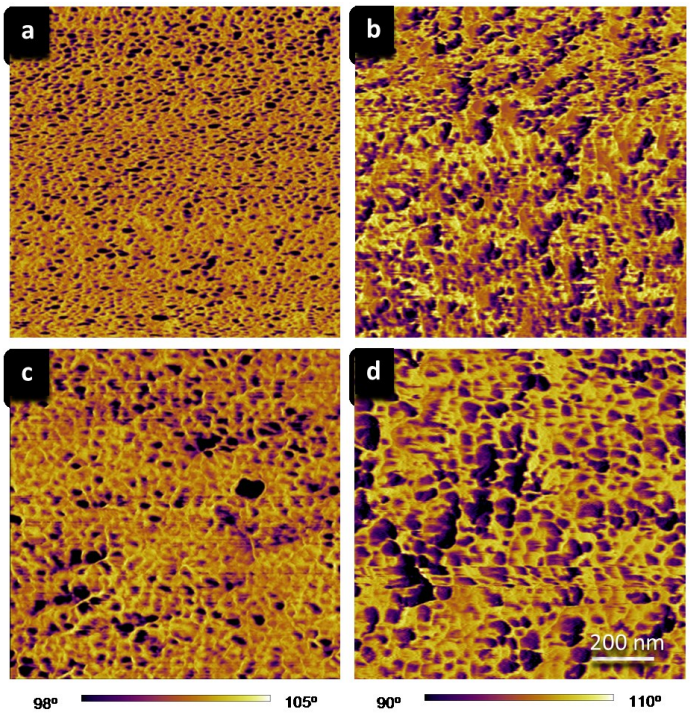

Figure 3.3 AFM phase images of the membrane surface (a,c) and of cryofractured cross-sections (b,d) of Nafion 212 (a,b) and Hyflon Ion E87-05 (c,d).

An important consideration when interpreting these cryofractured cross-sections is the effect of freezing water on the membrane microstructure. When submerged in liquid nitrogen, it is almost certain that the water inside the membrane freezes, in spite of the high ionic content and spatial confinement. This causes expansion of the water and, as a result, the hydrophobic polymer matrix. It is thus unclear, to what degree the increased cluster size may be an effect of this freezing expansion. To investigate this effect, we also examined the membrane surface after freezing in liquid nitrogen and found no SAXS experiments would represent a good way to probe the average cluster size as a function of these conditions, but this is beyond the scope of this work.

3.3 Imaging in Water and Under Methanol Solution

We next compared both membranes in water and in methanol solutions. Similar to high RH environment, we see little if any fibril formation in sharp contrast to Nafion where abundant fibril formation occurs. This reduced amount of surface rearrangement is a good sign for the long term durability of Hyflon as it implies an ability to absorb water without introducing roughness to the membrane-electrode interface. One unique feature we notice in Hyflon is a series of low lying height features across the membrane surface which appear to be oriented in one direction. These were observed equally across all water contents, and it seems likely that they are side effects of the extrusion process used to cast these membranes. However, we conducted imaging of Nafion 105 and 117 which are extruded LSC membranes and

found no evidence of these features, and a similar fibrillar morphology to that observed in Nafion 212. An example of image of Nafion 117 under DI water is shown in figure 3.5. This tells us that there is a significant difference in morphology between these two membranes which is independent of the casting process.

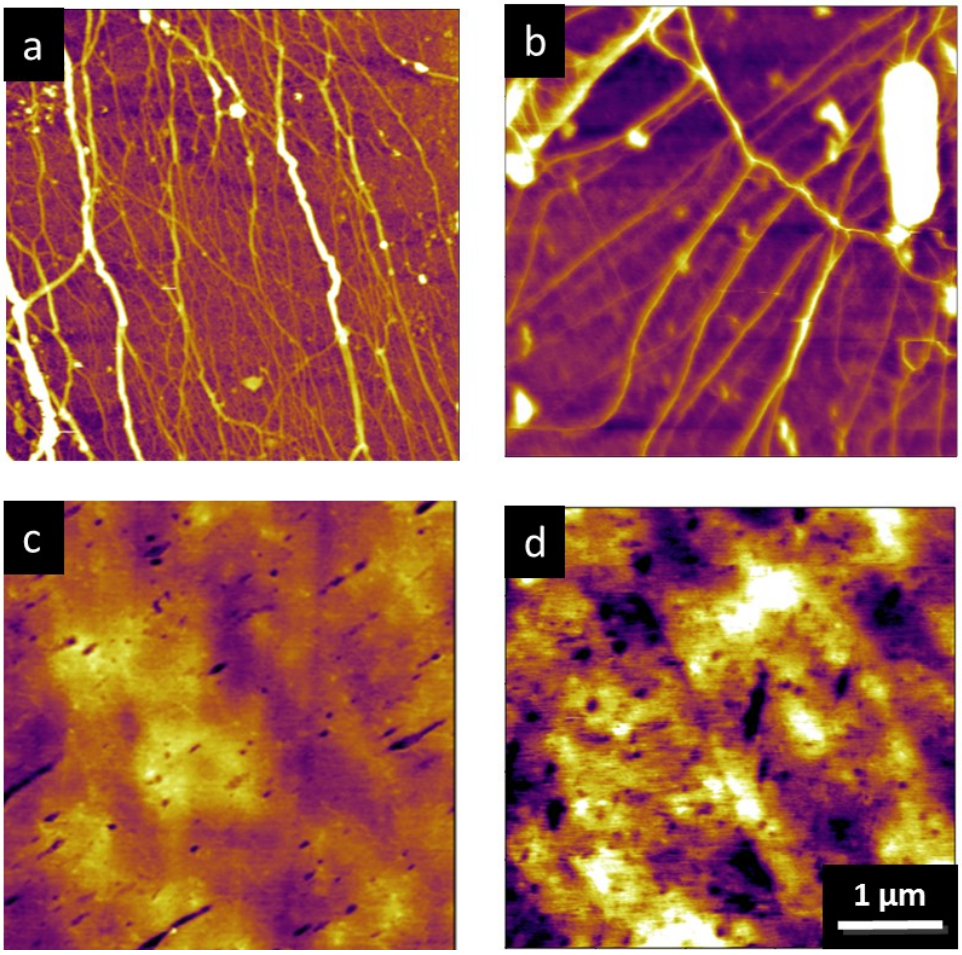

Figure 3.4: Topographic AFM images of Nafion 212 (a,b) and Hyflon Ion E87-05 (c,d) under DI water (a,c) and 50% methanol (b,d).

It is very likely that both membranes undergo a similar type of swelling in liquid environment. This is, however, difficult to observe or quantify microscopically in

Hyflon by AFM due to a lack of any type of reference features to act as a yardstick. Bulk swelling measurements of both membranes were conducted, and while they are by no means exhaustive, they show roughly similar degrees of in-plane swelling (~20%) when moving from ambient conditions to water equilibrated.

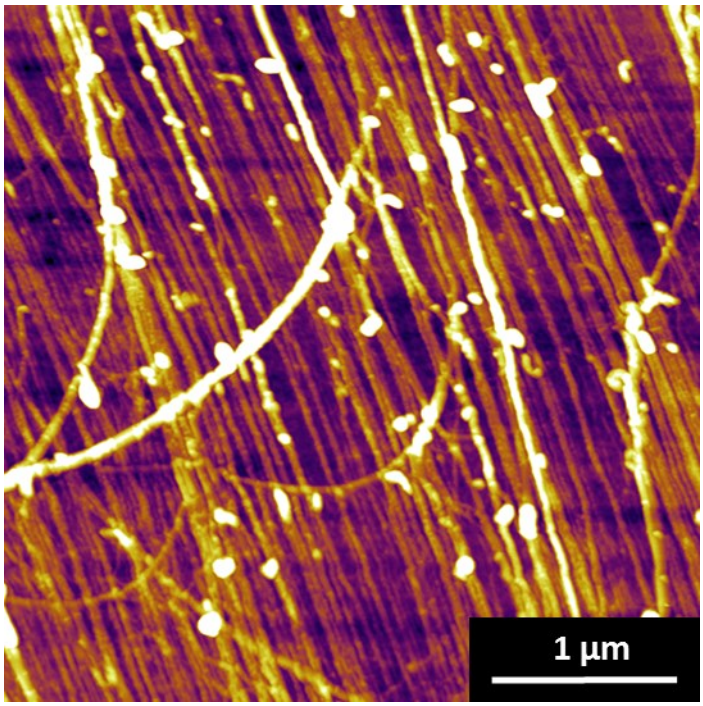

Figure 3.5: Topographic AFM images of Nafion 117, an extruded membrane under DI water.

In the case of alcohol environments, we saw that Hyflon swells macroscopically by ~13% when moved from water to 50 vol% methanol, less than the 22% increase seen in Nafion, implying a lower but still substantial methanol uptake without any measurable change in surface roughness. This may be caused by the reduced equivalent weight of Hyflon and the resulting smaller hydrophobic volume fraction that is available for solvation by methanol and other organic solvents. It could also be

that the reduced rotational mobility of side chains predicted in modelling[14] inhibits surface rearrangement in Hyflon during swelling.

3.3 Conductive Imaging

To investigate the effect of morphology on the fuel cell performance of each membrane, conductive probe AFM was employed on half fuel cells with hydrogen supplied to a carbon cloth electrode on the opposite side of the membrane as the AFM tip. As mentioned previously, the large worm-like feature in the Nafion image shows no current response. As in phase imaging, many features were observed in Nafion 212 but not in the Hyflon Ion membrane. However, small non-conductive areas were observed across the surface of both membranes which may correspond to hydrophobic domains or hydrophilic domains with poor connectivity.

Perhaps more importantly, the ability of the surface of Nafion to rearrange and form worm-like features at high water content provides a possible performance degradation mechanism. Humidity cycling tests conducted on membrane electrode assemblies containing Nafion have found a rapid performance loss which was attributed to membrane swelling and shrinking.[15] This specific type of swelling, where considerable roughness is introduced into the membrane-electrode interface would almost certainly add additional resistance and be deleterious to fuel cell performance. The higher glass transition temperature of Hyflon (160°C vs 110-130°C for Nafion)[2] could explain why surface rearrangement and the formation of worm-like features occurs in the LSC membrane, but not the SSC membrane. This

gives the SSC membrane an important advantage in durability in addition to improved proton conductivity.

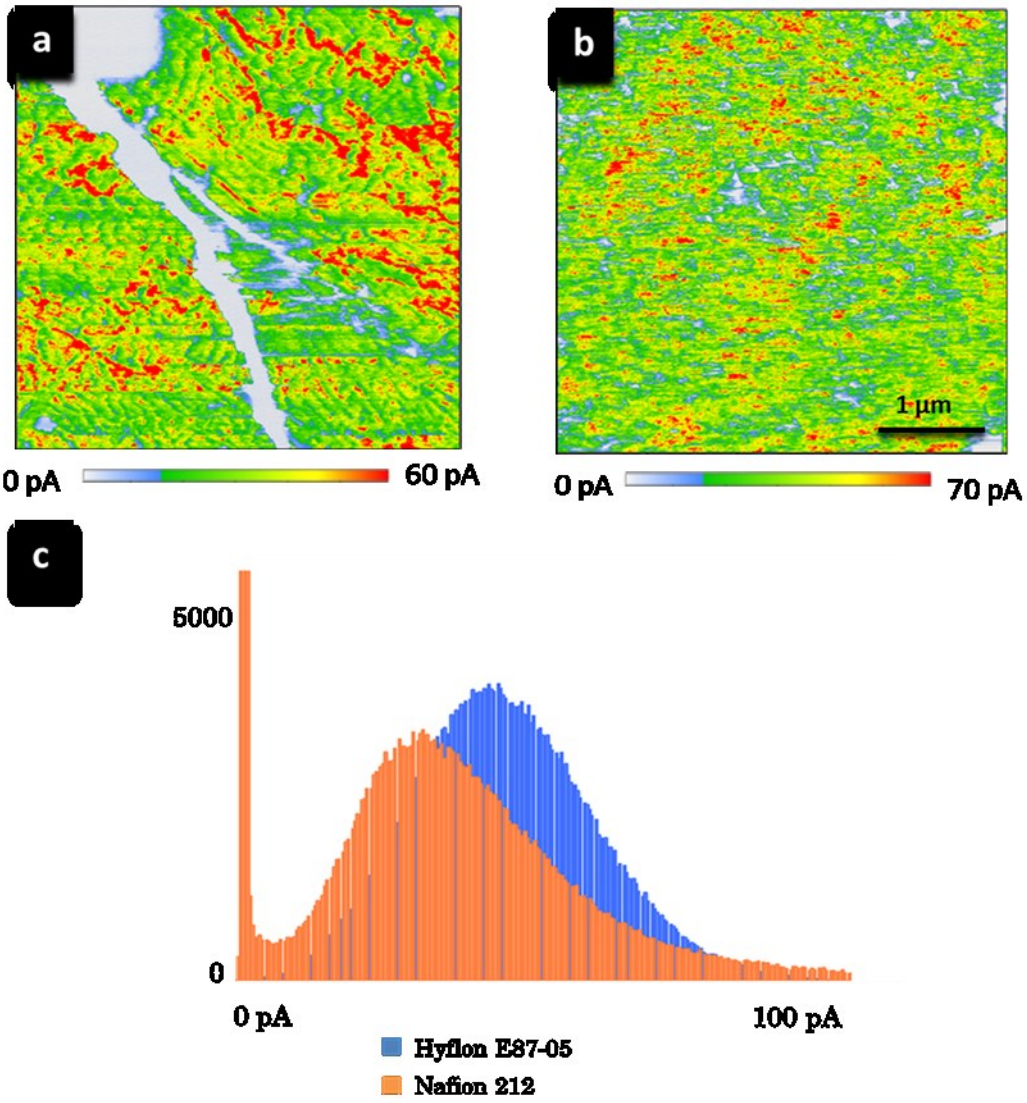

Figure 3.6: Conductive AFM images of Nafion 212 (a) and Hyflon Ion E87-05 (b) taken at 80 % relative humidity and 50 C. (c) Histograms of each conductive AFM image.

The conductivity images for each membrane exhibited a range of currents which followed a Gaussian distribution, with Hyflon Ion E87-05® exhibiting a higher

average current than Nafion 212® (70 pA vs. 62 pA) under identical conditions as shown in Figure 10. This difference in average current agrees well with the reported difference in bulk conductivity values under the temperature and humidity that these measurements were conducted under. Our cp-AFM's ability to differentiate between two materials with similar proton conductivity is a good indicator of its quantitative accuracy.

3.4 Conclusions

The question of why SSC membranes show improved performance over LSC membranes has been the subject of several studies.[2,3,9,14] Our results indicate an increased percentage of hydrophilic surface area in Hyflon due to its lower equivalent weight, which yields a higher proton conductivity at ambient conditions. At dehydrated conditions, hydrophilic surface area is retained, implying more pathways for proton conduction and higher performance than Nafion under the same conditions. At high water contents and in methanol solutions, we observe very little morphological rearrangement in Hyflon during swelling, in sharp contrast to Nafion. This improved swelling behavior is likely tied to the higher T_g of Hyflon. The greater stability of Hyflon should allow it to perform better under variable operating conditions.

The fact that SSC materials show improved properties gives important design information for future proton exchange membranes. In the case of Hyflon, efficient packing of polymer chains allows for better swelling behavior without sacrificing

proton conductivity. PFSA materials with even shorter side chains may be able to pack even more efficiently, allowing even lower equivalent weight membranes to be used. It is unclear, however, if the synthesis of such materials would be possible or economical. Cross-linked polymers[16,17], polymer/inorganic composite systems[18,19], as well as novel wholly inorganic membranes[20,21], provide an alternate route to improving swelling behavior without reducing the volume available for proton conduction.

References

(1) Prater, K. The Renaissance of the Solid Polymer Fuel Cell. *Journal of Power Sources* **1990**, *29*, 239–250.

(2) Tant, M. R.; Darst, K.P.; Lee, K. D.; Martin, C. W. *Structure and Properties of Short-Side-Chain Perfluorosulfonate Ionomers. In Multiphase Polymers: Blends and Ionomers*; ACS Symposium Series 395.; American Chemical Society: Washington, DC, 1989.

(3) Arcella, V.; Troglia, C.; Ghielmi, A. Hyflon Ion Membranes for Fuel Cells. *Ind. Eng. Chem. Res.* **2011**, *44*, 7646–7651.

(4) Deng, Z. D.; Mauritz, K. A. Dielectric Relaxation Studies of Acid-Containing Short-Side-Chain Perfluorosulfonate Ionomer Membranes. *Macromolecules* **1992**, *25*, 2369–2380.

(5) Eisman, G. A. The Application of Dow Chemical's Perfluorinated Membranes in Proton-Exchange Membrane Fuel Cells. *Journal of Power Sources* **1990**, *29*, 389–398.

(6) Merlo, L.; Ghielmi, A.; Cirillo, L.; Gebert, M.; Arcella, V. Membrane Electrode Assemblies Based on HYFLON ® Ion for an Evolving Fuel Cell Technology. *Separation Science and Technology* **2007**, *42*, 2891–2908.

(7) Gordano, A.; Arcella, V.; Drioli, E. New HYFLON AD Composite Membranes and AFM Characterization. *Desalination* **2004**, *163*, 127–136.

(8) Gebel, G.; Moore, R. B. Small-Angle Scattering Study of Short Pendant Chain Perfuorosulfonated Ionomer Membranes. *Macromolecules* **2000**, *33*, 4850–4855.

(9) Kreuer, K. D.; Schuster, M.; Obliers, B.; Diat, O.; Traub, U.; Fuchs, A.; Klock, U.; Paddison, S. J.; Maier, J. Short-Side-Chain Proton Conducting Perfluorosulfonic Acid Ionomers: Why They Perform Better in PEM Fuel Cells. *Journal of Power Sources* **2008**, *178*, 499–509.

(10) O'Dea, J. R.; Economou, N. J.; Buratto, S. K. Surface Morphology of Nafion at Hydrated and Dehydrated Conditions. *Macromolecules* **2013**.

(11) O'Dea, J. R.; Buratto, S. K. Phase Imaging of Proton Exchange Membranes under Attractive and Repulsive Tip−Sample Interaction Forces. *The Journal of Physical Chemistry B* **2011**, *115*, 1014–1020.

(12) Gierke, T. D.; Munn, G. E.; Wilson, F. C. The Morphology in Nafion Perfluorinated Membrane Products, as Determined by Wide- and Small-angle X-ray Studies. *Journal of Polymer Science: Polymer Physics Edition* **1981**, *19*, 1687–1704.

(13) Hsu, W. Y.; Gierke, T. D. Ion Transport and Clustering in Nafion Perfluorinated Membranes. *Journal of Membrane Science* **1983**, *13*, 307–326.

(14) Hristov, I. H.; Paddison, S. J.; Paul, R. Molecular Modeling of Proton Transport in the Short-Side-Chain Perfluorosulfonic Acid Ionomer. *The Journal of Physical Chemistry B* **2008**, *112*, 2937–2949.

(15) Two Fuel Cell Cars in Every Garage? *Electrochem. Soc. Interface (USA)* **2005**, *14*, 24–3535.

(16) Guo, Q. H.; Pintauro, P. N.; Tang, H.; O'Connor, S. Sulfonated and Crosslinked Polyphosphazene-Based Proton-Exchange Membranes. *J. Membr. Sci.* **1999**, *154*, 175–181.

(17) Ye, Y.-S.; Yen, Y.-C.; Cheng, C.-C.; Chen, W. Y.; Tsai, L.-T.; Chang, F.-C. Sulfonated Poly(ether Ether Ketone) Membranes Crosslinked with Sulfonic Acid Containing Benzoxazine Monomer as Proton Exchange Membranes. *Polymer* **2009**, *50*, 3196–3203.

(18) Ramani, V.; Kunz, H. .; Fenton, J. . Investigation of Nafion®/HPA Composite Membranes for High Temperature/low Relative Humidity PEMFC Operation. *Journal of Membrane Science* **2004**, *232*, 31–44.

(19) Jalani, N. H.; Dunn, K.; Datta, R. Synthesis and Characterization of Nafion®-MO2 (M = Zr, Si, Ti) Nanocomposite Membranes for Higher Temperature PEM Fuel Cells. *Electrochimica Acta* **2005**, *51*, 553–560.

(20) Athens, G. L.; Ein-Eli, Y.; Chmelka, B. F. Acid-Functionalized Mesostructured Aluminosilica for Hydrophilic Proton Conduction Membranes. *Adv. Mater.* **2007**, *19*, 2580–2587.

(21) Moghaddam, S.; Pengwang, E.; Jiang, Y.-B.; Garcia, A. R.; Burnett, D. J.; Brinker, C. J.; Masel, R. I.; Shannon, M. A. An Inorganic-Organic Proton Exchange Membrane for Fuel Cells with a Controlled Nanoscale Pore Structure. *Nat Nano* **2010**, *5*, 230–236.

Chapter 4: Investigation of 3M Membranes for High Temperature Fuel Cell Operation

4.1 Introduction:

Proton exchange membrane fuel cells (PEM-FC's) are a promising power source that is under development for automotive and stationary applications. Currently these devices suffer from high system cost and poor durability relative to internal combustion engines which have impeded commercialization. One route to addressing these factors is to create cells that can operate at higher temperatures (>100C). This would mitigate several problems inherent to fuel cells, such as slow oxygen reduction reaction kinetics at the cathode and the propensity for carbon monoxide poisoning to occur at both electrodes. The challenge to accomplishing this goal lies in the PEM itself. These membranes consist of phase separated polymers with a hydrophilic proton conducting phase inside of a hydrophobic polymer matrix. The most commonly employed membrane is Nafion, a perfluorosulfonic acid (PFSA) membrane. While Nafion shows good performance, it has several drawbacks especially for high temperature operation. At high temperatures, water is lost from the hydrophilic phase and ionic conductivity from anode to cathode drastically

decreases. This dehydration also accelerates chemical degradation processes which lead to permanent performance loss in the membrane. Additionally, high temperatures put Nafion close to its glass transition temperature (~110C) which causes a loss of mechanical strength.[1,2]

Water retention and proton conductivity can be increased by using lower equivalent weight (EW) membranes but this in turn reduces the length of crystallizable polymer backbone segments which decreases the mechanical strength of the membrane.[3,4] Low EW membranes also swell excessively at high humidity causing dimensional stress which can lead to accelerated degradation of the membrane electrode interface.[5] All PEM's must balance ionic conductivity with mechanical strength in this way, and numerous approaches have been taken to impart additional mechanical strength to membranes such as forming organic/inorganic composites[6–9], using highly porous polymer scaffolds[10], and crosslinking polymers[11–13]. While these methods can create mechanically robust materials, they often do so at the expense of proton conductivity.

3M has developed a new approach to this problem where a PFSA precursor is imparted with a new side chain functionality that contains two acidic protons per side-chain instead of one.[14] This in theory allows for a membrane with a higher acid content (lower EW) without sacrificing the crystallinity of the resulting membrane. Hamrock and coworkers have shown that these perfluoro-imide acid (PFIA)

membranes yield excellent mechanical stability compared to PFSA membranes of a similar equivalent weight.

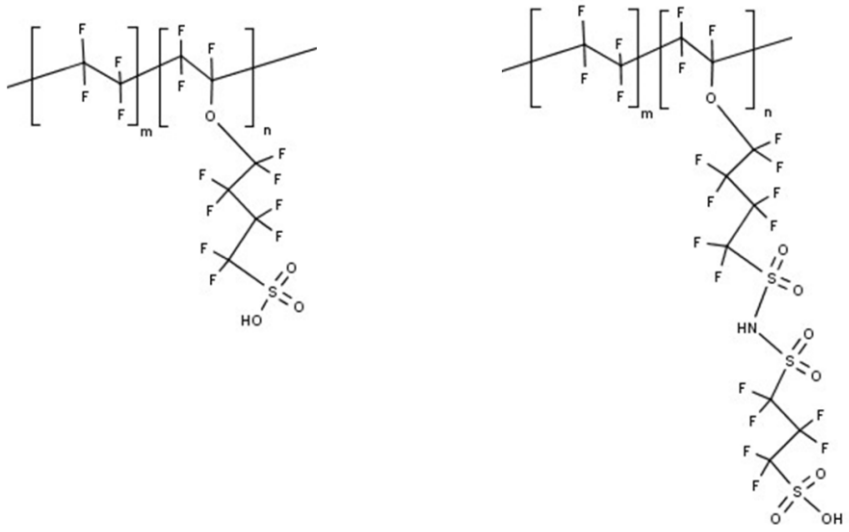

Figure 4.1: Chemical Structures of the 3M PFSA (left) and PFIA (right).

Bulk conductivity measurements have already shown that a PFIA membrane has higher proton conductivity than a PFSA membrane made from the same polymer precursor due to an increased concentration of protons.[14] It has also been shown that this leads to increased performance at elevated temperatures. Modeling studies have also determined a distinct dissociation behavior and hydrogen bond connectivity between the two acid groups.[15] What remains to be seen is how these observations are tied to membrane morphology, swelling behavior, and spatial distribution of proton current coming through the membrane. It also remains to be seen if the membrane morphology is stable across the wide range of water contents that can be experienced during fuel cell operation. Understanding the changes in these nano-

scale properties will help to determine to what degree the multi-acid sidechain architecture meets the desired design goals of increased proton conductivity without a loss in mechanical stability under fuel cell operating conditions.

Here we employ tapping mode and conductive probe atomic force microscopy (cp-AFM) as tools to investigate the nanoscale morphology and proton conductivity of a 3M PFIA membrane as a function of relative humidity. As a point of comparison, we also investigate a 3M PFSA made from an identical polymer precursor to directly see the effect of the additional acid group and longer sidechain on the properties of interest. Because of the large range of relative humidity (RH) that can be present in a fuel cell, we employ a closed fluid cell and investigate morphology over the range 3-95% RH with a specific focus on the extremes of this range. Imaging at extensively dehydrated conditions allows us to assess the membrane's water retention and to see how the hydrophilic phase changes under these conditions. Conversely, very high RH conditions allow us to evaluate the mechanical stability of this membrane when subjected to various forms of swelling. Cp-AFM then allows us to obtain spatially resolved proton conductivity maps under a similar set of conditions and observe directly how membrane morphology is tied to proton conductivity. Through this we are able to see evidence of the improved water retention and proton conductivity in the PFIA at elevated temperature, but at high RH conditions see evidence of a nearly continuous hydrophilic phase which may indicate unfavorable swelling behavior.

4.2 Experimental:

For these experiments, we used similar scan imaging parameters to those used to characterize Nafion and Hyflon in previous chapters. In this work we used the same conductive imaging cell, but imaged at increased temperatures. Experiments were conducted up to 200 degrees, at which point no membrane maintained conductivity, and the humidity in the cell was essentially zero. Humidified hydrogen was supplied via a gas flow channel under the electrode at 50 mL/minute and humidified air was supplied over the membrane surface at 100 mL/minute while scanning. Using a humidity sensor (Honeywell) we found that the humidity in the chamber was 80% at room temperature and decayed to ~3% at 160C. A graph of the humidity to temperature ratio for our cell is shown below.

For experiments using dry gas feeds, both flow channels were passed through a desiccator column yielding a relative humidity of 6% at room temperature. At each temperature interval, the sample was allowed to equilibrate with the atmosphere for 30 minutes prior to imaging which was observed to coincide with stable RH values. A positive bias of 1 V was applied to the sample for all images and data reported here, but a linear relationship between current and bias voltage was observed at positive bias.

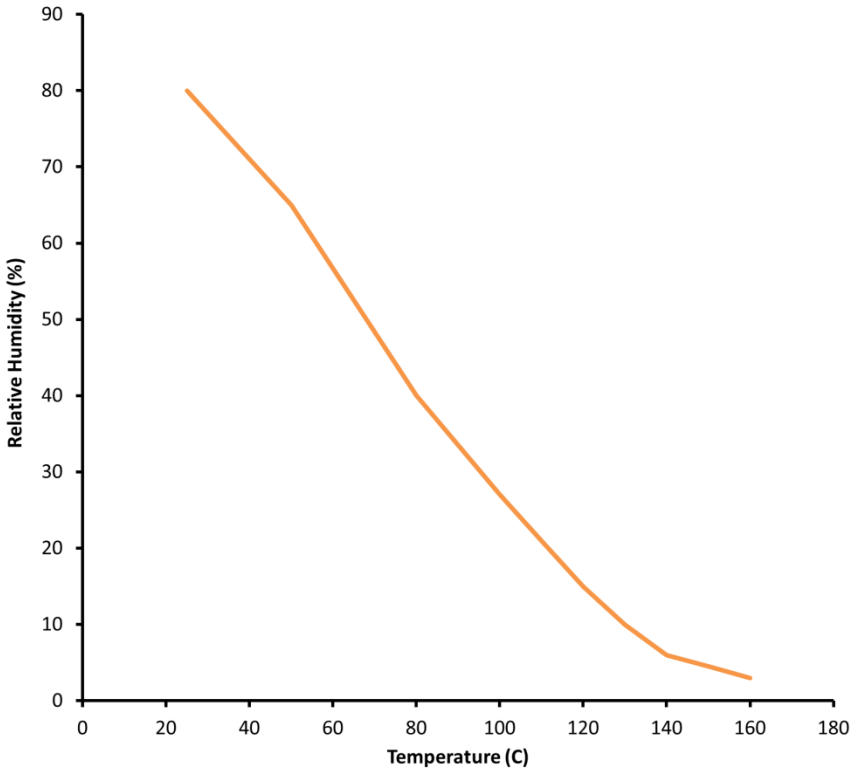

Figure 4.2: Relative humidity versus temperature relationship for our sample chamber with membrane sample and flow rates of 50 mL per minute humidified H_2 (g) and 100 mL per minute humidified air at anode and cathode respectively.

4.3 Phase Imaging of 3M Ionomers

Our first goal was to evaluate the morphology of the 3M PFIA ionomer compared to its PFSA counterpart. Since both polymer membranes are made from the same sulfonyl amine precursor, one important question to answer is whether the additional acid group on the PFIA has a significant effect on the resulting membrane morphology. For this we employed tapping mode AFM imaging under a wide range of relative humidity as we have used previously to characterize other PFSA polymers.[16,17] At ambient conditions we already notice both polymers showing

slightly different morphology. Both polymers show a similar degree of phase contrast, implying similar mechanical properties of both the hydrophilic and hydrophobic domains. We see a well-defined hydrophilic pore structure in both polymers with each showing a similar fraction of hydrophilic surface area – 22% for the PFIA and 21% for the PFSA. This is an interesting result as the lower equivalent weight and higher water uptake observed in the PFIA polymer might be expected to confer a higher hydrophilic surface area, but they are almost identical. Despite having a similar amount of hydrophilic surface area, we notice a significant difference in the size of individual hydrophilic domains. Analysis of phase images similar to figure 1 showed that the average radius for hydrophilic domains in the PFIA membrane was 8.2 nm versus 7.7 nm for the PFSA. The cluster network model set forth by Gierke and Hsu[18,19] predicts that cluster size should increase as equivalent weight decreases, which is what we observe here. This is also consistent with previous work by our group on other, higher E.W. PFSA's, which both showed smaller average domain sizes. It is worth pointing out, however, that the domains we observe are not the same as the clusters inferred from X-ray scattering. The domains we see are on the order of 10-15 nm in diameter while individual clusters are 3-4nm. This has been explained by various models by the coalescence of individual clusters to form a larger hydrophilic phase.[20–22] and by a different morphology at the membrane surface than in the bulk material.[23] What we can infer from this information, however, is that a larger cluster size in the bulk is also linked to a larger average domain size at the surface.

Since the PFIA is designed to perform under low relative humidity and high temperature, we next evaluated the water retention ability of the PFIA polymer by conducting imaging under heavily dehydrated conditions and comparing to the PFSA membrane. Our previous experience with PFSA polymers has shown that imaging under these conditions requires moving from the attractive imaging regime (phase > 90) to the repulsive imaging regime (phase < 90) in order to observe phase contrast between hydrophilic and hydrophobic domains without coupling strongly to topography.[16,17,24] This is likely related to the fact that in attractive mode, only the first atomic layer is being probed mechanically, whereas in repulsive mode the probe depth increases to a few nm.[25] In short this implies that other PFSA's such as Nafion have essentially no water at the surface and that the phase contrast we see is due to water in subsurface domains in the first few nanometers. In the case of both the PFSA and PFIA, we were able to achieve stable, attractive mode phase imaging without significant coupling to topography, which alone implies that both membranes exhibit better surface water retention. At dehydrated conditions, the PFIA still exhibits 9% hydrophilic surface area under attractive conditions, whereas the PFSA exhibits 3.9% hydrophilic surface area. The average domain size in the PFSA decreases considerably to 3.7 nm radius, while the PFIA undergoes less of a decrease to 6.7nm. The occurrence of domains in the PFSA is also markedly lower than the PFIA at 195 domains per square micron versus 390. We attribute these results to better water retention and a hydrophilic phase which is stable even under extremely dehydrated conditions.

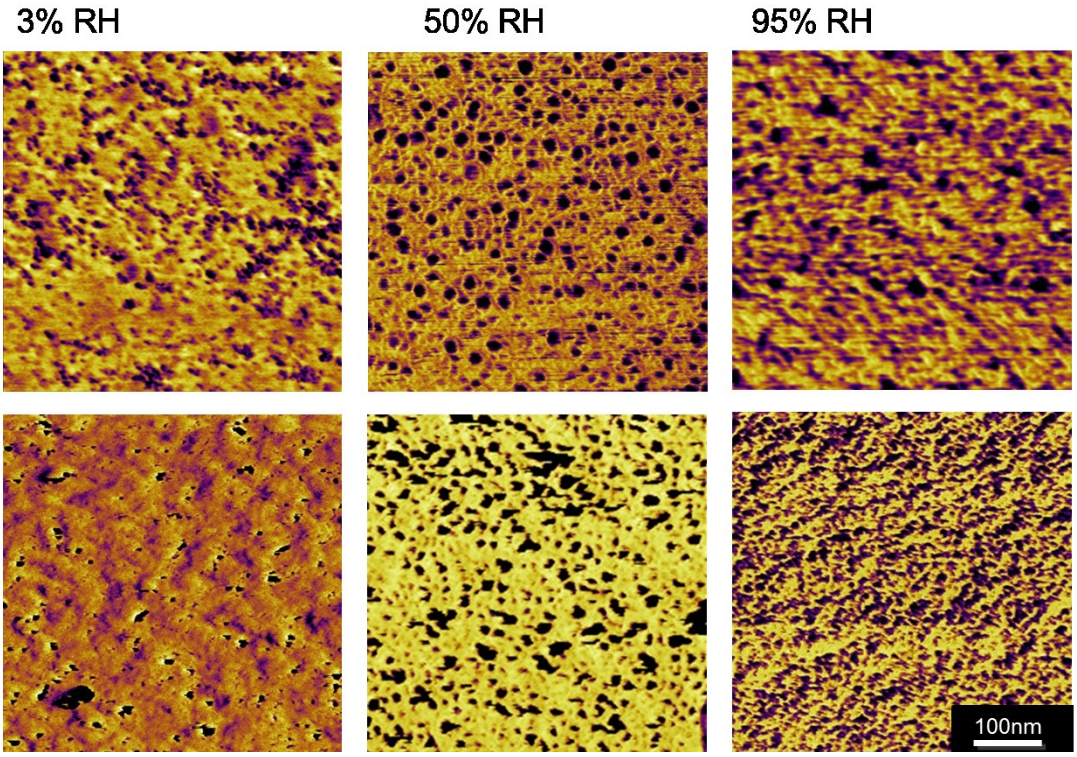

Figure 4.3: 500 nm phase images of 3M 625 EW PFIA (top) and 825 EW PFSA (bottom) under dehydrated (3% RH) (a,d) ambient (50% RH)(b,e) and hydrated (95%RH)(c,f) conditions. Dark areas correspond to hydrophilic domains while bright areas represent the hydrophobic polymer matrix.

One advantage of the PFIA polymer is that despite being able to effectively retain water, it should exhibit sufficient crystallinity due to polymer backbone packing so that it does not swell excessively at high water contents. This enables the use of lower EW PFIA polymers (625g/mol in this case) while maintaining sufficient mechanical strength. Schaberg and coworkers have already shown that these polymers exhibit higher crystallinity than a PFSA of equal equivalent weight.

In order to evaluate performance at high water contents, we equilibrated both membranes in water and imaged them in a high (95%) RH atmosphere. In both cases, we see an increase in hydrophilic surface area, consistent with a dilation of ionic clusters. Previous SAXS experiments on 3M PFSA polymers[26] and other PFSA membranes[23,18,27] have shown that the size of ionic clusters increases with increasing water content as is the case for many phase separated systems. By AFM, we notice an increase in hydrophilic surface area in the PFIA to 36% and in the PFSA to 33%. Particle analysis shows that the average size of hydrophilic domains greatly increases, especially in the PFIA. We also see a movement towards a near-continuous hydrophilic phase at the surface which is more pronounced in the PFIA, in contrast to the isolated hydrophilic domains at ambient and dehydrated conditions. While this continuous hydrophilic phase may be beneficial for proton conductivity, it has the potential to cause problems at the interface due to swelling induced mechanical strain or water accumulation inside the electrodes. It appears that while the PFIA retains similar mechanical properties to the corresponding PFSA, the additional acid group causes a small degree of additional swelling. This is something that needs to be taken into account when considering fuel cell applications for this membrane.

4.4 Conductive Imaging

We have already shown that qualitatively, both membranes follow a similar change in morphology but with a quantitative difference in hydrophilic surface area.

To more directly visualize the performance of these membranes under fuel cell operating conditions, we employed conductive probe AFM as described in our previous work.[16] At room temperature and 80% RH we noticed a substantially higher current in the PFIA as compared to the PFSA, likely due to the increased concentration of protons in the membrane. We also noticed the formation of large, non-conductive fibrils features in both membranes, similar to those observed in Nafion 212.[16,17] This is likely caused by the sample construction method where samples are hot-pressed at 130° C, close to their glass transition temperature, which leads to this structural rearrangement. As can be seen in Figure 3, these features are non-conductive indicating that they do not contribute to through-plane conductivity and thus fuel cell performance.

In order to evaluate the performance of these polymers at the designed operating conditions, we conducted cp-AFM imaging at elevated temperature and reduced humidity. We could not find a practical way to increase the temperature of our gas streams without introducing substantial electrical noise into the cp-AFM measurements. For this reason we used room temperature gas feeds and raised the temperature of the fluid cell which increased temperature and simultaneously decreased relative humidity. We found that at the flow rates used in this study, we achieved a relative humidity of 80% at 25°C which decays to ~25% at 100°C. Figure 4.2 shows the relationship between temperature and relative humidity at the conditions used in this study. Not surprisingly, in this temperature range, both membranes lost conductivity quickly as temperature was raised and did so at a rate

consistent with bulk ionic conductivity decreasing with decreasing relative humidity as was observed in previous measurements by the 3M group. Above 100°C, the decrease in conductivity was more rapid likely due to additional dehydration of the surface from being above the boiling point of water.

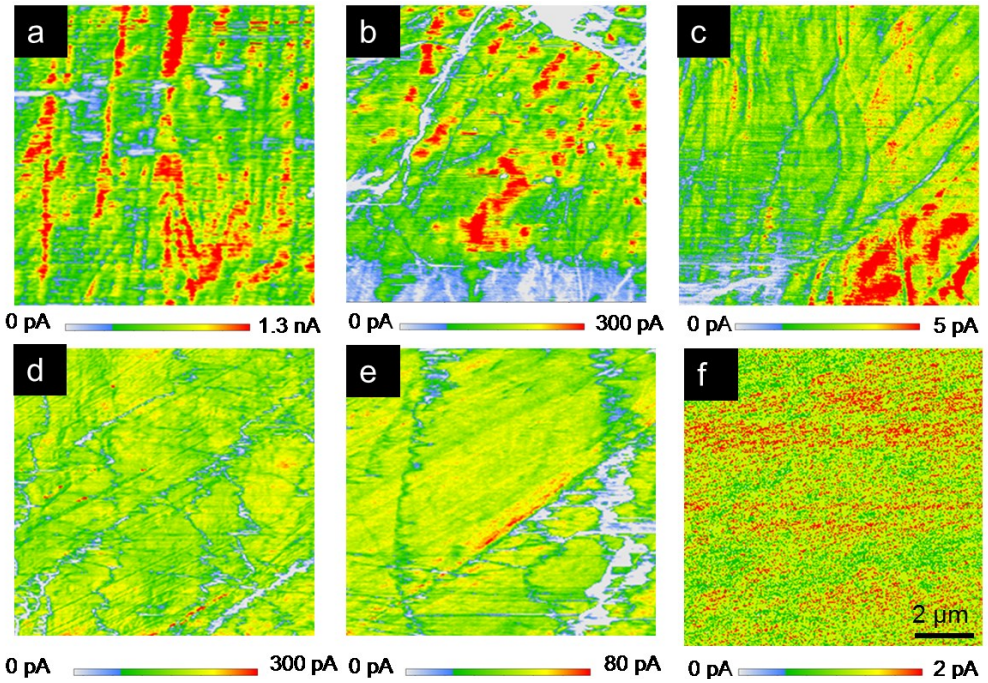

Figure 4.4: Large scale (10um) conductive probe AFM images of 3M PFIA (top) and PFSA (bottom). These were conducted using 50 mL of humidified hydrogen at the anode and 100 mL of humidified air at the cathode with cell temperatures of 25°C (a,d) 100°C (b,e) and 140°C (c,f). These increasing temperatures correspond to decreasing relative humidity in the sample chamber.

Figure 4.4 shows proton conductivity images of each membrane at 25, 100 and 140 C, showing the decay and eventually the complete loss of conductivity. We observed that the PFIA maintained a small amount of proton conductivity up to 160C whereas the PFSA lost all conductivity above 130C. This result appears to be in line

with our previous observations about the more hydrophilic character of the PFIA surface. Due to the current resolution of our setup, currents below 1pA could not be separated from noise and were not factored in to average currents.

As is readily apparent, the PFIA shows higher current values across all of the conditions explored in this study. This is not surprising, as the lower equivalent weight is expected to yield a higher density of proton charge carriers and thus higher proton conductivity. Interestingly, the PFIA shows much broader current distributions as well. This often was manifested as "hot spots" in the current images which were in the hundreds of nanometers to micron size range, and was most pronounced at high relative humidity. Our interpretation of these results is that there is a distinct morphology causing a non-uniform concentration of sulfonic acid groups near the surface. Figure 4.5 shows a series of histograms displaying the average currents from a 20 μm x 20 μm conductive AFM image at a range of temperature/RH conditions. We found that in practice there was a large variation in these average values, possibly due to imperfections in sample construction, especially at the membrane-electrode interface. As such we took several scans and report here the scans with the highest value at each temperature as these best represent an ideal construction without additional resistance being added. These histograms show the broader distribution of currents in the PFIA membrane, as well as a substantially smaller decrease in conductivity with decreasing relative humidity.

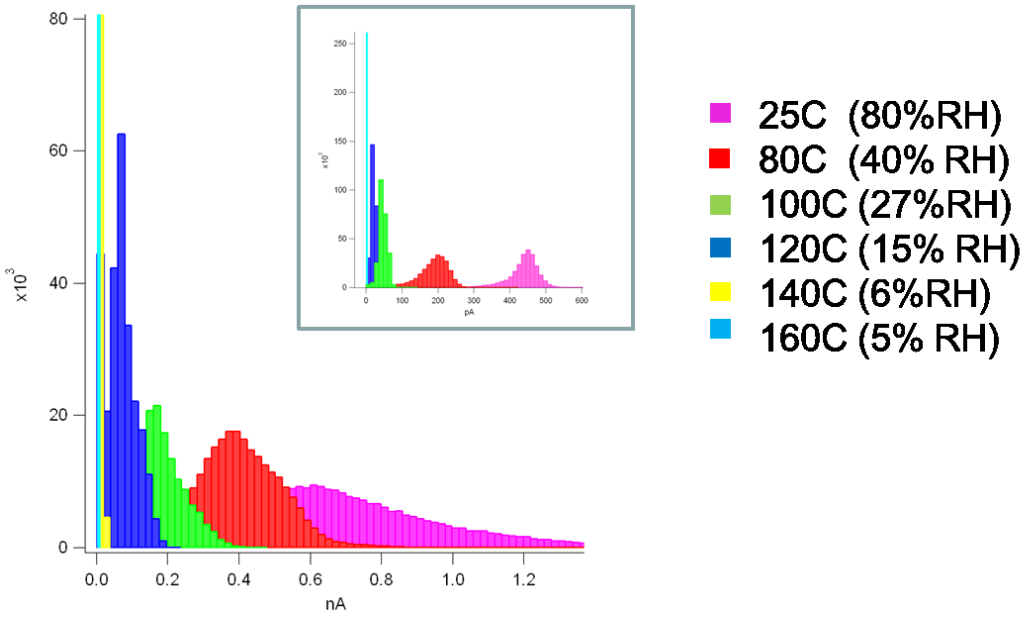

Figure 4.5: Histograms of current values at various temperatures for 3M 625 E.W. PFIA (left) and 825 E.W. PFSA (inset).

Figure 4.6 shows a plot of the log of average current in these experiments versus the relative humidity at each temperature, and shows how each of the membranes investigated shows a near linear decrease in the 80 – 20% RH range and then a more drastic decrease at very low relative humidity. The lower humidity range also corresponds to areas above the boiling point of water, so it is likely that under these conditions loss of water from the membrane surface is a large factor, even if some water is maintained in the bulk. As can be seen here, both the PFSA and PFIA show substantially higher proton conductivity than Nafion 212 and all membranes showed a decrease in conductivity that follows an exponential decay ($R^2 > 0.93$). By carefully monitoring the relative humidity inside of the sample chamber at each temperature

value, we were able to accurately relate each temperature to a relative humidity. It has been found in previous studies on Nafion that despite a theoretical increase in proton conductivity at elevated temperature, values at different temperatures but constant RH showed very little change. For this reason we assumed that temperature was not a factor in these experiments in order to plot our data as a function of relative humidity.

While the PFIA was able to reach higher temperatures and maintain measurable proton conductivity, this is mainly caused by the PFIA having higher conductivity to begin with and the limited current resolution of our instrument. If we instead look at the normalized proton conductivity (Figure 4.6b) we can see that in the extremely low RH/High temperature regime, both membranes lose a similar percentage of proton conductivity. The largest differences occurred at 100C and 120C (15% and 27% RH) where the PFIA shows about double the normalized proton conductivity of the PFSA. This implies that the PFIA shows the biggest improvement in performance in this temperature regime, which is generally regarded as a target range for higher temperature PEMFC's.[28]

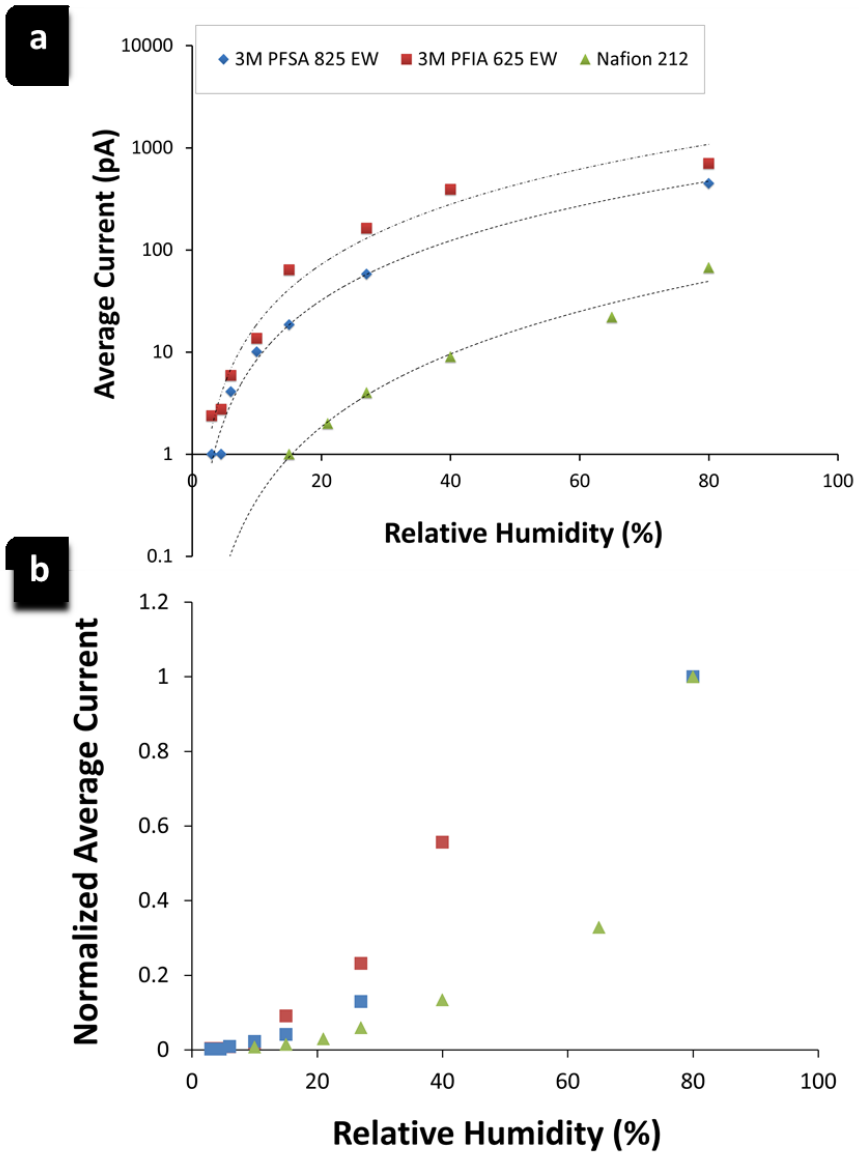

Figure 4.6: Average conductivity values on a logarithmic scale versus relative humidity (a) and average normalized current versus relative humidity (b) for PFIA, PFSA and Nafion 212 Membranes.

If we compare our AFM conductivity values to those acquired by Schaberg et al during bulk conductivity measurements, we see good quantitative agreement. This is impressive given the differences in the techniques being employed, bulk

measurements measure conductivity in the in-plane direction using a high frequency AC bias, while our AFM measurements are conducted in the through-plane direction under a constant DC bias. Figure 4.7 shows a plot of our conductive AFM data alongside theoretical currents based on bulk conductivity values and assuming a fixed tip-sample contact area (20nm radius half-sphere) and fixed membrane thickness for the PFIA and PFSA polymers. For example, the PFIA showed a conductivity of 120 mS/cm at 80% RH. If we apply our assumptions and assume no interfacial resistance or kinetic limitations, we get a theoretical value of 1.14 nA/V. The current we actually measure under these conditions is 704 pA/V, about 30% lower, but a very good estimate given the lack of information on the actual tip/sample contact area. It has been shown in other studies that at high relative humidity, a meniscus typically forms at the AFM tip, which causes an effective broadening of contact area.[29,30] At lower relative humidity, we see that the through plane conductivity is decreasing more rapidly than the in plane conductivity likely due to increased dehydration directly at the surface and a decreased electrochemical contact area with the AFM tip.

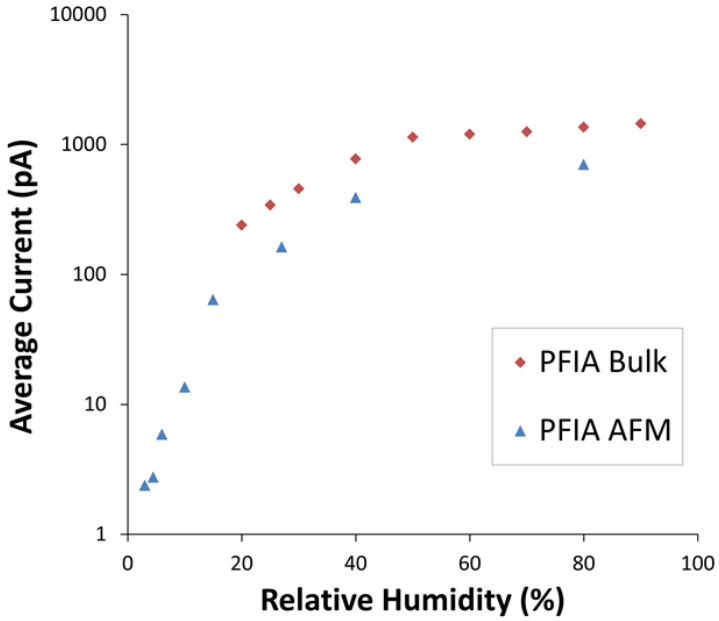

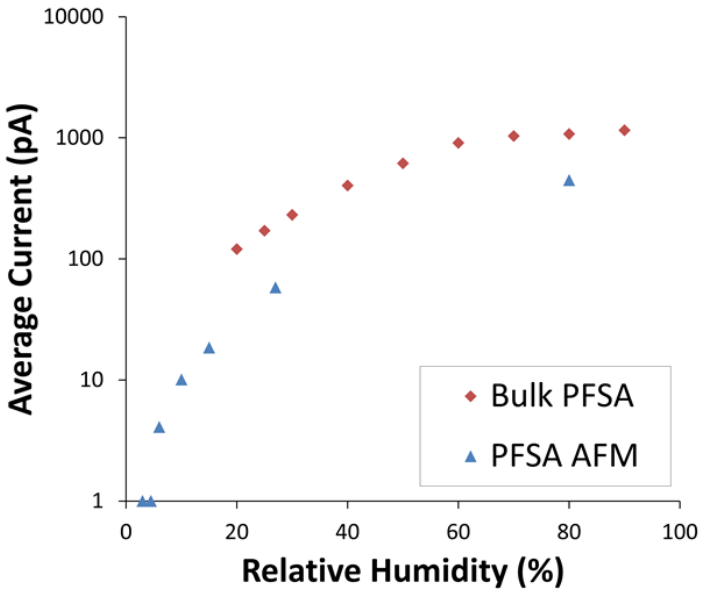

Figure 4.7: Comparison between average current values versus relative humidity from cp-AFM scans and bulk conductivity data from Schaberg et al. assuming a 20 nm ½ sphere as the AFM tip-sample contact area.

We conducted a similar set of experiments using dry gas feeds, where temperature was varied and humidity remained essentially constant (6% RH at 25C

and 3% RH at 150C). Under these conditions we notice a linear decrease in current as temperature is increased, due to increased evaporation at high temperatures. These measurements highlight an important consideration when interpreting bulk conductivity measurements of ionomer materials. During fuel cell operation, the surface properties of the membrane ultimately dictate through-plane conductivity and the performance of the fuel cell and need to be considered when evaluating these materials.

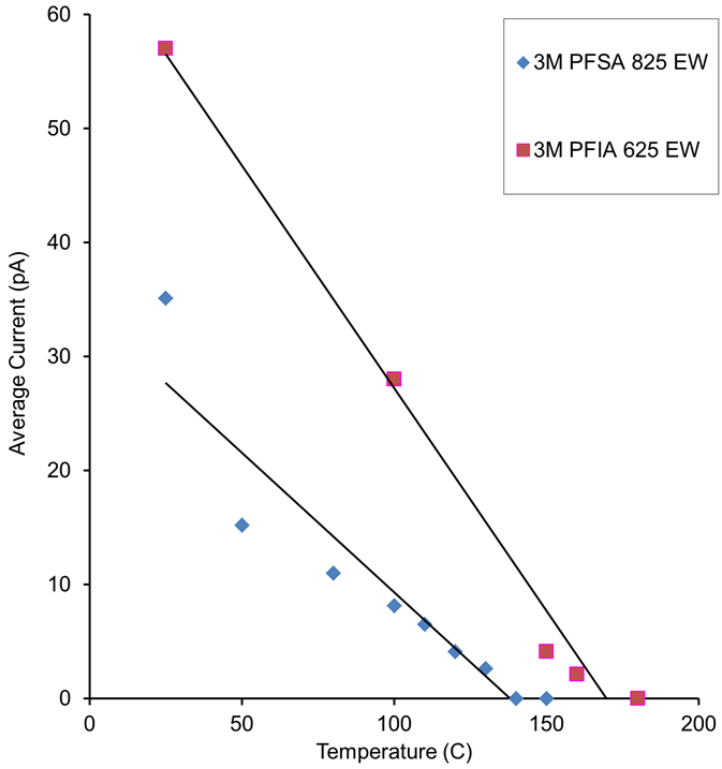

Figure 4.8: Average proton conductivity versus temperature under dry gas feeds for the PFIA and PFSA polymers. Flow rates were 50ml and 100ml per minute dry nitrogen at anode and cathode. Humidity was essentially constant (6% at 25C and 3% at 160C).

4.5 Conclusions

In summary, we have investigated two of 3M's perfluorinated ionomers which are designed specifically for PEM fuel cells operating under high temperature and low relative humidity. We show that both membranes have impressive water retention capability at low relative humidity, and that the PFIA is especially well suited for these conditions. At high RH we see a large amount of hydrophilic surface area in both, and the formation of a continuous hydrophilic phase in the PFIA which likely indicates unfavorable swelling. Using conductive imaging we measured the through plane conductivity at conditions closely resembling the operating conditions for these cells. We saw that the PFIA membrane shows higher currents and broader current distributions across all temperature and humidity. Comparison to bulk proton conductivity yields fairly good quantitative agreement at high relative humidity, but poorer agreement at low humidity due to a reduced electrochemical contact between the AFM tip and membrane surface. These measurements are useful because they allow us to visualize the effect of operating conditions on through membrane current under a steady DC bias which closely mimics fuel cell operation. The changing contact area of the tip also allows a quantification of surface contributions to overall resistance when compared to bulk conductivity values. Further optimization of this technique will allow for the continued evaluation of high temperature PEM materials.

References

(1) Osborn, S. J.; Hassan, M. K.; Divoux, G. M.; Rhoades, D. W.; Mauritz, K. A.; Moore, R. B. Glass Transition Temperature of Perfluorosulfonic Acid Ionomers. *Macromolecules* **2007**, *40*, 3886–3890.

(2) Zhang, S.; Dou, S.; Colby, R.; Runt, J. Glass Transition and Ionic Conduction in Plasticized and Doped Ionomers. *J. Non-Cryst. Solids* **2005**, *351*, 2825–2830.

(3) Ii, J. K. C.; Paddison, S. J.; Hamrock, S. J. The Effect of Hydrogen Bond Reorganization and Equivalent Weight on Proton Transfer in 3M Perfluorosulfonic Acid Ionomers. *Phys. Chem. Chem. Phys.* **2012**, *14*, 16349–16359.

(4) Maalouf, M.; Pyle, B.; Sun, C.-N.; Wu, D.; Paddison, S. J.; Schaberg, M.; Emery, M.; Lochhaas, K. H.; Hamrock, S. J.; Ghassemi, H.; et al. Proton Exchange Membranes for High Temperature Fuel Cells: Equivalent Weight and End Group Effects on Conductivity. *Proton Exchange Membrane Fuel Cells 9* **2009**, *25*, 1473–1481.

(5) Tant, M. R.; Darst, K.P.; Lee, K. D.; Martin, C. W. *Structure and Properties of Short-Side-Chain Perfluorosulfonate Ionomers. In Multiphase Polymers: Blends and Ionomers*; ACS Symposium Series 395.; American Chemical Society: Washington, DC, 1989.

(6) Adjemian, K. T.; Lee, S. J.; Srinivasan, S.; Benziger, J.; Bocarsly, A. B. Silicon Oxide Nafion Composite Membranes for Proton-Exchange Membrane Fuel Cell Operation at 80-140[degree]C. *J. Electrochem. Soc.* **2002**, *149*, A256–A261.

(7) Adjemian, K. T.; Dominey, R.; Krishnan, L.; Ota, H.; Majsztrik, P.; Zhang, T.; Mann, J.; Kirby, B.; Gatto, L.; Velo-Simpson, M.; et al. Function and Characterization of Metal Oxide−Nafion Composite Membranes for Elevated-Temperature H2/O2 PEM Fuel Cells. *Chemistry of Materials* **2006**, *18*, 2238–2248.

(8) Marani, D.; Trakanprapai, C.; Licoccia, S.; Traversa, E.; Miyayama, M. Influence of Titania Morphology on the Electrochemical Properties of Composite Polymer Electrolyte Membranes. *Mater. Res. Soc. Symp. Proc.* **2008**, *1126*, No pp. given, Paper #: 1126–S07 – 02–T06 – 02.

(9) Patil, Y.; Sambandam, S.; Ramani, V.; Mauritz, K. Model Studies of the Durability of a Titania-Modified Nafion Fuel Cell Membrane. *JOURNAL OF THE ELECTROCHEMICAL SOCIETY* **2009**, *156*, B1092–B1098.

(10) Patankar, K.; Dillard, D.; Case, S.; Ellis, M.; Lai, Y.-H.; Budinski, M.; Gittleman, C. Hygrothermal Characterization of the Viscoelastic Properties of Gore-Select® 57 Proton Exchange Membrane. *Mechanics of Time-Dependent Materials* **2008**, *12*, 221–236.

(11) Guo, Q. H.; Pintauro, P. N.; Tang, H.; O'Connor, S. Sulfonated and Crosslinked Polyphosphazene-Based Proton-Exchange Membranes. *J. Membr. Sci.* **1999**, *154*, 175–181.

(12) Titvinidze, G.; Wohlfarth, A.; Kreuer, K.-D.; Schuster, M.; Meyer, W. H. Reinforcement of Highly Proton Conducting Multi-Block Copolymers by Online Crosslinking. *Fuel Cells* **2014**, *14*, 325–331.

(13) Ye, Y.-S.; Yen, Y.-C.; Cheng, C.-C.; Chen, W. Y.; Tsai, L.-T.; Chang, F.-C. Sulfonated Poly(ether Ether Ketone) Membranes Crosslinked with Sulfonic Acid Containing Benzoxazine Monomer as Proton Exchange Membranes. *Polymer* **2009**, *50*, 3196–3203.

(14) Schaberg, M. S.; Abulu, J. E.; Haugen, G. M.; Emery, M. A.; O'Conner, S. J.; Xiong, P. N.; Hamrock, S. New Multi Acid Side-Chain Ionomers for Proton Exchange Membrane Fuel Cells. *ECS Trans.* **2010**, *33*, 627–633.

(15) Clark II, J. K.; Paddison, S. J. Proton Dissociation and Transfer in Proton Exchange Membrane Ionomers with Multiple and Distinct Pendant Acid Groups: An Ab Initio Study. *Electrochimica Acta* **2013**, *101*, 279–292.

(16) Economou, N. J.; O'Dea, J. R.; McConnaughy, T. B.; Buratto, S. K. Morphological Differences in Short Side Chain and Long Side Chain Perfluorosulfonic Acid Proton Exchange Membranes at Low and High Water Contents. *RSC Adv.* **2013**.

(17) O'Dea, J. R.; Economou, N. J.; Buratto, S. K. Surface Morphology of Nafion at Hydrated and Dehydrated Conditions. *Macromolecules* **2013**.

(18) Gierke, T. D.; Munn, G. E.; Wilson, F. C. The Morphology in Nafion Perfluorinated Membrane Products, as Determined by Wide- and Small-angle X-ray Studies. *Journal of Polymer Science: Polymer Physics Edition* **1981**, *19*, 1687–1704.

(19) Hsu, W. Y.; Gierke, T. D. Ion Transport and Clustering in Nafion Perfluorinated Membranes. *Journal of Membrane Science* **1983**, *13*, 307–326.

(20) Elliott, J. A.; Hanna, S.; Elliott, A. M. S.; Cooley, G. E. Interpretation of the Small-Angle X-Ray Scattering from Swollen and Oriented Perfluorinated Ionomer Membranes. *Macromolecules* **2011**, *33*, 4161–4171.

(21) P. J. James, J. A. Elliott, T. J. McMaster, J. M. Newton, A. M. S. Elliott, S. Hanna and M. J. Miles. Hydration of Nafion® Studied by AFM and X-Ray Scattering. *Journal of Materials Science* **2000**, *35*, 5111–5119.

(22) Hiesgen, R.; Aleksandrova, E.; Meichsner, G.; Wehl, I.; Roduner, E.; Friedrich, K. A. High-Resolution Imaging of Ion Conductivity of Nafion® Membranes with Electrochemical Atomic Force Microscopy. *Electrochimica Acta* **2009**, *55*, 423–429.

(23) Rubatat, L.; Gebel, G.; Diat, O. Fibrillar Structure of Nafion: Matching Fourier and Real Space Studies of Corresponding Films and Solutions. *Macromolecules* **2004**, *37*, 7772–7783.

(24) O'Dea, James. Probing Ion Conducting Domains and Localizing Catalysts in Proton Exchange Membrane Fuel Cells. Ph.D. Thesis, University of California Santa Barbara, 2010.

(25) McLean, R. S.; Doyle, M.; Sauer, B. B. High-Resolution Imaging of Ionic Domains and Crystal Morphology in Ionomers Using AFM Techniques. *Macromolecules* **2000**, *33*, 6541–6550.

(26) Liu, Y.; Horan, J. L.; Schlichting, G. J.; Caire, B. R.; Liberatore, M. W.; Hamrock, S. J.; Haugen, G. M.; Yandrasits, M. A.; Seifert, S.; Herring, A. M. A Small-Angle X-Ray Scattering Study of the Development of Morphology in Films Formed from the 3M Perfluorinated Sulfonic Acid Ionomer. *Macromolecules* **2012**, *45*, 7495–7503.

(27) Kreuer, K. D.; Schuster, M.; Obliers, B.; Diat, O.; Traub, U.; Fuchs, A.; Klock, U.; Paddison, S. J.; Maier, J. Short-Side-Chain Proton Conducting Perfluorosulfonic Acid Ionomers: Why They Perform Better in PEM Fuel Cells. *Journal of Power Sources* **2008**, *178*, 499–509.

(28) Epping Martin, K.; Kopasz, J. P. The U.S. DOEs High Temperature Membrane Effort. *Fuel Cells* **2009**, *9*, 356–362.

(29) Rozhok, S.; Sun, P.; Piner, R.; Lieberman, M.; Mirkin, C. A. AFM Study of Water Meniscus Formation between an AFM Tip and NaCl Substrate. *J. Phys. Chem. B* **2004**, *108*, 7814–7819.

(30) Weeks, B. L.; Vaughn, M. W.; DeYoreo, J. J. Direct Imaging of Meniscus Formation in Atomic Force Microscopy Using Environmental Scanning Electron Microscopy. *Langmuir* **2005**, *21*, 8096–8098.

5. Advances in Conductive-probe AFM Imaging of PEM's

5.1 AC-mode cp-AFM:

Our research group was one of the first to develop the conductive probe AFM technique for characterizing PEM's and it has been almost 10 years since its inception.[1] Whereas the previous chapters show the versatility of this technique in characterizing new membrane systems and developing a unique understanding of their structure and properties, this chapter details a series of technical developments aimed at expanding the capability of this imaging technique.

As can be seen from our previous experiments, tapping mode AFM and conductive probe AFM each provide valuable information about the membrane surface, and when combined, allow for the relationship between morphology and proton conductivity to be explored in great detail. In previous work, we have used phase-current correlation microscopy and taken scans in each mode and compared hydrophilic domains to proton conducting domains. This led us to the conclusion that

many hydrophilic domains do not conduct protons, as there is a lower occurrence of conductive domains.[1] There are several disadvantages to this technique, such as a resolution mismatch between the AFM tips and imaging conditions used. The low resolution of cp-AFM in contact mode precludes an accurate analysis of domain size and shape. Adsorbed water on the surface can also easily cause a loss of lateral resolution, as is seen in the conductive images in figure 3.6. Additionally, it is difficult to collect scans on the same area and directly compare them. An ideal technique would be to collect proton conductivity data while imaging in tapping mode, thus achieving high resolution conductivity images and allowing for a direct comparison between mechanical and electrical properties.

The challenge to this technique is that due to the rapid oscillation of the AFM tip, the period of time which it is actually in contact with the sample is very short. For a 75 KHz probe typically used, this equates to contact times on the order of microseconds. Takimoto et al. have published work where they appear to do just this, image in tapping mode while collecting conductivity data.[2,3] It is unclear, however, that this group was actually measuring proton conductivity, as it was conducted without fuel or oxidant being supplied, which we have found is necessary to achieve any current readings. This work was also done under a reverse-bias configuration where the tip acts as anode and surface acts as cathode, which introduces additional questions to how these images compare to our own. Hiesgen and coworkers, similarly have used peak force TUNA mode which is available on Bruker instruments, to simultaneously collect mechanical and electrochemical information. [4]

This technique, however is better suited for measuring adhesion force than tip-sample dissipation. The lateral resolution of the image is also affected by the large amount of contact required.

For our AC mode cp-AFM experiments, we used an identical setup to our contact mode measurements, with the membrane hot-pressed onto a commercial carbon cloth electrode and imaged inside of our humidity controlled fuel cell sample chamber.[5,6] We used a DPER18 platinum-iridium coated cantilever. These have the advantage of low electrical noise, and a small, 20 nm tip radius which afforded good lateral resolution. Because of the extremely low fundamental resonance of these cantilevers (~10 KHz) we conducted our tapping mode experiments using the second harmonic at ~80 KHz and found that this allowed for stable tapping mode imaging while still allowing for a current to be read. We noticed that these measurements were only possible with high relative humidity (>75%) inside of the sample chamber and hydrogen being supplied at the anode. While the second harmonic does not follow the simple dissipation-phase angle relationship outlined in the experimental section, we found that in practice it still gave negative contrast to hydrophilic domains when in attractive mode, implying that the direction of phase contrast is the same despite having a possibly different dependence on power dissipation.

Figure 5.1 shows a series of two conductive AFM scans of Nafion 212, the top taken in contact mode, and the bottom taken in tapping mode using the same cantilever and imaging the same sample area. The area in the circle is the same in

each image to provide a useful feature for reference. In tapping mode, we achieve much higher resolution in topography and clearly alter the surface much less than when imaging in contact mode as is apparent by the decreased smearing of fibrils in the scan direction. At the same time, our contact mode image gives much higher currents (50 pA vs 3 pA) due to the longer duration of electrical contact during imaging. Figure 5.2 shows histograms of current values from each conductive image in Figure 5.1.

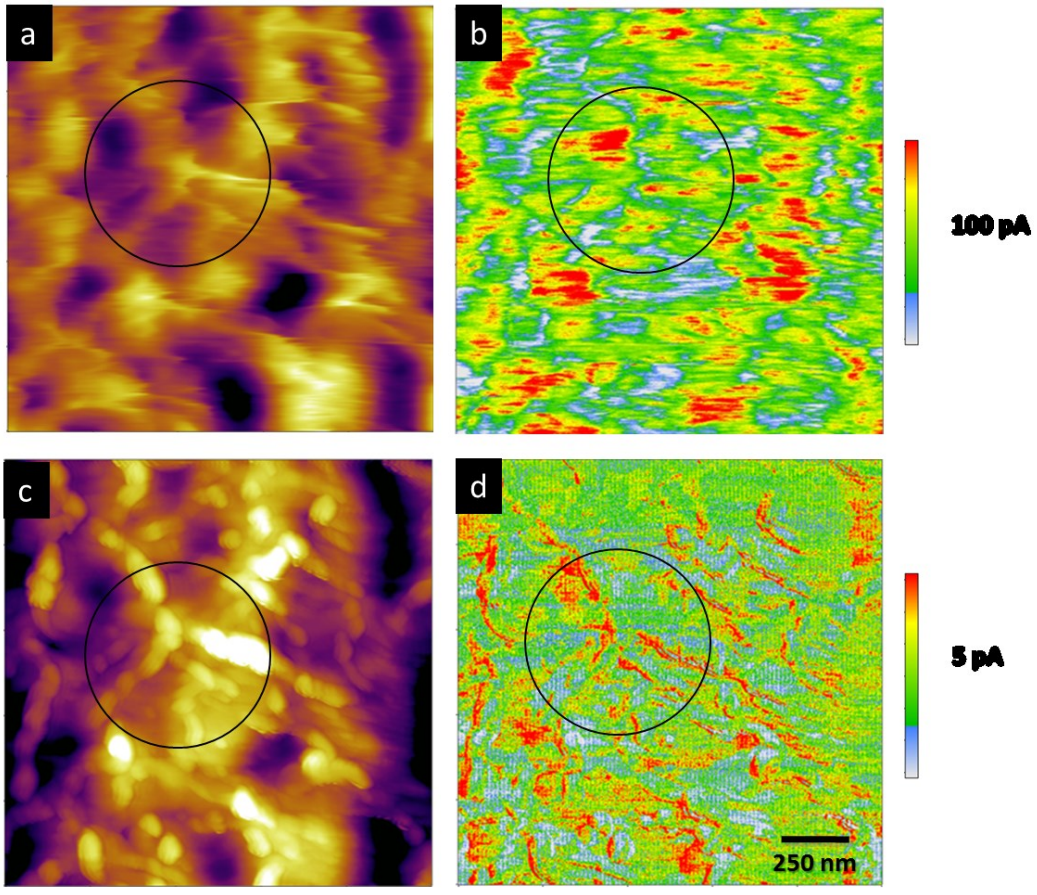

Figure 5.1: Contact mode (a,b) and AC-mode (c,d) conductive AFM images. Topographic images are shown in (a) and (c) current is shown in (b) and (d). Images were collected at room temperature with a +1 V sample bias.

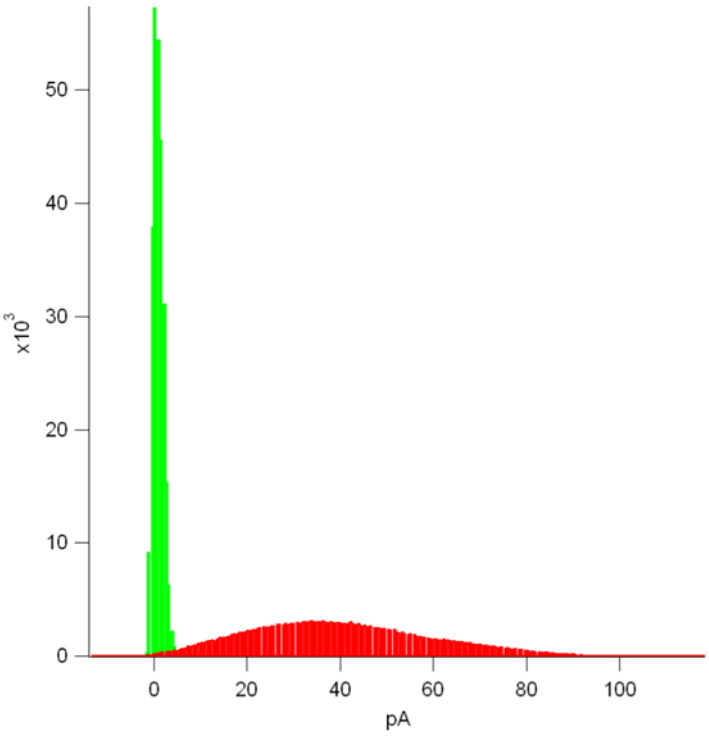

Figure 5.2: Histograms of current values from Figure 5.1 images, green is AC-mode and red is contact mode.

In the conductivity image we see several insulating fiber features covering the sample, but outside of those, the entire surface appears conductive due to water at the surface delocalizing our measurements. In the tapping mode image we are able to discern distinct hydrophilic domains. In this image, we noticed that the sides of fiber features provided a conductive area, possibly due to retention of water in these locations. It may also be that preferential tip contact due to the water in these locations caused an increased current reading. The challenge to conducting and interpreting images in this imaging mode, is insuring that there are no artifacts in the current image caused by differences in tip-sample contact over the sample. For these

reasons, after scans were taken in attractive mode, repulsive mode scans with a much lower setpoint (A/A° = 0.5) were employed and compared to the attractive mode image. It was also common to scan the area in contact mode after as well in order to investigate the tip-sample contact dependence, as well as to obtain more quantitatively accurate current readings.

With these questions about the nature of tip-sample contact unanswered, it is impossible to judge whether these AFM scans are providing useful information or merely reflecting the topography through changes in contact area. We conducted a series of AC-mode force curves in order to more closely examine the nature of these forces. For these experiments, the same cantilever is used at the same drive frequency as before, a conductive region is chosen and the tip is gradually brought into contact while the current, amplitude and phase are monitored. We can see clearly that there are two current response regimes in the force curve, the first occurs at relatively high amplitudes (>80% of free amplitude), and corresponds to a ~5pA current, which is typical for AC mode imaging. At extremely low amplitudes, essentially contact mode, we see a much larger response. This appears to occur in a step-like fashion, indicating that the actual value of the amplitude setpoint has minimal effect on the observed current. Furthermore, looking at the phase image, we can see that there is little difference in current between operating in the attractive (>90) and repulsive (<90) regimes. Several force curves were collected at different points on the surface and showed very similar behavior. This tells us that the current response is uniform under static (non-scanning) conditions, but many of the artifacts

we see might be due to scan direction and other dynamic effects. To further calibrate our technique, we employed a series of conductive model samples in order to discern the relationship between current and topography during scanning. The most useful was fluorine doped tin oxide (FTO) as its rough surface topography and relatively uniform surface conductivity allowed us to observe the relationship between contact forces and observed current directly.

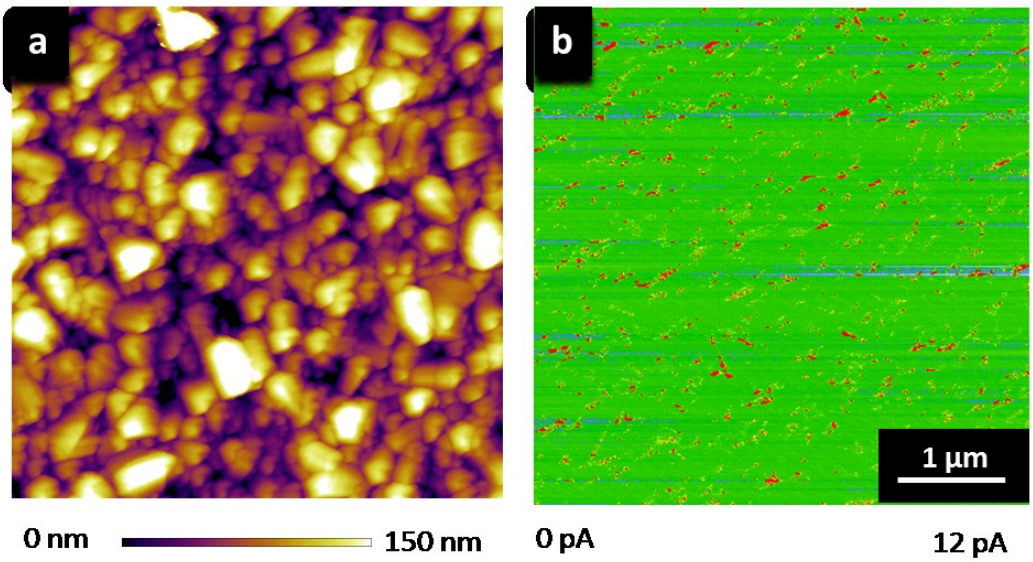

Figure 5.3: Topography and current images of an FTO sample collected in AC mode with a +1V sample bias.

In this sample, we saw that unlike in contact mode where uniform conductivity is observed, most of the sample appears insulating with scattered bright spots. Average currents were also much lower than is observed in contact mode, which is unsurprising given our previous data on Nafion. Overlaying the current image on the height image and on the phase image gives a clear picture of what factors influence the observed current. In Figure 5.5a, one can see that current is preferentially read on

one side of the FTO crystallites, which was found to vary with the AFM scan direction. This is similar to the influence of topography on phase that we observe in our phase imaging of Nafion.[7]

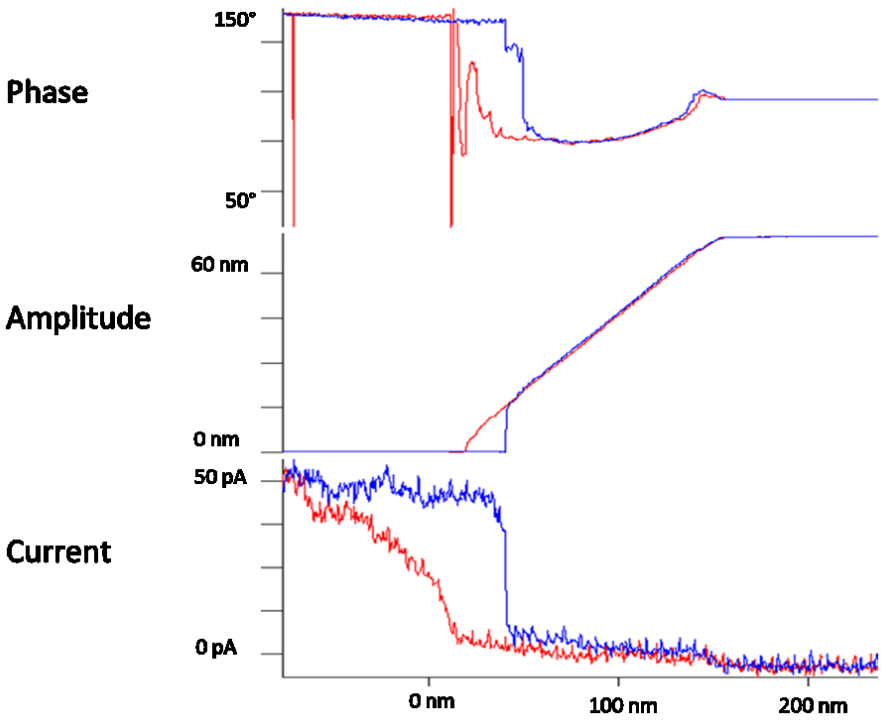

Figure 5.4: AC mode force curve of a Nafion 212 Half-MEA under bias and with humidified gas feeds. Phase, amplitude and current were simultaneously collected. The blue trace represents the approach of the tip towards the sample while red represents the retraction.

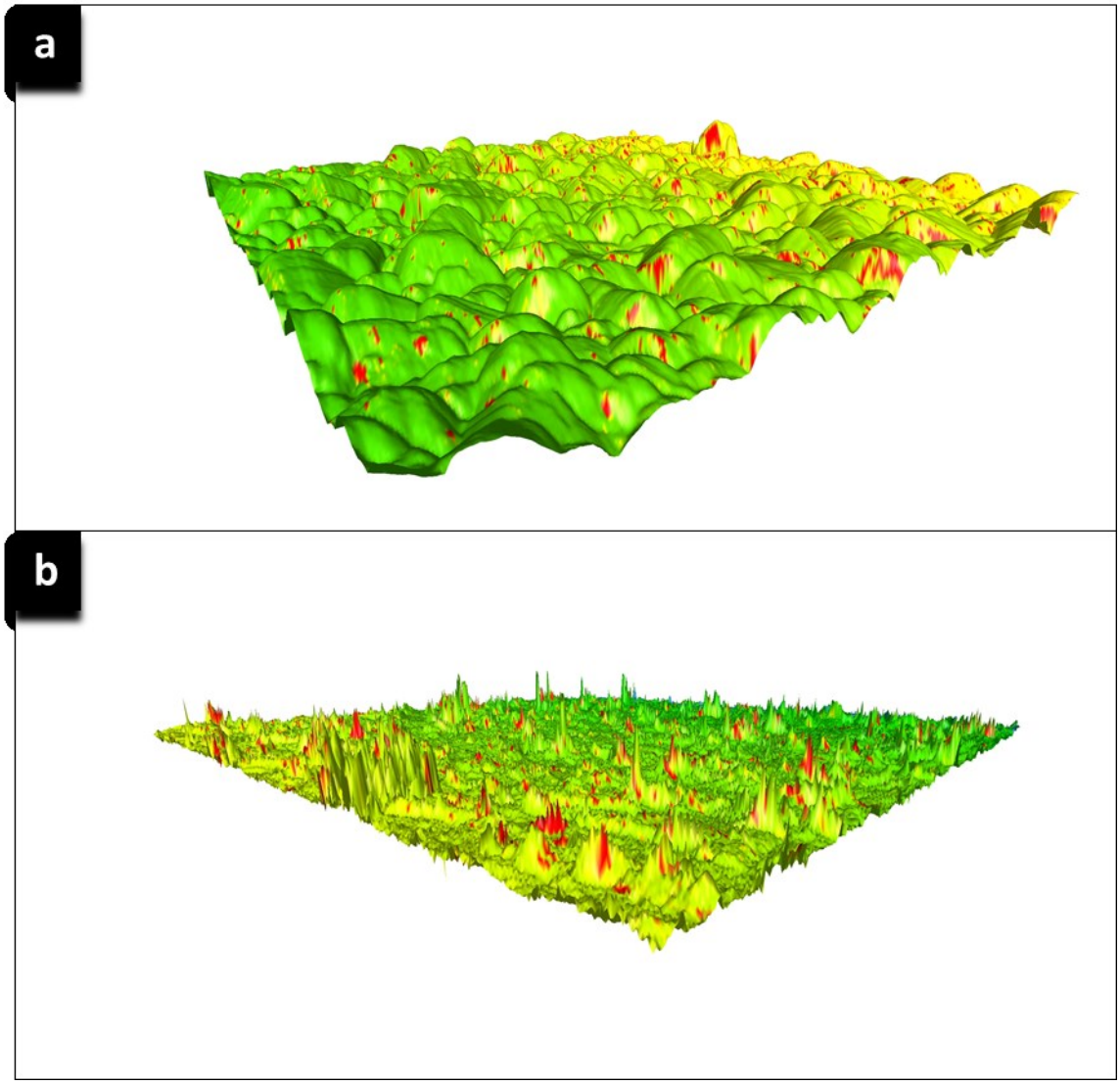

Figure 5.5: Current overlayed on topography (a) and Current overlayed on phase (b) for the FTO sample in Figure 5.4

In the overlay of current and phase, we see that this is indeed the case, and that both current and phase are almost perfectly correlated with tall areas (high phase angle) showing up as red (high current). This phase image was collected in repulsive mode, where positive values (peaks) correspond to areas with higher tip-sample power dissipation. In this case there should be almost no variation in the material

properties of the sample, so any phase is an artifact of differences in tip-sample contact.

These experiments reveal that under certain conditions there is a strong coupling between tip-sample contact and observed current when measuring electrical conductivity on a rigid sample, it is not clear to what degree this carries over to measuring proton conductivity on a much softer sample with water at the surface. FTO is also much rougher than Nafion (35 nm rms roughness vs 5 nm), so any topographic contributions are exaggerated on this sample. Even so, after all experiments on Nafion we carefully checked for any correlation between current, phase, and topography in order to assure that we are isolating the properties of interest.

Subsequent optimization of imaging parameters allowed for a more routine collection of AC mode cp-AFM images and reduced contribution to current from topographic factors. Figure 5.6 shows two series of images of Nafion 212 at larger (5 μm) and smaller (250 nm) length scales. At large length scales we can see that while fiber features are nearly invisible in topography, they can be resolved in the phase image and show dissipative character. This image is especially interesting as these fibers can be seen to go beneath the surface and lose phase contrast at certain locations. However, even when they are sub surface, they are still visible in the conductivity image, indicating that they can still impede proton transport even if they

are not directly at the surface. It is interesting to note, however that the correlation between current and phase is far from perfect.

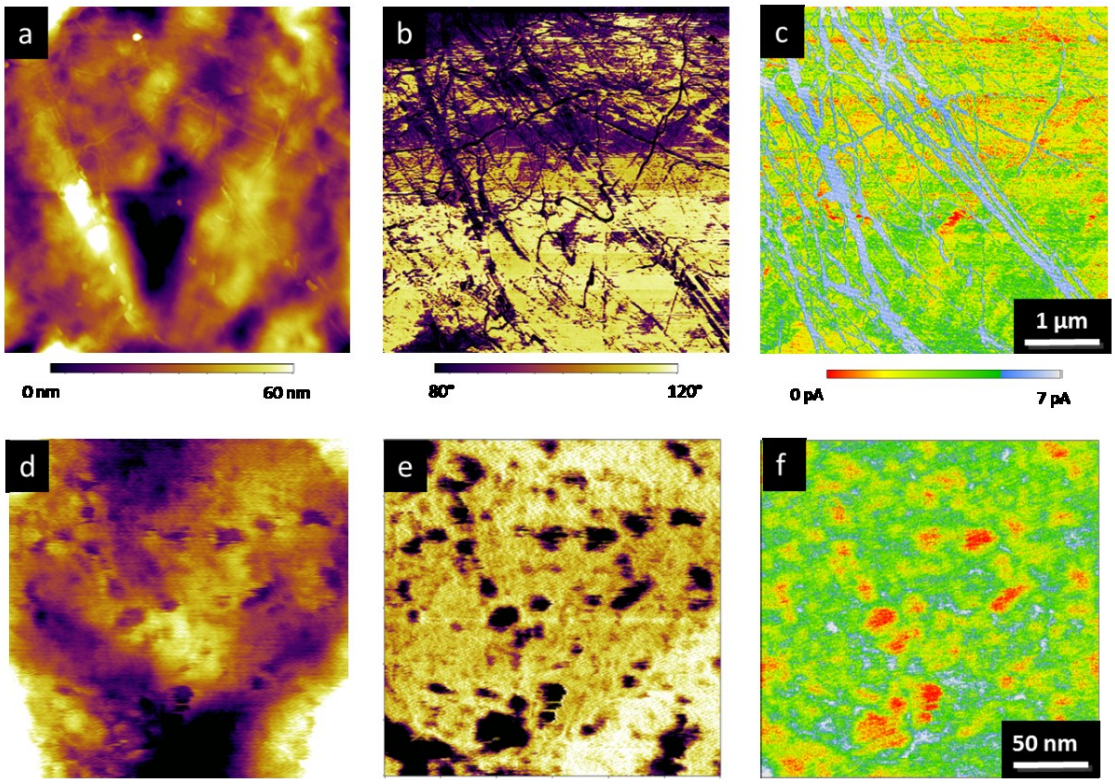

Figure 5.6: Large (5µm) (a,c) and small (250 nm)(d-f) length scale AC-mode cp-AFM images of a Nafion 212 half MEA. Topography (a,c) Phase (b,d) and Current (c,f). Images were collected at +1V sample bias at room temperature with 50mL humidified hydrogen and 100mL humidified air supplied at the anode and tip respectively.

At smaller length scales, we see that we can isolate individual proton conducting domains in the conductivity image (f). For the most part, conductive regions coincide with hydrophilic regions in the phase image, however there are several exceptions. Looking closely, one notices that several proton conducting spots occur at places on the membrane which appear hydrophobic. This indicates that despite being

apparently isolated in the phase image, there is actually a thin layer of surface water present on the membrane which connects domains. This image was collected at 75% RH, and it is likely that there exists a point at which this layer is not present. In our experiments, however, we were not able to collect AC mode conductive images at humidities below 70%. This could be in part to the humidity dependence of Nafion's conductivity dropping below the detection threshold of our cp-AFM hardware, more sensitive current sensing hardware would be ideal for future measurements in this regime.

We also notice the opposite phenomenon, hydrophilic domains which appear insulating in the proton conductivity image. This is likely caused by these domains being dead-ends and not connecting with the rest of the proton conducting network. This sheds some doubt on the previously accepted wisdom that proton conducting regions and hydrophilic regions are directly correlated. This is consistent with the previous work in our group using phase-current correlation, but it is interesting to see directly. Another interesting discovery is that the largest hydrophilic domains are the ones which provide the largest currents. This is consistent with theory as it is expected that as water is less tightly bound to sulfonic acid sidechains, it can behave more like bulk water and exhibit higher proton conductivity. It also tells us that in order to create a membrane with higher proton conductivity it is ideal to make domains as large as possible.

With this new imaging capability we can directly correlate phase and current and gain an in-depth understanding of the relationship between morphology and proton conductivity. It may be possible to further improve this technique by finding ways to increase currents, either through sample design or by time-resolving the current signal such that the current is read only when the tip is in contact with the surface.

5.2 Reversed electrode configuration

In our next series of experiments, we investigated the possibility of reversing the electrode configuration of our samples; using the tip as an anode while using the bottom electrode as a cathode. Since the kinetics at the cathode are more sluggish, it should be possible to improve current output by having a more ideal catalyst (a commercial electrode) on this side. In this series of images we operated in contact mode in order to achieve more quantitatively accurate current readings and to compare the reversed and normal configurations.

One issue that occurred with this technique was a high and sometimes drifting background current both with and without bias. It appears that flowing hydrogen over the tip allows the hydrogen oxidation to proceed even without bias, and thus causes a substantial and inconsistent baseline current. Nonetheless, by using higher flow rates of hydrogen and allowing this current to stabilize, it was possible to collect good quality conductive AFM images.

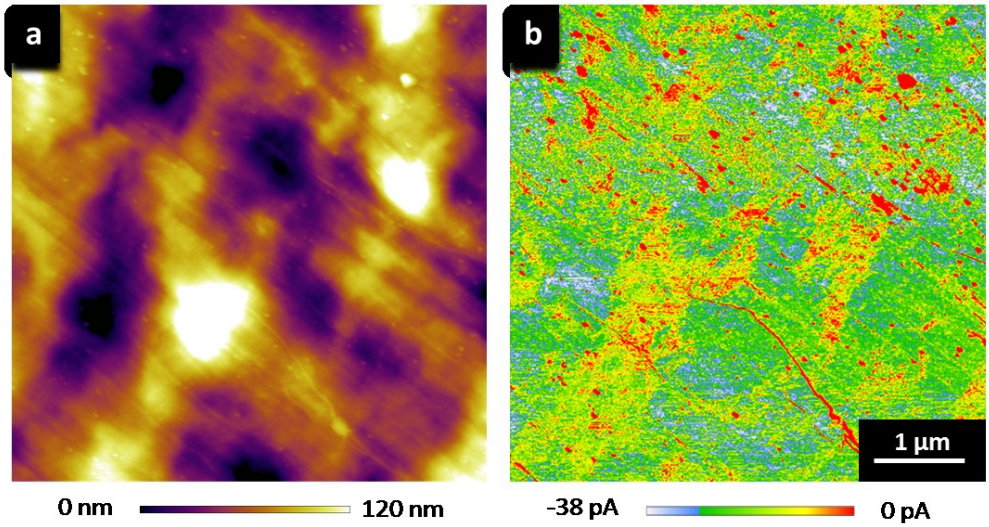

Figure 5.7: Topographic (a) and conductive (b) images of a Nafion 212 half MEA using the reversed electrode configuration. Humidified air was supplied below the sample at 50 mL per minute and humidified hydrogen was flowed over the sample at 200 mL per minute. This image was collected at -1V sample bias at room temperature.

In this case we observed a ~100 pA background current which was present at all bias conditions and only when hydrogen was present in the sample chamber. Fiber features now appear red, as they are the most insulating section, while white and blue areas are highly conducting. This image is essentially the inverse of what we see in the normal configuration. Contrary to our expectations, we did not achieve higher currents under the reverse configuration. This tells us that there is not any significant kinetic limitation from the ORR occurring at the tip. For this reason, we typically do not employ the reverse configuration, as it offers little additional information and more difficulty in collecting stable images. The ability to investigate both electrodes independently does introduce the possibility of investigating CO poisoning or other phenomenon by selectively poisoning one catalyst layer or the other. The use of

different tip materials could also allow for the investigation of new catalysts in a spatially resolved manner.

5.3 Using methanol as a fuel

Although there is much interest in developing PEM fuel cells which utilize liquid fuels such as direct methanol fuel cells (DMFC's)[8] and designing new membranes for these applications[9–11], conductive-probe AFM using methanol as a fuel has yet to be demonstrated. A large reason for this is that the sample design for these experiments is not trivial. The membrane must be in contact with a liquid fuel which causes swelling of the membrane,[12] while the AFM tip must be kept relatively dry in order to selectively read current. Despite these inherent challenges, this type of imaging could be tremendously useful for evaluating PEM stability and performance in this unique environment. Bulk proton conductivity in DMFC's is a frequently sought after metric for gauging performance,[9,13,14] and methanol permeability of the membrane provides another key parameter to consider in membrane design.[15–18] Both spatially resolved studies on proton conductivity, and on methanol crossover in these membranes would be of great use for understanding membrane operation and improving design.

For these measurements, we used the same fluid cell, sample, and tip as used before. Instead of flowing hydrogen at the anode, we fed a 2M solution of methanol in water (a typical DMFC fuel stream) using a peristaltic pump. Very low flow rates were used (10's of mL/minute) in order to cause minimal stress to the half MEA,

even so, the sample usually bulged significantly in the center. Tip engaging and stable topographic imaging was extremely difficult for these samples and wetting of the sample and its delamination from the steel puck used to attach is to the cell was also a constant issue.

After many trials, we were able to achieve stable cp-AFM images which are shown in Figure 5.8. Interestingly, the currents we observe are more than an order of magnitude higher than we see using hydrogen gas. This is surprising as DMFC's typically have a much lower current density. The probable cause is that the membrane becomes highly hydrated due to contact with water which causes the membrane proton conductivity to greatly increase. We also noticed that conductivity values would steadily rise over the course of measurements, another strong indicator that this is the case. MEA's were often very rough when imaging under these conditions, likely due in part to high degree of swelling.

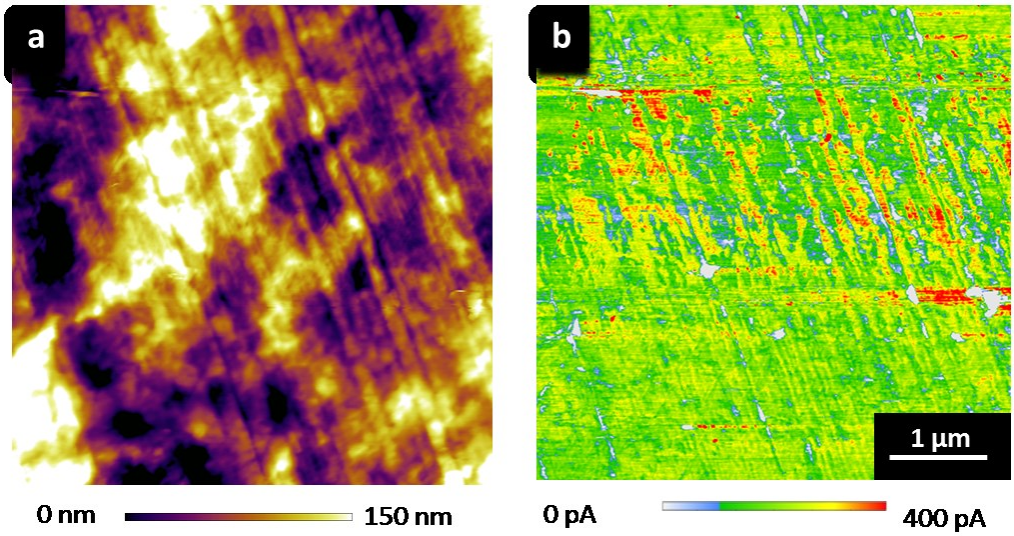

Figure 5.8: Topographic (a) and conductive (b) images of a Nafion 212 half MEA using methanol as fuel. A 2M aqueous methanol solution was fed at the anode under the sample using a peristaltic pump. Humidified air was provided at the tip and the sample was scanned at +1V sample bias.

These experiments are still in their preliminary stages but represent an excellent way to evaluate membranes for DMFC's and other liquid fuel systems. Sample design is a crucial issue for achieving reliable images, and improvements in the dimensional stability of the sample should make imaging much easier. Future experiments which can selectively measure methanol permeating through the membrane would be of great use towards understanding the spatial variation in this process.

5.4 Imaging proton conductivity inside the catalyst layer

In addition to the PEM itself, understanding proton transport inside of the catalyst layer of the fuel cell is an important goal for improving fuel cell performance. Inside of the catalyst layer, proton conducting polymer, electron conducting carbon, and reactant gases exist together in a "three-phase reaction zone". It is understood that a certain ideal mixture of these must exist in order to facilitate fuel cell operation. However, the hydration state of Nafion inside the catalyst layer is greatly reduced compared to inside the membrane (λ = 2 -3), due to physical confinement, and coordination with carbon and platinum particles. This likely adds resistance to the fuel cell and lowers performance. Many studies have been geared towards determining bulk proton conductivity values of the ionomer phase inside of the catalyst layer of the electrode.[19–22] For this reason, we would like to be able to conduct a similar type of imaging in order to characterize the morphology and proton conductivity of Nafion inside of the catalyst layer and examine any spatial variation that might occur. For these experiments we constructed what we refer to as a ¾ MEA in contrast to the ½ MEA's used for membrane conductivity images. In these samples we hot pressed a commercial electrode on one side of the membrane alongside a thin film decal electrode on the other side.

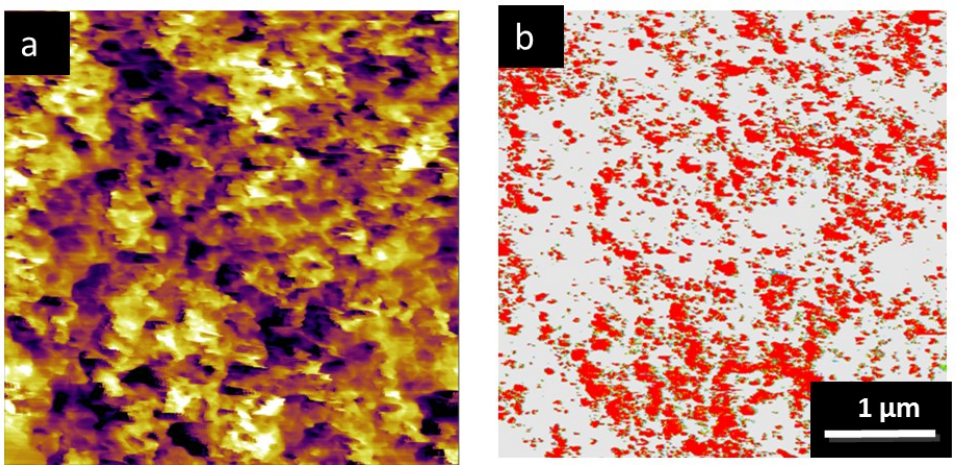

Figure 5.9: Topographic (a) and conductive (b) images of a Nafion 212 3/4 MEA without fuel applied and under zero bias.

These decal electrodes were anywhere from 1 to 10 microns thick and consisted of a 3:2 carbon to Nafion ratio (by weight). Large scale topographic and conductivity images are shown below in Figure 5.9. We found that a major limitation of this technique is that conductivity readings are delocalized throughout the carbon phase of the top electrode. This causes readings which saturate the detector whenever scanning over the carbon particles, and can be seen by the bimodal distribution of currents found in Figure 5.9. In this case, the image was taken with no fuel, no humidification, and no bias, conditions which normally would lead to no current at all. Even though Nafion is a very good electronic insulator, when the tip is in contact with the carbon electrode the large effective surface area causes large currents to pass through the membrane even under nominally zero bias. This can best be seen in the image in Figure 5.10 where a cross section of Nafion is imaged by conductive AFM without fuel or bias. We see that the bottom electrode and top electrode both show

extremely high conductivity whereas the membrane between them shows very low conductivity (essentially zero).

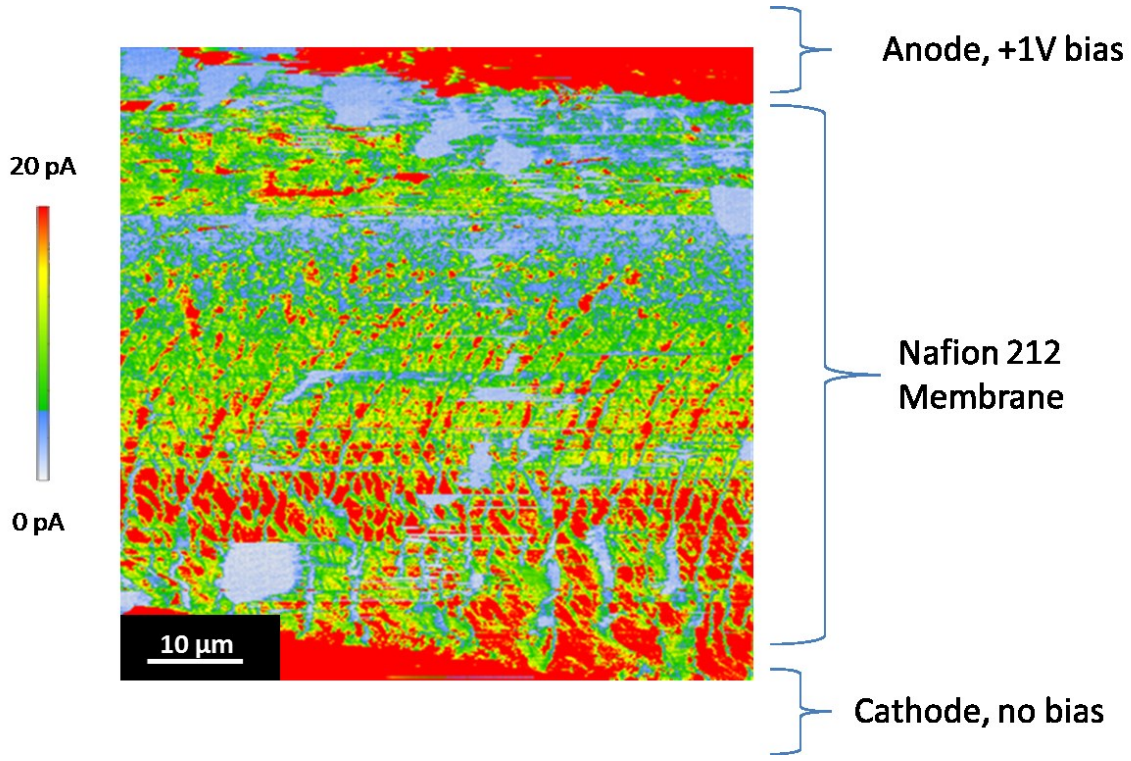

Figure 5.10: Cross sectional conductive image of a ¾ MEA showing delocalized current measurements. The top electrode in this image is biased at +1 V with no connection to the bottom electrode. Both electrodes showed enough current to saturate the current detecting hardware (20 nA).

For this reason, any attempt to measure proton transport inside of a catalyst layer will suffer from delocalization of current measurements. Despite this, we can still differentiate between the conductive carbon phase and the insulating Nafion phase, so this technique is still useful for examining electrode morphology. It may also be useful to examine the electrical conductivity of the carbon phase, but this type of

study would require a larger current range than the ORCA holder we use can provide. Hiesgen et al. conducted a similar series of experiments and showed conductive images of carbon electrodes where the electrical conductivity was probed directly in this manner.[23]

It was, however possible to obtain images where we could simultaneously view the ionic conductivity of the membrane and the electronic conductivity of the carbon electrode. For these experiments, we created an extremely low mass carbon/Nafion decal such that the carbon did not completely cover the surface. This was done by using a carbon ink that was diluted 100 times, spin casting a film and hot-pressing it onto the top surface of the membrane. In this sample we can see large strings of agglomerated carbon particles which are adhered to the membrane. These strings are easily visible in the conductive image, but difficult to see in the topography as they have been submerged in the membrane during hot pressing. Aggregates several microns long were visible, as well as smaller aggregates and single carbon black particles with sizes of approximately 100 nm. Phase imaging (not shown) also did not allow for reliable differentiation of these carbon aggregates, likely due to a Nafion layer on the outside.

This image shows that there is a clear relationship between the size of carbon aggregates and the current being read. This indicates that as the conductive area in contact with the tip gets larger, the current that can be read through the membrane increases. This would be equivalent to using a tip with a much larger surface area.

Related to this is an extremely consistent current reading across of each of these aggregates. We also notice a high current outline on the leading edge of aggregates which we think is due to a capacitive charging of carbon particles during each scan. This was observed in scans in each direction and never exceeded a few pixels in width. This is not a phenomenon which would occur in an operating fuel cell, as it is the movement of the tip which causes this charging to occur.

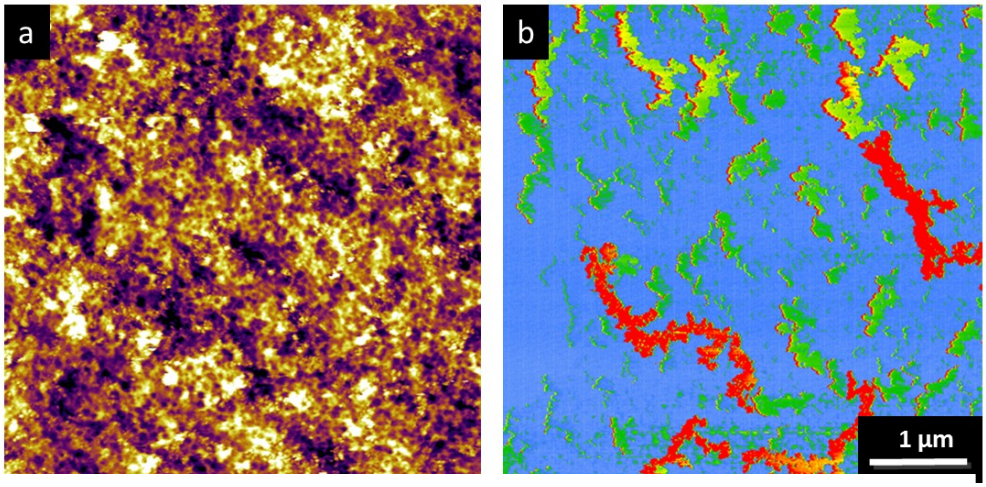

Figure 5.11: Topographic and conductive images of a ¾ MEA with an extremely thin layer of carbon applied to the top. The strings (red) in the conductivity image are carbon aggregates and the areas in between are exposed Nafion membrane. This was collected using standard fuel flow rates and a +1 V bias. Topographic scale is 110 nm, current scale is 30 pA.

In between aggregates, we can see that the Nafion surface undergoes a similar degree of proton conductivity (average current = 10 pA). This is much lower than over the carbon particles, as the effective tip area in these locations is much lower due to a lack of delocalization.

5.5 Diagnosing Catalyst Utilization Using cp-AFM

We discovered that cp-AFM is an effective tool for the evaluation of new catalyst preparation methods. Our lab is involved in work to reduce the platinum loading of electrodes without sacrificing fuel cell performance. We accomplish this through the electrodeposition of platinum nanoparticles using a PEM as a template as is described in the work of O'Dea,[6] Ranasinge[24], and Burk[25]. This method is able to greatly reduce loadings, but the performance of the cell is always lower, despite theoretically having platinum at the terminus of every membrane-spanning hydrophilic channel. To analyze the effectiveness of this type of preparation, we made half MEA's using both a commercial electrode, and an electrode that has had platinum deposited electrochemically through the membrane, onto the electrode surface. We then took several large area- cp-AFM scans of each half MEA. What we saw was that on many of the through-membrane deposited electrodes, there were large, micron size areas of non-conductive membrane, implying that the platinum precursor did not deposit evenly through the membrane onto the electrode. These areas were often several microns in size, much larger than any of the non-conductive features typically seen in our conductive AFM experiments. After analyzing 10 images on each MEA we saw that the average active area of the TMD cell was approximately 2/3 that of the commercial cell. Average currents of the active regions were found to be similar in each sample, and there was no difference in observed membrane morphology. This is a strong indicator that the anode catalyst layer is the cause of this inhomogeneous through-plane proton current This led us to believe that

perhaps the electrode surface has a non-uniform surface potential such that platinum precursor does not deposit evenly and leads to these inactive areas. These electrodes were fabricated by immersing the ½ MEA in a platinum precursor solution and electrodepositing through the membrane We employed electrostatic force microscopy (EFM) to investigate the surface charge of a bare electrode under bias.

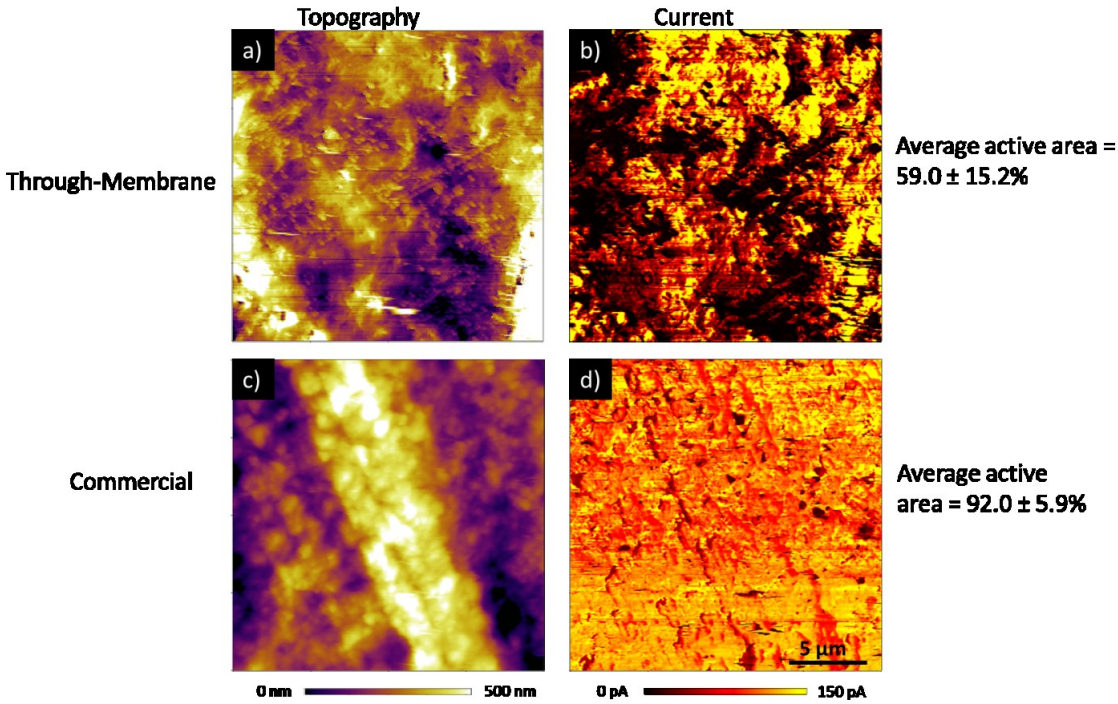

Figure 5.12: Representative topographic (a,c) and current images (b,d) from half MEA's fabricated using through-membrane electrodeposited electrodes (top) and commercial electrodes (bottom). Average active area is an average of ten 20 µm by 20 µm images.

Our goal is to understand the charge at the surface of the electrode when under bias, under conditions similar to the electrochemical deposition. This would provide a rough indicator of areas of the surface where platinum is able to deposit effectively.

This technique consists of a dual-pass scan where the topography is first scanned in tapping mode, then a second pass retraces the topography with a set lift height to give a fixed tip-sample separation. A bias is applied to the sample which causes shifts in the frequency of the cantilever oscillation due to local differences in the electric field above the sample.

On our blank carbon electrode, we see large, micron sized regions with a lower surface voltage (blue) scattered across the electrode surface. This implies that these regions have effectively lower surface potential and would be less preferentially electrodeposited on under bias. On these electrodes, both Nafion and Teflon are used as binding agents, so these may represent locations where the concentration of binder is prohibitively high. These areas never show zero voltage, but this could be because EFM probes the electric field from the entire sample. If we had a thin insulating layer over a thick conductive layer, as we suspect, than this is the type of reading that might be observed. For this reason, the EFM image likely over-estimates the voltage at the very surface of the electrode in these locations.

We also see a significant contribution to the surface voltage from topography, as is common in EFM experiments, especially with rough samples such as these. We experimented with a wide range of drive amplitudes, lift heights, and applied biases and found that while a large amplitude and lift height reduced this contribution, it could never be fully be avoided.

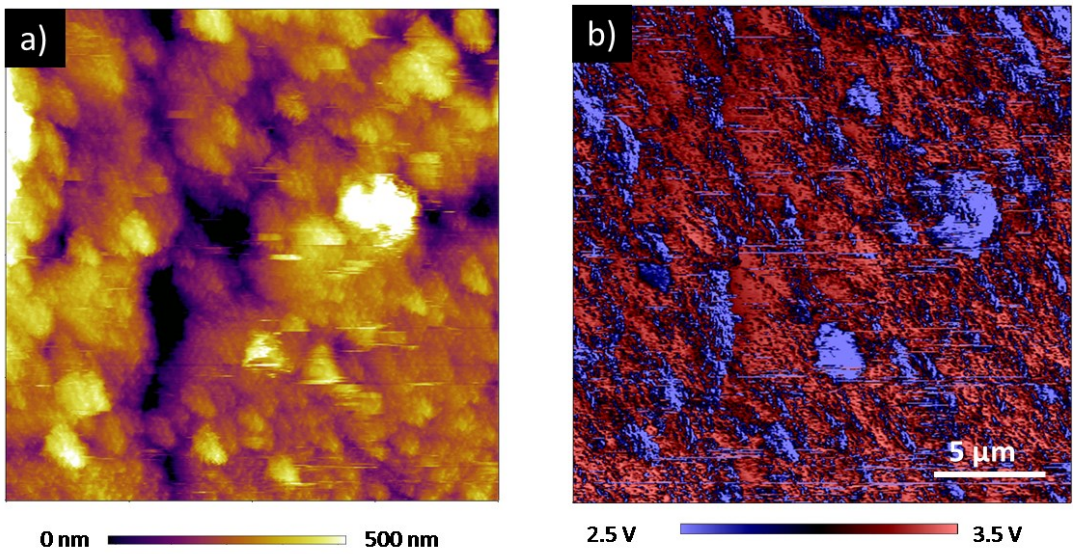

Figure 5.13: Topography (a) and electrostatic force images (b) of a blank ELAT 1400 LT electrode. Collected at +3V bias.

It is possible, however, that the roughness of these electrodes alone is enough to cause inhomogeneous platinum distribution. In solution, a platinum precursor will see a field similar to what we see as it approaches the surface. This indicates that the large surface roughness alone may be sufficient to cause uneven platinum deposition. In solution, other phenomenon such as diffusion limitations and double layer charging will also play a role in affecting platinum deposition.[26,27]

In order to attempt to minimize topographic contributions to our surface electrical characterization, we employed scanning kelvin probe microscopy (SKPM) to look at the same blank electrode. This technique is commonly employed for examining conductive carbon structures[28–31], and has the advantage of a reduced contribution from topography in most cases. While similar to EFM, this technique

instead does not oscillate the cantilever on the nap scan, and instead applies an AC voltage directly to the tip at the resonance frequency of the cantilever. The electrostatic attraction then induces an oscillation in the cantilever which is then measured, and with the appropriate reference, can be used to calculate the work function of the surface directly.

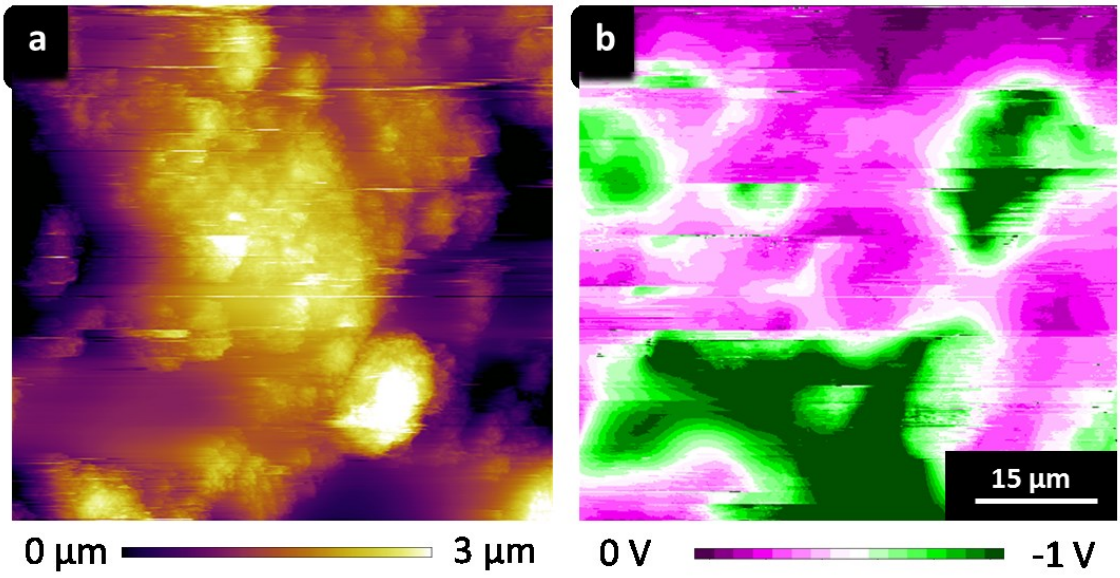

Figure 5.14: Topography (a) and surface potential (b) of a blank ELAT 1400 LT electrode. Collected at 5V AC tip bias.

In these images, we can clearly see areas of negative surface potential, shown in green. These correspond to areas which would require a higher overpotential to effectively deposit on. Electrodeposition is typically carried out with a ~0.5 overpotential (-1.5V vs SCE), so it may be that to achieve a truly optimal electrode surface, higher potentials are required. It should be noted that these potentials have not been calibrated by using a reference of known work function, but at least qualitatively they tell us that there is a large scale variation in surface potential.

Future work in this area will aim to quantify these potential differences and optimize our electrodeposition procedure to best overcome these variations and evenly deposit platinum across the surface.

5.6 Conclusions

In this chapter we outlined several experiments aimed at both refining and expanding conductive imaging to a wider range of samples. We demonstrate that conductive probe AFM can be utilized in tapping mode under appropriate conditions. This allows for direct correlation between the chemical properties of the surface (hydrophilicity) and its electrochemical properties (proton conductivity). We have also shown that reversing the electrode configuration is possible, but that the amount of additional information it provides is limited.

We have demonstrated the first conductive imaging of a PEM using methanol as a fuel, and hope that with further development it can become a technique which can be routinely employed to evaluate PEM performance under DMFC operating conditions. Tailoring of this technique to investigate spatially resolved methanol permeability raises another interesting avenue for evaluating DMFC membrane materials.

While our attempts to obtain spatially resolved proton conductivity inside of the catalyst layer were not entirely successful, we nonetheless have developed a useful technique for evaluating electrode morphology. Further experiments to this end may

be able to use time resolved electrical AFM techniques such as electrical impedance AFM[32–35] in order to separate electronic and ionic conductivity, as they exhibit different frequency dependencies.[36] The use of cp-AFM to investigate the efficiency of electrodeposited catalysts provides an exciting avenue for refining these techniques and developing ultra-low Pt loading electrodes without sacrificing performance. In conjunction with surface potential mapping, we can obtain a much better spatial understanding of the platinum deposition process and use this to further optimize deposition parameters in order to further decrease platinum loading and maintain high cell performance.

References

(1) Bussian, D. A.; O'Dea, J. R.; Metiu, H.; Buratto, S. K. Nanoscale Current Imaging of the Conducting Channels in Proton Exchange Membrane Fuel Cells. *Nano Letters* **2007**, *7*, 227–232.

(2) Takimoto, N.; Wu, L.; Ohira, A.; Takeoka, Y.; Rikukawa, M. Hydration Behavior of Perfluorinated and Hydrocarbon-Type Proton Exchange Membranes: Relationship between Morphology and Proton Conduction. *Polymer* **2009**, *50*, 534–540.

(3) Takimoto, N.; Takamuku, S.; Abe, M.; Ohira, A.; Lee, H.-S.; McGrath, J. E. Conductive Area Ratio of Multiblock Copolymer Electrolyte Membranes Evaluated by E-AFM and Its Impact on Fuel Cell Performance. *Journal of Power Sources* **2009**, *194*, 662–667.

(4) Hiesgen, R.; Helmly, S.; Morawietz, T.; Yuan, X.-Z.; Wang, H.; Friedrich, K. A. Atomic Force Microscopy Studies of Conductive Nanostructures in Solid Polymer Electrolytes. *Electrochim. Acta* **2013**, *110*, 292–305.

(5) Economou, N. J.; O'Dea, J. R.; McConnaughy, T. B.; Buratto, S. K. Morphological Differences in Short Side Chain and Long Side Chain Perfluorosulfonic Acid Proton Exchange Membranes at Low and High Water Contents. *RSC Adv.* **2013**.

(6) O'Dea, James. Probing Ion Conducting Domains and Localizing Catalysts in Proton Exchange Membrane Fuel Cells. Ph.D. Thesis, University of California Santa Barbara, 2010.

(7) O'Dea, J. R.; Buratto, S. K. Phase Imaging of Proton Exchange Membranes under Attractive and Repulsive Tip−Sample Interaction Forces. *The Journal of Physical Chemistry B* **2011**, *115*, 1014–1020.

(8) Kreuer, K. D. On the Development of Proton Conducting Polymer Membranes for Hydrogen and Methanol Fuel Cells. *Journal of Membrane Science* **2001**, *185*, 29–39.

(9) Silva, V. S.; Mendes, A.; Madeira, L. M.; Nunes, S. P. Proton Exchange Membranes for Direct Methanol Fuel Cells: Properties Critical Study Concerning Methanol Crossover and Proton Conductivity. *J. Membr. Sci.* **2006**, *276*, 126–134.

(10) Neburchilov, V.; Martin, J.; Wang, H.; Zhang, J. A Review of Polymer Electrolyte Membranes for Direct Methanol Fuel Cells. *J. Power Sources* **2007**, *169*, 221–238.

(11) Jorissen, L.; Gogel, V.; Kerres, J.; Garche, J. New Membranes for Direct Methanol Fuel Cells. *J. Power Sources* **2002**, *105*, 267–273.

(12) Chaabane, L.; Bulvestre, G.; Larchet, C.; Nikonenko, V.; Deslouis, C.; Takenouti, H. The Influence of Absorbed Methanol on the Swelling and Conductivity Properties of Cation-Exchange Membranes: Evaluation of Nanostructure Parameters. *Journal of Membrane Science* **2008**, *323*, 167–175.

(13) Dai, C.-A.; Liu, C.-P.; Lee, Y.-H.; Chang, C.-J.; Chao, C.-Y.; Cheng, Y.-Y. Fabrication of Novel Proton Exchange Membranes for DMFC via UV Curing. *J. Power Sources* **2008**, *177*, 262–272.

(14) Birry, L.; Bock, C.; Xue, X.; McMillan, R.; MacDougall, B. DMFC Electrode Preparation, Performance and Proton Conductivity Measurements. *J. Appl. Electrochem.* **2009**, *39*, 347–360.

(15) Du, C. Y.; Zhao, T. S.; Yang, W. W. Effect of Methanol Crossover on the Cathode Behavior of a DMFC: A Half-Cell Investigation. *Electrochim. Acta* **2007**, *52*, 5266–5271.

(16) Han, J.; Liu, H. Real Time Measurements of Methanol Crossover in a DMFC. *J. Power Sources* **2007**, *164*, 166–173.

(17) Kin, T. H.; Shieh, W. Y.; Yang, C. C.; Yu, G. Estimating the Methanol Crossover Rate of PEM and the Efficiency of DMFC via a Current Transient Analysis. *J. Power Sources* **2006**, *161*, 1183–1186.

(18) Zhang, J.; Wang, Y. Modeling the Effects of Methanol Crossover on the DMFC. *Fuel Cells* **2004**, *4*, 90–95.

(19) Iden, H.; Ohma, A.; Shinohara, K. Analysis of Proton Transport in Pseudo Catalyst Layers. *J. Electrochem. Soc.* **2009**, *156*, B1078–B1084.

(20) Suzuki, T.; Tsushima, S.; Hirai, S. Effects of Nafion® Ionomer and Carbon Particles on Structure Formation in a Proton-Exchange Membrane Fuel Cell Catalyst Layer Fabricated by the Decal-Transfer Method. *International Journal of Hydrogen Energy* **2011**, *36*, 12361–12369.

(21) Boyer, C.; Gamburzev, S.; Velev, O.; Srinivasan, S.; Appleby, A. J. Measurements of Proton Conductivity in the Active Layer of PEM Fuel Cell Gas Diffusion Electrodes. *Electrochimica Acta* **1998**, *43*, 3703–3709.

(22) Passos, R. R.; Paganin, V. A.; Ticianelli, E. A. Studies of the Performance of PEM Fuel Cell Cathodes with the Catalyst Layer Directly Applied on Nafion Membranes. *Electrochimica Acta* **2006**, *51*, 5239–5245.

(23) Mack, F.; Klages, M.; Scholta, J.; Joerissen, L.; Morawietz, T.; Hiesgen, R.; Kramer, D.; Zeis, R. Morphology Studies on High-Temperature Polymer Electrolyte Membrane Fuel Cell Electrodes. *J. Power Sources* **2014**, *255*, 431–438.

(24) Chou, J.; Jayaraman, S.; Ranasinghe, A. D.; McFarland, E. W.; Buratto, S. K.; Metiu, H. Efficient Electrocatalyst Utilization: Electrochemical Deposition of Pt Nanoparticles Using Nafion Membrane as a Template. *The Journal of Physical Chemistry B* **2006**, *110*, 7119–7121.

(25) Burk, J. J. Strategies to Produce Efficient Electrocatalysts and Improve Electrode Designs for Proton Exchange Membrane Fuel Cells. Ph.D., University of California, Santa Barbara: United States -- California, 2014.

(26) Milchev, A.; Kruijt, W.; Sluytersrehbach, M.; Sluyters, J. Distribution of the Nucleation Rate in the Vicinity of a Growing Spherical Cluster .1. Theory and Simulation Results. *J. Electroanal. Chem.* **1993**, *362*, 21–31.

(27) Milchev, A.; Heerman, L. Electrochemical Nucleation and Growth of Nano- and Microparticles: Some Theoretical and Experimental Aspects. *Electrochim. Acta* **2003**, *48*, 2903–2913.

(28) Simpkins, B. S.; Yu, E. T.; Waltereit, P.; Speck, J. S. Correlated Scanning Kelvin Probe and Conductive Atomic Force Microscopy Studies of Dislocations in Gallium Nitride. *J. Appl. Phys.* **2003**, *94*, 1448–1453.

(29) Pingree, L. S. C.; Rodovsky, D. B.; Coffey, D. C.; Bartholomew, G. P.; Ginger, D. S. Scanning Kelvin Probe Imaging of the Potential Profiles in Fixed and Dynamic Planar LECs. *J. Am. Chem. Soc.* **2007**, *129*, 15903–15910.

(30) Musumeci, C.; Liscio, A.; Palermo, V.; Samorì, P. Electronic Characterization of Supramolecular Materials at the Nanoscale by Conductive Atomic Force and Kelvin Probe Force Microscopies. *Materials Today*.

(31) Yu, Y.-J.; Zhao, Y.; Ryu, S.; Brus, L. E.; Kim, K. S.; Kim, P. Tuning the Graphene Work Function by Electric Field Effect. *Nano Lett.* **2009**, *9*, 3430–3434.

(32) Darowicki, K.; Zieliński, A.; J Kurzydłowski, K. Application of Dynamic Impedance Spectroscopy to Atomic Force Microscopy. *Sci. Technol. Adv. Mater.* **2008**, *9*, 045006.

(33) O'Hayre, R. Ionic and Electronic Impedance Imaging Using Atomic Force Microscopy. *J. Appl. Phys.* **2004**, *95*, 8382.

(34) O'Hayre, R.; Feng, G.; Nix, W. D.; Prinz, F. B. Quantitative Impedance Measurement Using Atomic Force Microscopy. *J. Appl. Phys.* **2004**, *96*, 3540.

(35) Hink, S.; Roduner, E. Application of a Contact Mode AFM for Spatially Resolved Electrochemical Impedance Spectroscopy Measurements of a Nafion Membrane Electrode Assembly. *Phys. Chem. Chem. Phys.* **2013**, *15*, 1408–1416.

(36) Yuan, X.; Wang, H.; Sun, J. C.; Zhang, J. AC Impedance Technique in PEM Fuel Cell Diagnosis - a Review. *Int. J. Hydrog. Energy (UK)* **2007**, *32*, 4365–4380.

Chapter 6: Layered Thin Film Electrodes for PEM Fuel Cells

6.1 Introduction

In addition to improvements in membrane materials, PEMFC's have a large potential for cost reductions by improvements in electrode design, particularly through reductions in platinum loading[1]. While there have been numerous advances towards increasing platinum utilization and decreasing loading,[2–8] there are questions which remain unanswered about the optimal distribution of platinum inside the electrode. Despite numerous studies and theoretical modelling,[9,10] it remains unclear how far into the catalyst layer platinum is utilized and what decrease in performance is associated with increased separation from the PEM. The only experimental study which addressed this determined that there was a linear decrease in current with distance, and established a rough distance dependence.[11] Proton transport inside of the catalyst layer is met with higher resistance due to the lower hydration state of Nafion, and as such, there are limits to how protons can travel without significant

performance losses.[12] There are also significant questions in regard to the lateral (in-plane) direction protons can be effectively transported.

Commercial electrodes consist of evenly distributed platinum throughout the carbon phase, it is not clear if this is an optimal configuration. Some studies have shown that thin (nm thick) catalyst layers can achieve extremely high performance despite the relatively tight packing of particles. [5,13] A large number of modelling studies have been employed in an attempt to model the reactant flow inside of the catalyst layer and determine the optimal distribution of platinum[9,14–18], but in many cases these are oversimplified and experimental validation is lacking. Modelling studies have predicted that an "ordered" catalyst layer, with bands of platinum perpendicular to the membrane surface should show improved performance relative to an evenly distributed system with equal loading.[19] This has also not yet been thoroughly evaluated experimentally.

Most of this modelling and experimental work has focused on the cathode, where kinetic limitations are greater and the potential for platinum loading reduction is large. The anode, however represents a good system to investigate as it removes this kinetic limitation and allows us to probe catalyst accessibility directly. In this series of experiments, we create layered electrode structures which confine the platinum into thin bands inside of the microporous layer. In this work we seek to determine what the optimal distribution of platinum inside of the electrode is, and if performance can be improved beyond what we observe in a commercial electrode.

6.2 Experimental

Our lab has developed a spin-casting electrode fabrication procedure, which we have shown is capable of creating extremely flat, uniform thin film electrodes[20]. These experiments and the characterization of these electrodes are detailed in Jonathan Burk's dissertation and the reader is directed there for a comprehensive review of this work. Briefly, inks containing platinum nanoparticles supported on porous carbon mixed with aqueous Nafion solution were mixed and ultrasonicated before use. The ink was then converted to the tertbutylammonium form (TBA) in order to give thermoplastic character to the Nafion and allow for more even films to be cast. These inks were then cast in 1 mL aliquots onto a PTFE coated fiberglass substrate and dried inside of a vacuum oven at 130 C after each layer. This process was repeated until the desired mass of platinum was obtained (generally 3-5 layers of ink). To create MEA's using these electrodes, they were hot pressed onto either side

of a Nafion membrane at 130 C. While testing, a carbon cloth gas diffusion layer was placed over the decal electrode. In most cases we used a commercial electrode as the opposite electrode in these systems in order to test the effect of replacing a single electrode.

Example Topographic AFM images of these spin cast electrodes are shown in Figure 6.1 and demonstrate their reduced surface roughness relative to a hand-painted decal. The surface roughness is also much lower than that of a commercial electrode (not shown). We correlated this reduced roughness with a reduced

electrical resistance, and thus improved cell performance. Extensive surface and electrochemical characterization was also conducted and is detailed in Jonathan Burk's dissertation.

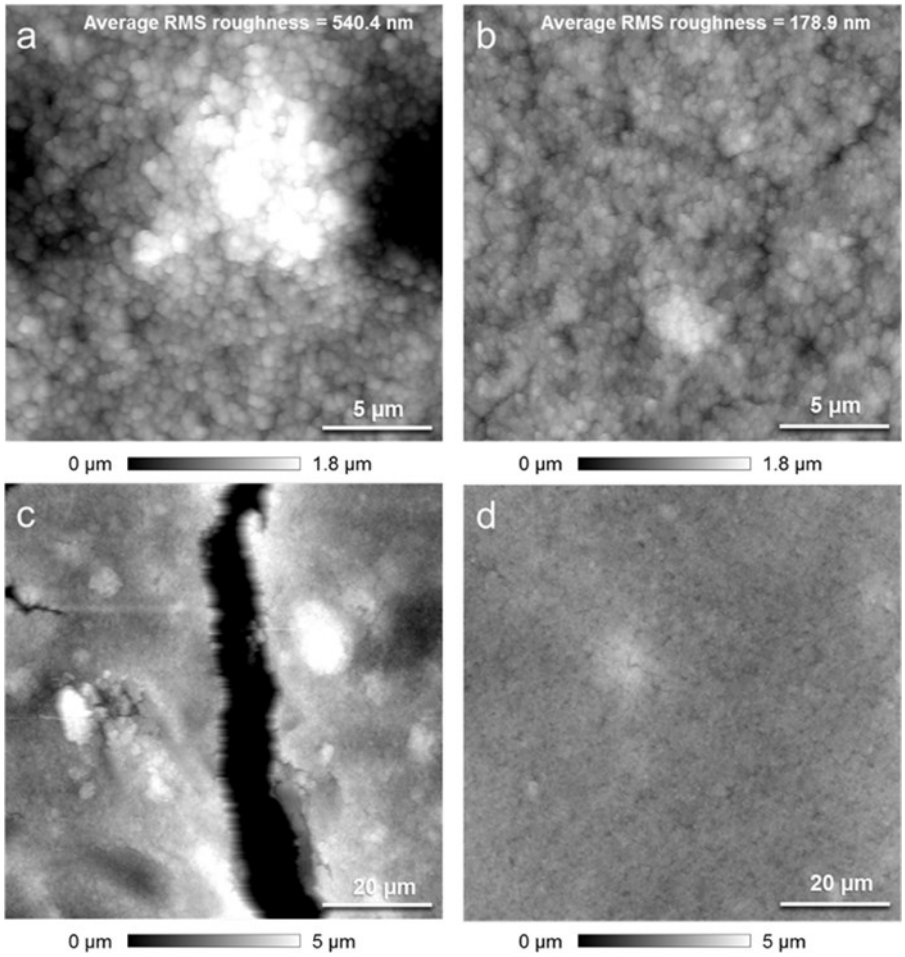

Figure 6.1: Large (a,b) and very large scale (c,d) topographic images of hand painted (a,c) and spin cast (b,d) thin film decal electrodes.

To fabricate layered electrodes, we conducted a similar fabrication procedure, but with two separate inks; a catalyzed and uncatalyzed ink. The catalyzed ink was made from either 20% Pt on Vulcan mixed with a 3:2 mass ratio of carbon to Nafion using

an aqueous Nafion solution (5% by weight, FuelCellsEtc.). This ink was then diluted tenfold in order to give a low viscosity ink that could create extremely thin layers when spin cast. Figure 6.1 shows a topographic image of a single layer of catlalyzed ink deposited onto the fiberglass substrate and shows that it is extremely thin (~ 500 nm) and extremely smooth, with an rms roughness of only 144 nm. This is approaching the size of single Vulcan carbon particles, which are generally 60-80 nm in diameter. This demonstrates our ability to effectively deposit and localize catalyst in an extremely thin layer.

With this capability we interspersed extremely thin, catalyzed layers in between uncatalyzed layers containing only carbon and Nafion. While we were not able to gauge the thickness of every layer, we were able to measure the mass of carbon or platinum/carbon deposited with very high precision. By assuming constant density and thickness we were then able to back out the thickness of carbon. This enabled us to construct electrodes with constant thickness (to within 1 μm), and constant platinum loading to within 5μg/cm^2. This represents a much more accurate determination of thickness than previous work, as well as a smaller possible increment of distance.

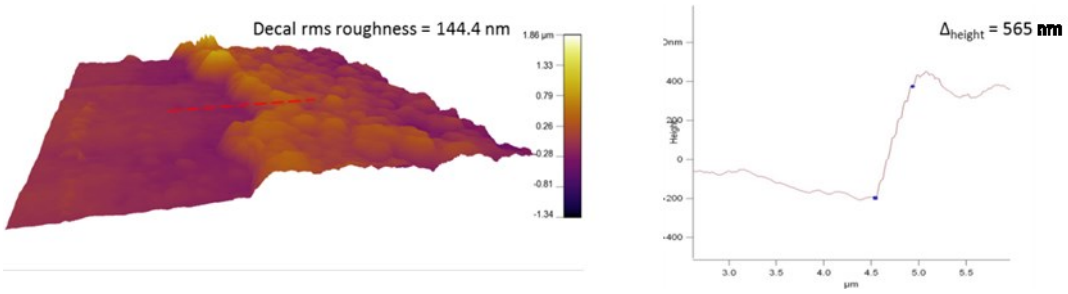

Figure 6.2: 3-D topographic AFM image (left) showing an exposed cross section of a thin catalyzed carbon layer on a PTFE coated fiberglass substrate. A corresponding line cut used to measure thickness (right).

For fuel cell characterization, 1cm^2 decal electrodes were hot pressed onto a Nafion 212 membrane at 130°C at 500 lbs for 3 minutes. It was found that ion-exchanging the Nafion in the catalyst layer from TBA^+ form to H^+ form by boiling in 0.5M sulfuric acid for 12 hours had no effect on fuel cell performance, so all cells were run without ion exchanging. Many cells contained a commercial electrode at the anode Prior to testing, we subjected each cell to an extended (~16 hour) break in period at high temperature and relative humidity and it is likely that this caused the decals to become ion exchanged before testing was conducted. Carbon cloth gas diffusion layers were placed at the anode and cathode between the decal electrodes and bipolar plates of the cell assembly. A Scribner 850C fuel cell test station was used with H_2/air stoichiometry of 18:24 and a 65 C cell and gas inlet temperature, back pressure at the anode and cathode was 35 kPa.

6.3 Investigating the Effect of Location of Platinum on Cell Performance

For our first series of experiments, we sought to investigate the depth dependence of platinum placement on the performance of the cell. Because our catalyst layers generally had low loading we began by using a layered electrode as the anode catalyst layer, where there is less kinetic limitation and thus lower loadings are more feasible. For these studies we often refer to electrodes as "Layer 1, Layer 2 etc." and this refers to the catalysts proximity to the membrane, where layer 1 is closest. The difference between layers is about 1.5 microns, as this is the thickness of single uncatalyzed layers.

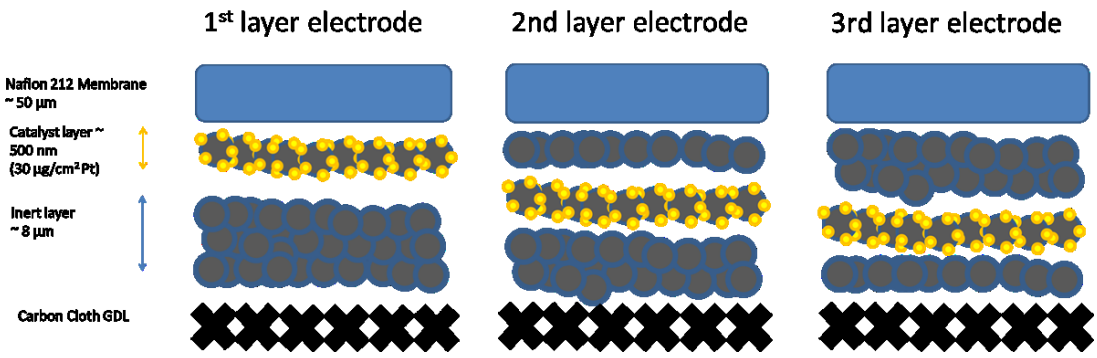

Figure 6.3: Schematic representation of the construction of layered thin film electrodes.

In order to insure that layers are not intermixing either during the casting of subsequent layers or during hot pressing or cell operation, we cryofractured cross-sections of multiple cells at all stages of fabrication and testing. We then imaged these cross-sections with scanning electron microscope (SEM) and used energy dispersive spectroscopy (EDS) in order to discern the regions which had platinum.

Figure 6.3 shows an SEM image and corresponding EDS line scan of a "layer 1" electrode which show that the platinum is still localized in a sub-micron thick layer.

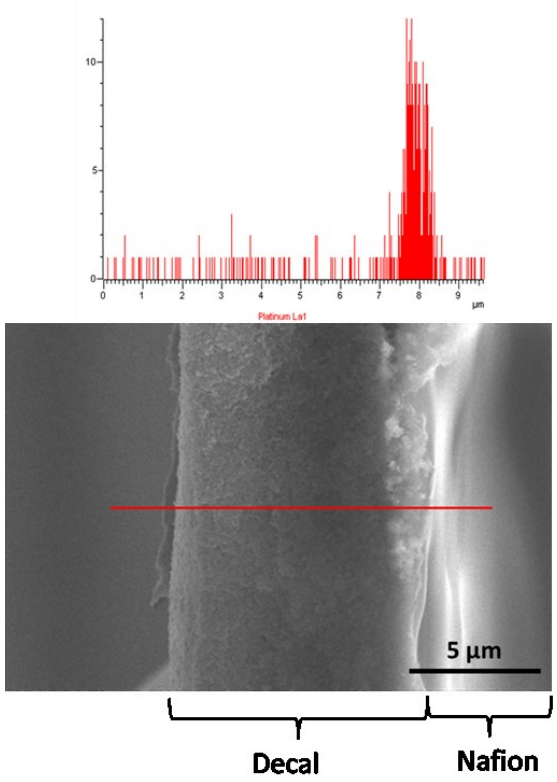

Figure 6.4: SEM image with corresponding EDS linescan of the platinum α peak signal showing the distribution of platinum inside of a layered thin film decal electrode.

Similar images were obtained for layers deeper inside the electrode, and we saw no effect of running the fuel cell on this dispersion of platinum. It is, however, likely that if this cell was run for long periods of time, a slow migration of platinum would be observed from dissolution and redeposition of platinum. This is a common issue in fuel cells and work by many groups is aimed at finding methods to anchor

platinum to the surface and immobilize it such that catalytic activity is not lost over long periods of operation.

The thickness of the electrode in figure 6.3 (~10 μm) was typical for these experiments though this varied by up to a micron over the entire electrode and between electrodes. We constructed a series of fuel cells with varying separation from 0-8 μm and with a catalyst layer of equal thickness and loading (~35 μg) in each case. We see that the layer 1 electrode achieve performance which is almost indistinguishable from a commercial electrode despite having more than 10 times lower platinum loading. This is a good indicator that kinetic limitations at the anode are minimal and that our loadings are adequate for this study.

As platinum is moved further back into the electrode and away from the membrane interface, the performance gradually decreases, as is expected. This decrease appears largely in the ohmic region, since protons must travel further inside of the catalyst layer where resistance is higher than in the membrane. This makes for a higher overall resistance and lower voltage. It appears that any difference in mass transport in these cells is minimal, as evidenced by similar behavior at high current densities. Interestingly, even at layer 6, with 8 μm between the catalyst and PEM, the cell maintains about half of its short circuit current. This implies that catalyst particles far from the interface can still contribute significantly to fuel cell performance, albeit with increased resistance.

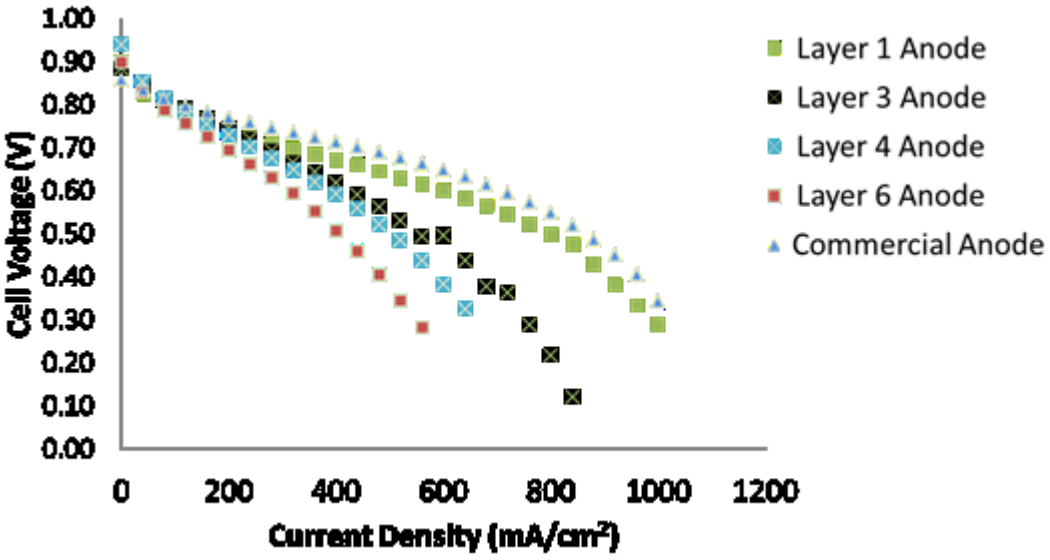

Figure 6.5: I-V polarization curves of MEA's containing several different layered thin film anodes. An MEA with commercial anode is also plotted for comparison. All MEA's had a commercial electrode as a cathode.

This work agrees fairly well with the previous study by Boyer et al. and tells us that the previous estimate of 20 μm for the effective distance from the membrane at which platinum can still be utilized is relatively accurate.

We next ran an identical set of cells with a layered electrode at the cathode and a commercial electrode at the anode. For these experiments, a thicker catalyst containing layer was applied in order to achieve a higher loading to the expected mass transfer at the cathode. We used a loading of 120 μg for these cells but determined that even with this loading, kinetic limitations are still an issue. Figure 6.4 shows "the layer 1" cathode cell with a commercial anode next to the layer 1 anode with a commercial cathode. We see that at low current densities there is a

larger activation loss, and then a sharp drop in the mass transfer regime, consistent with a kinetic limitation at the cathode. For this reason, these experiments were not pursued further and the anode was targeted as a means to improve performance.

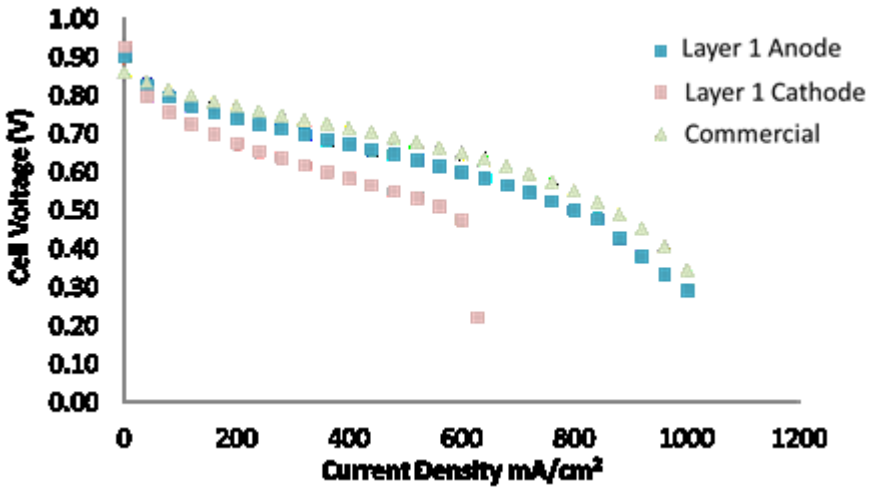

Figure 6.6: I-V polarization curves of MEA's containing, a 35 µg Pt layered anode with commercial cathode, a 120 µg Pt layered cathode with commercial anode, and a cell with two commercial electrodes.

Other experimental work focused on the fuel cell cathode used a sputtering technique and made a similar assessment; that confining the platinum into thin layers results in improved performance.[13] It is not known if this phenomenon is unique to the cathode, or if anode performance can be similarly increased by this method.[13] We sought to determine this experimentally by fabricating layered electrodes with multiple thin platinum layers in order to approximate this structure. We experimented with anodes using 60µg platinum loadings with a variety of different platinum distributions. Of these, we found that an electrode where 4 separate thin catalyzed layers were interspersed between inert layers outperformed a commercial

anode. Each layer had an approximate platinum loading of 15µg and a thickness of 300 nm. These were spaced between 1.5 µm thick uncatalyzed layers. We found that this cell shows improved performance in the activation and ohmic region of the polarization curve, implying improved proton transport to the membrane, and possibly a more efficient 3 phase reaction zone.

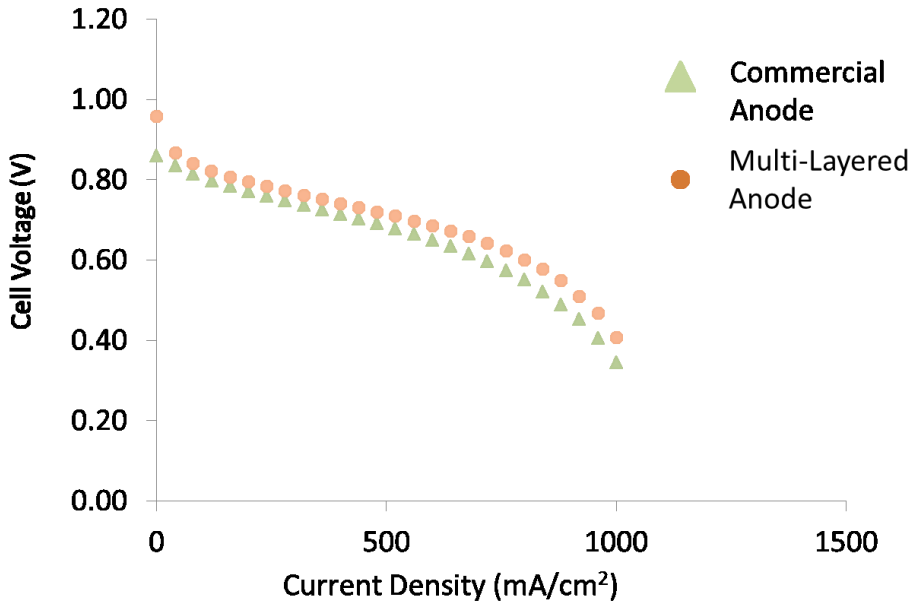

Figure 6.7: I-V polarization curves of MEA's containing, a commercial anode, and multi-layered thin film anode with 60 µg platinum loading. Both Cells used a commercial electrode as a cathode.

The fact that we can create an anode which outperforms a commercial electrode with considerably reduced loading is impressive in itself. The DOE target for total platinum loading for a PEM fuel cell is 125 µg by 2020[21], of which a large fraction must be used at the cathode. While further optimization is required, these experiments show the performance gains that are possible through using layered electrodes. Ongoing work on these electrodes is aimed at further reducing loading,

and investigating different layering configurations to further optimize platinum distribution. Investigation of layered cathodes is also underway as this should follow similar behavior to the anode, but with an additional kinetic limitation which must be factored in when choosing a target platinum loading.

A final set of experiments that we conducted was to vary the Nafion content throughout the depth of the electrode. In this experiment we made a series of inks with varying Nafion content (20 wt % - 60 wt%) and cast them in order to give such a depth profile. The platinum depth profile was kept relatively constant by mixing 60% PT on C powder with uncatalyzed Vulcan XC-72 in order to achieve the desired Pt loading in each layer. The electrode shown here has 75 μg of platinum, considerably more than the 35 μg in the layer 1 anode shown on the same plot. What we see in the polarization curves for this electrode is that while the activation region is identical, the ohmic section has considerably higher resistance. This implies that the effective ionic resistance is higher, likely due to a less effective interface. These finding support the idea that while a three phase reaction zone is necessary, a flat membrane electrode interface with a sharp compositional change is preferable to one with a slowly changing composition. These experiments also do not take into account the effect of hot pressing this decal onto the membrane, which could alter the

Nafion distribution in the electrode.

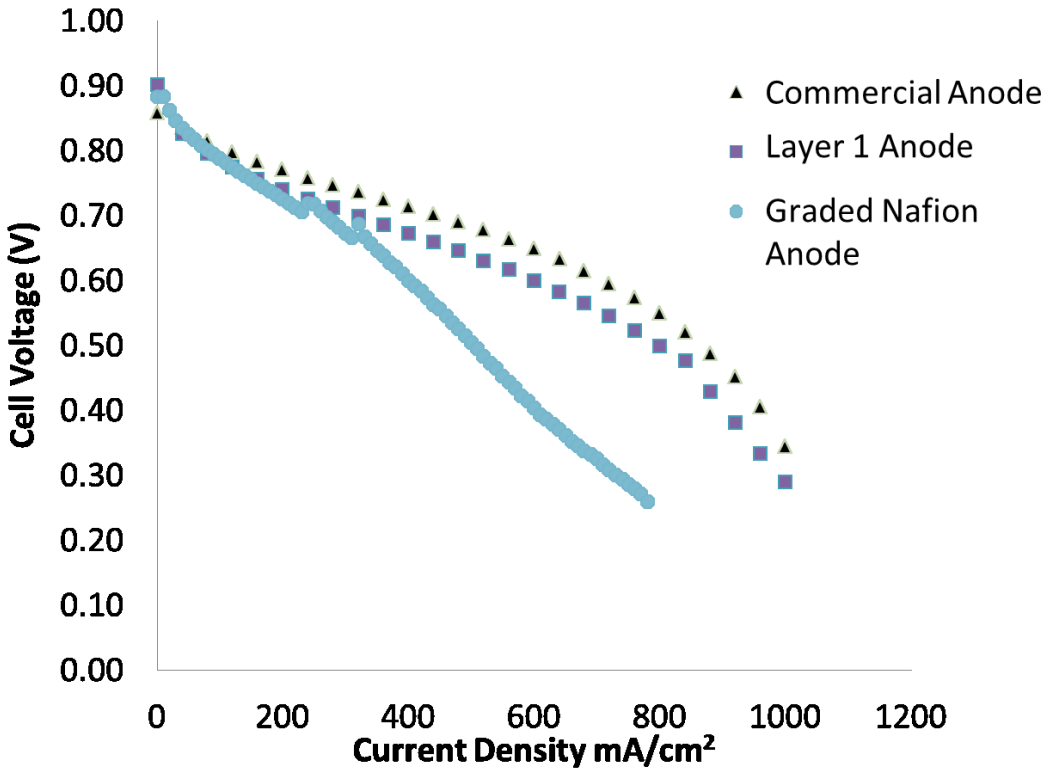

Figure 6.8: I-V polarization curves of an MEA with graded Nafion and carbon composition, layer 1 and commercial anodes are shown for comparison. All cells used a commercial electrode as a cathode.

6.4 Conclusions

In this section we describe experiments aimed at better understanding the optimal distribution of platinum inside the catalyst layer of PEM fuel cells. We showed that we can create thin film electrodes with a highly localized platinum containing layer and used this to probe the effect of limited proton conductivity inside of the catalyst layer. We found that at distances of up to 8μm over half of the short circuit current of

the cell is maintained, implying that distances of over 10 μm are easily accessible, in agreement with previous predictions.

We then used this technique to create multi-layered electrodes which showed improved performance over a commercial anode despite having a platinum loading of only 60μg as opposed to the 500 μg found in a commercial electrode.

Our layer by layer spin-casting technique is highly versatile and will allow for future experiments to explore different electrode configurations where components vary with depth. These experiments are still in their early stages, and much work remains to be done in determining the optimal distribution of platinum inside of the catalyst layer, both on the anode and cathode sides of the cell. Another promising avenue is to employ different inks to tune porosity[22] and create a hierarchically porous carbon phase[23] in order to improve gas permeability to catalyst particles. These improvements could play a large role in improving cell performance and moving close to the DOE targets for reduced platinum loading.

References

(1) Litster, S.; McLean, G. PEM Fuel Cell Electrodes. *Journal of Power Sources* **2004**, *130*, 61–76.

(2) Ticianelli, E. A.; Beery, J. G.; Srinivasan, S. Dependence of Performance of Solid Polymer Electrolyte Fuel Cells with Low Platinum Loading on Morphologic Characteristics of the Electrodes. *J Appl Electrochem* **1991**, *21*, 597–605.

(3) Wilson, M.; Valerio, J.; Gottesfeld, S. Low Platinum Loading Electrodes for Polymer Electrolyte Fuel-Cells Fabricated Using Thermoplastic Ionomers. *Electrochim. Acta* **1995**, *40*, 355–363.

(4) Zeis, R.; Mathur, A.; Fritz, G.; Lee, J.; Erlebacher, J. Platinum-Plated Nanoporous Gold: An Efficient, Low Pt Loading Electrocatalyst for PEM Fuel Cells. *J. Power Sources* **2007**, *165*, 65–72.

(5) O'Hayre, R.; Lee, S.-J.; Cha, S.-W.; Prinz, F. B. A Sharp Peak in the Performance of Sputtered Platinum Fuel Cells at Ultra-Low Platinum Loading. *Journal of Power Sources* **2002**, *109*, 483–493.

(6) Cha, S. Y.; Lee, W. M. Performance of Proton Exchange Membrane Fuel Cell Electrodes Prepared by Direct Deposition of Ultrathin Platinum on the Membrane Surface. *J. Electrochem. Soc.* **1999**, *146*, 4055–4060.

(7) Song, Y.; Ma, Y.; Wang, Y.; Di, J.; Tu, Y. Electrochemical Deposition of Gold-Platinum Alloy Nanoparticles on an Indium Tin Oxide Electrode and Their Electrocatalytic Applications. *Electrochimica Acta* **2010**, *55*, 4909–4914.

(8) Taylor, E. J.; Anderson, E. B.; Vilambi, N. R. K. Preparation of High-Platinum-Utilization Gas Diffusion Electrodes for Proton-Exchange-Membrane Fuel Cells. *J. Electrochem. Soc.* **1992**, *139*, L45–L46.

(9) Broka, K.; Ekdunge, P. Modelling the PEM Fuel Cell Cathode. *Journal of Applied Electrochemistry* **1997**, *27*, 281–289.

(10) Modeling of PEMFC Catalyst Layer Performance and Degradation - Springer. In.

(11) Boyer, C.; Gamburzev, S.; Velev, O.; Srinivasan, S.; Appleby, A. J. Measurements of Proton Conductivity in the Active Layer of PEM Fuel Cell Gas Diffusion Electrodes. *Electrochimica Acta* **1998**, *43*, 3703–3709.

(12) Springer, T. E.; Zawodzinski, T. A.; Wilson, M. S.; Gottesfeld, S. Characterization of Polymer Electrolyte Fuel Cells Using AC Impedance Spectroscopy. *J. Electrochem. Soc.* **1996**, *143*, 587–599.

(13) Fofana, D.; Natarajan, S. K.; Hamelin, J.; Benard, P. Low Platinum, High Limiting Current Density of the PEMFC (proton Exchange Membrane Fuel

Cell) Based on Multilayer Cathode Catalyst Approach. *Energy* **2014**, *64*, 398–403.

(14) Weber, A. Z.; Newman, J. Modeling Transport in Polymer-Electrolyte Fuel Cells. *Chem. Rev.* **2004**, *104*, 4679–4726.

(15) You, L. X.; Liu, H. T. A Two-Phase Flow and Transport Model for the Cathode of PEM Fuel Cells. *Int. J. Heat Mass Transf.* **2002**, *45*, 2277–2287.

(16) Eikerling, M.; Kornyshev, A. A. Modelling the Performance of the Cathode Catalyst Layer of Polymer Electrolyte Fuel Cells. *J. Electroanal. Chem.* **1998**, *453*, 89–106.

(17) Song, D.; Wang, Q.; Liu, Z.; Eikerling, M.; Xie, Z.; Navessin, T.; Holdcroft, S. A Method for Optimizing Distributions of Nafion and Pt in Cathode Catalyst Layers of PEM Fuel Cells. *Electrochimica Acta* **2005**, *50*, 3347–3358.

(18) Gurau, V.; Liu, H. T.; Kakac, S. Two-Dimensional Model for Proton Exchange Membrane Fuel Cells. *AICHE J.* **1998**, *44*, 2410–2422.

(19) Du, C. Y.; Yang, T.; Shi, P. F.; Yin, G. P.; Cheng, X. Q. Performance Analysis of the Ordered and the Conventional Catalyst Layers in Proton Exchange Membrane Fuel Cells. *Electrochimica Acta* **2006**, *51*, 4934–4941.

(20) Burk, J. J. Strategies to Produce Efficient Electrocatalysts and Improve Electrode Designs for Proton Exchange Membrane Fuel Cells. Ph.D., University of California, Santa Barbara: United States -- California, 2014.

(21) Fuel Cell Technologies Program Multi-Year Research, Development and Demonstration Plan - 3.4 Fuel Cells - Fuel_cells.pdf.

(22) Shin, S.-J.; Lee, J.-K.; Ha, H.-Y.; Hong, S.-A.; Chun, H.-S.; Oh, I.-H. Effect of the Catalytic Ink Preparation Method on the Performance of Polymer Electrolyte Membrane Fuel Cells. *Journal of Power Sources* **2002**, *106*, 146–152.

(23) Lee, J.; Kim, J.; Hyeon, T. Recent Progress in the Synthesis of Porous Carbon Materials. *Adv. Mater.* **2006**, *18*, 2073–2094.

Chapter 7: Conclusions and Future Directions

In this thesis we have shown that AFM is a powerful tool for characterizing proton exchange membranes and have been able to make advances in understanding the complex behavior that these materials exhibit during fuel cell operation. While other techniques such as SAXS, impedance spectroscopy, and dynamic mechanical analysis are useful for obtaining bulk structural information, the spatially resolved nature of AFM allows us to investigate the spatial variation in these same properties and to observe phenomena that bulk techniques might miss. This in turn allows for the development of a more detailed structure-property relationship which can aid in the design of new materials which improve on proton conductivity, mechanical strength and durability.

One focus of this work was to characterize the phase separated morphology of PEM's as they become hydrated and dehydrated in the variable environment found inside of a fuel cell. Promising future directions for this work include in situ measurements of membrane hydration and dehydration and physically capturing these transitions in morphology in order to understand their time dependence. The high temperature AFM work done in this thesis also has great potential as a

technique to evaluate new membrane materials for high temperature operation. These include, but are not limited to porous Teflon supported membranes such as gore select, inorganic composites, and cross-linked membrane systems.

Another promising direction is to study anion exchange membranes, these membranes offer the potential to use non-noble metal catalysts due to improved kinetics. Anion exchange membrane development is still in its early stages and great strides in material development could be made with the aid of AFM techniques.

An important direction for future fuel cell research is to decrease the platinum loading in cells or remove it altogether. Towards reducing platinum loading, we have shown that our layer by layer spin casting technique gives a simple yet versatile route to exploring layered electrode structures. Continuing off our initial studies here, there are a wide range of possible layered structures to explore with the aim of increasing platinum utilization and decreasing loading. We have also demonstrated that cp-AFM is an effective technique for evaluating the efficiency of templated electrodeposition allowing us to address performance losses in these ultra-low loading electrodes and zero in on the minimum possible platinum loading.

Conductive probe AFM has undergone numerous technical advances since our group first started using this technique. Ac-mode cp-AFM represents a promising technique due to its ability to directly couple mechanical and electrochemical measurements. Further advances could take advantage of other nanomechanical scanning modes such as contact resonance AFM or amplitude modulated frequency modulated (AM FM) AFM to enable the extraction of additional mechanical

information. The ability to image using liquid fuel feeds represents another interesting avenue of research which could be useful for evaluating new membranes for direct methanol fuel cells. Tailoring of this technique may even allow for methanol crossover through the membrane to be spatially mapped alongside proton conductivity, providing a valuable tool for improving these systems.

PEM fuel cells are on the cusp of being a commercially viable power source, and through these types of fundamental experiments, material design can be improved to the point where they reach this goal. It is my hope that the work in this thesis can continue to be built upon and contribute to this greater research effort.

Appendix 1: Photoconductive AFM of Nanostructured Photoelectrochemical Cells

A1.1 Introduction

Artificial photosynthesis using "cell-like" autonomous devices to carry out redox chemistry and produce useful fuels or chemicals has long been a goal of solar energy researchers[1–3]. Solar-to-chemical conversion at high efficiencies has been demonstrated with clever use of high quality devices based on thin film semiconductors such as silicon and gallium arsenide[4–6]. However, the devices reported thus far suffer from poor stability and/or high cost [7,8]. A major barrier is the development of cost-effective device structures which efficiently couple and integrate individual photoelectrochemical conversion components (light absorbers + electrocatalysts) into a manufacturable, sustainable, artificial photosynthetic unit. Recently we described one such strategy for fabricating an integrated photoelectrochemically active heterostructure (PAH) comprised of a high efficiency semiconductor light absorber capped with oxidation and reduction electrocatalysts.[9] To protect high efficiency semiconductors from corrosive electrolytes, an array of PAHs are created in porous anodic aluminum oxide membranes with each unit

physically, chemically, and electronically isolated from its neighbors by the stable alumina cellular enclosure and capping electrocatalysts. The resulting structures are a high-density array (10^9 - 10^{10}/cm^2) of nanostructured, corrosion resistant, fault tolerant, autonomous photoelectrochemically active units. Using the above device architecture we demonstrated free floating artificial photosynthetic devices that produced hydrogen at a stable rate for over 24 hours in corrosive hydroiodic acid electrolyte (pH=2) with overall energy efficiency of 2.9% for conversion of absorbed solar spectrum light into stored chemical potential energy (as molecular hydrogen). The above strategy also facilitates assembly of individual nanoscale functional units into macroscopic functional devices that can be manufactured at large scale and integrated into enormous solar-to-chemical systems – a prerequisite for developing commercially significant solar processes.

To improve the design and efficiency of the photosynthetic heterostructures, it is important to understand and optimize the interfacial reactions and rate determining steps of the photon-to-chemical transport pathways in these light sensitive high-density nano architectures both individually and collectively. In particular, the electronic behavior and absolute band offsets of nanoscale structures and interfaces are difficult to predict based on bulk material models.[10,11] Hence, understanding and controlling interfacial electronic properties should be made a high priority in order to achieve efficient design and utilization of such material structures.

Atomic force microscopy (AFM) techniques have proven especially well-suited to studying the electrical properties of semiconductor samples with nanometer resolution.[12,13] Conductive probe atomic force microscopy (cp-AFM) specifically has been used to characterize properties such as photoconductivity[14–177], piezoelectric response[18–21], and charge transport[22,23] in a variety of nanostructured semiconductor samples. Recently, other groups have shown that cp-AFM techniques are effective at examining photoconductivity in inorganic semiconductor electrodes used in photosynthetic devices.[24,25] In the case of photosynthetic cells such as ours, electrochemical measurements are an important addition to solid state techniques in order to determine how solid state electrical properties translate into photosynthetic efficiency with the addition of an electrolyte.[26] Importantly for *in situ* characterization, the high resolution of AFM can be retained in aqueous environments allowing for spatially resolved electrochemical measurements.[27,28]

In this letter we employ cp-AFM to investigate the photocurrents and photovoltages present in individual n-$CuInSe_2$/Au Schottky barrier PAH structures within a large array device consisting of ~10^9 such PAH units. We explore the relationship between the individual unit properties at the nano-scale and the bulk performance of the overall device. By comparing these results to a planar device architecture we are able to better understand the advantages of the PAH cell design over conventional thin film structures. Unique to this work is the use of conductive/photoconductive atomic force microscopy in both solid and solution-phase environments to investigate the photoelectric and photoelectrochemical

properties of individual PAH's. This technique is shown to be effective at separating the individual performance of each PAH from the bulk device performance. Differences in solid and liquid state behavior also give insight into the processes occurring at the electrode under operating conditions.

A1.2 Experimental Methods.

Details of the fabrication of PAH structures in porous alumina templates, and some of the post-growth fabrication steps, have been reported previously[30]. Briefly, n-$CuInSe_2$ nanorods with rod diameters of ~120nm were electrodeposited in a porous anodic aluminum oxide template that was prepared on a transparent ITO/TiO_2 conducting substrate[31]. n-$CuInSe_2$ was electrodeposited as described previously[32]. This was followed by gold deposition which acts as a Schottky barrier to the underlying semiconductor[33]. All electrodeposition runs were carried using a standard calomel electrode as the reference electrode and Pt mesh as the counter electrode. Cyclic voltammetry was conducted on a potentiostat (Bio-Logic SAS, VSP model) using a 400mM $K_3Fe(CN)_6$ / $K_4Fe(CN)_6$ aqueous solution as an electrolyte and Pt mesh as a counter electrode. Detailed structure was determined using scanning electron microscopy (SEM)(FEI Sirion XL30), and energy-dispersive x-ray spectroscopy (EDS)(Oxford Inca).

AFM images were collected on an Asylum Research MFP3D-SA using a standard ORCA module with a 500 MΩ sensitivity which allowed for conductive imaging. Tapping mode imaging was conducted using a silicon cantilever

(MikroMasch NSC15) with a nominal spring constant of 40 N/m. Conductive imaging employed a Pt-Ir coated silicon cantilever (MikroMasch HQ-DPER-XSC11) the longest lever was used which had a nominal spring constant of 0.2 N/m and tip radius of 25nm. Typical contact forces during I-V curves and scanning were ~40nN. All scans were conducted at 1Hz, with 512 x 512 points, and no image modification was used for any images. To collect current-voltage (I-V) curves, a scan was first taken over the desired area and a specific point was selected. The tip was then engaged at the same contact force and I-V curves were collected with an external source meter (Kiethley 2612-A). Solution I-V measurements utilized a 400mM $K_3Fe(CN)_6$ / $K_4Fe(CN)_6$ aqueous solution as an electrolyte. As a light source we used the 150W halogen lamp that is built in to the AFM (FiberLite M-150R), employing a calibrated silicon photodiode as a reference, we determined that the irradiance on the sample was ~1000 mW/cm^2.

A1.3 Results and Discussion

The photovoltaic (PV) and photoelectrochemical (PEC) devices were fabricated on an ITO substrate coated with TiO_2 which served as a hole-blocking layer (see Experimental Methods for more details). $CuInSe_2$ nanorods were electrochemically synthesized on the TiO_2 /ITO substrate in the nanopores of porous anodic aluminum oxide (AAO) prepared by Al anodization. $CuInSe_2$ nanorods were then capped by electrodepositing gold which acts as the Schottky barrier top contact, while the ITO served as the back contact. The scanning electron microscopy (SEM) and tapping

mode AFM were employed to characterize the morphology of the PAH array devices. The $CuInSe_2$/Au multi segmented nanorods used in this study were ~350 nm long ($CuInSe_2$ - 300±10 nm; Au - 50±20 nm), with diameters ≈ 120±15 nm and with inter-rod gaps ~ 30±20 nm with the density of PAH's in the array was found to be ~$10^9/cm^2$ (Figure 1a-b). Cross sectional SEM (not shown) verified that the thin conductive ITO/TiO_2 layer at the bottom of the array was in good contact with the semiconductor of the PAH and there were no shorts between the PAH's. Tapping mode AFM (Figure 1c) was employed to examine the topography of the surface, and showed minimal variation in height of the alumina surface. The high elevation areas correspond to the nanoporous alumina, while the low elevation areas are pores in the alumina where the PAH's were electrodeposited. The pore diameters and areal density determined by AFM were in good agreement with SEM analysis. Due to the size and aspect ratio of the AFM tip, it was found that the tip could only descend ~30nm into each pore. This was a critical factor when constructing samples, as devices where PAH's were more than 30 nm below the pore mouth of the alumina substrate did not allow for PAH's to be contacted with the AFM tip. For this reason, conductive images of the sample in Figure 1c showed no measureable conductivity or photoactive behavior without first reducing the height of the alumina by etching. The alumina in these cells was chemically etched using 0.1M sodium hydroxide until the electrocatalyst surface (gold in this case) of the PAH's protruded above the alumina. Figure 1d shows a topographic image of a cell where the alumina has been etched away, leaving the PAH structures as the tall features in this image.

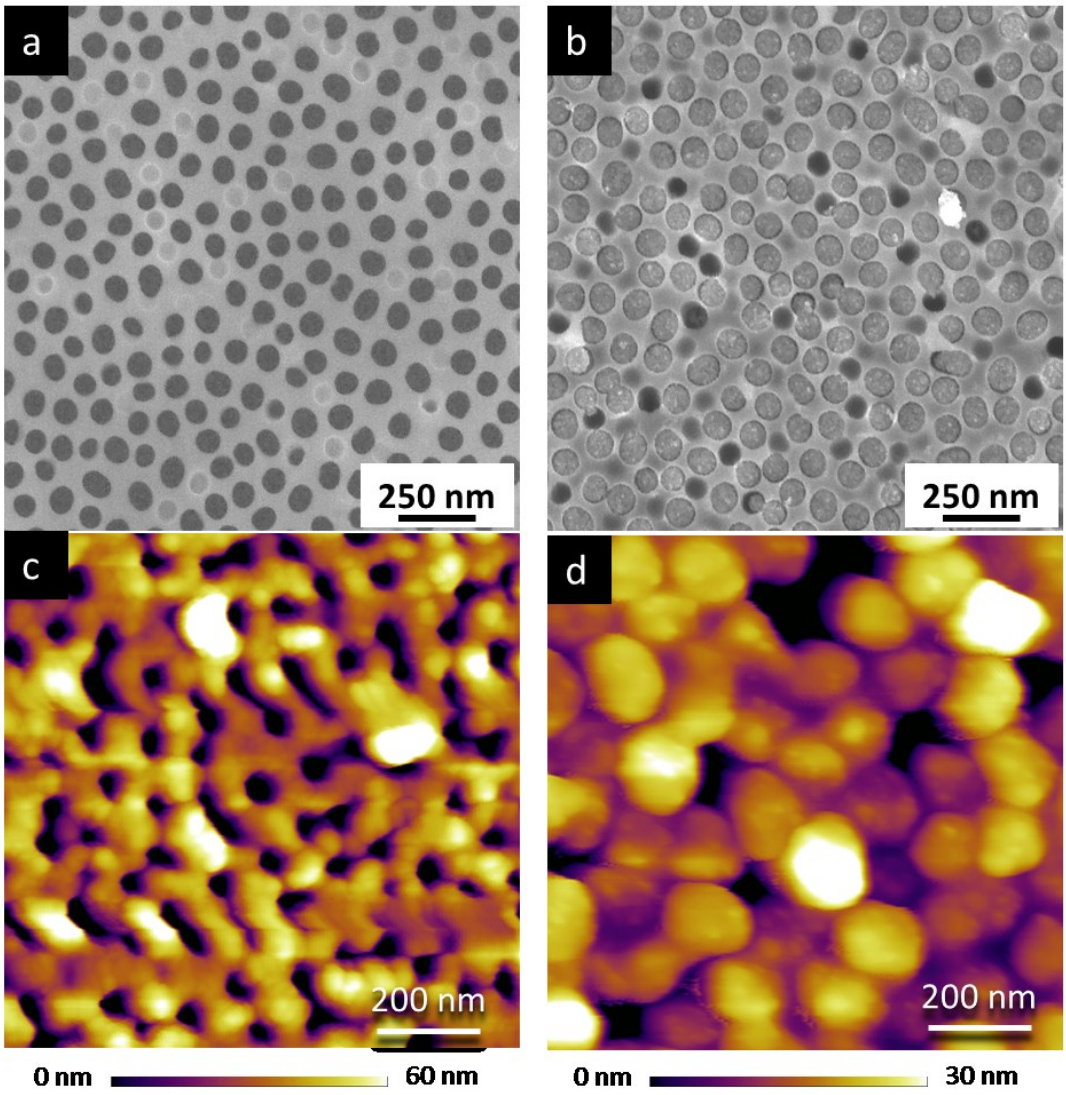

Figure A1.1: Scanning electron microscopy images of PAH structures grown inside porous alumina prior to (a) and after (b) electrochemical etching of the alumina (c) shows the tapping-mode AFM topography of the porous alumina prior to etching and (d) AFM topography of exposed PAH structures after electrochemical etching.

Several PAH array devices were fabricated by the procedure outlined above. Different degrees of etching were used to achieve devices whereby the PAH's could be contacted by the AFM tip but remained electronically isolated from each other. To acquire solid state conductive AFM measurements, a $CuInSe_2$ PAH sample with a gold Schottky barrier was etched until the alumina was ~50 nm below the top of the PAH's. It was found that the reliable electrical contact enabled by the gold layer facilitated reproducible current measurements. Figure 2a shows a schematic of measurement set-up with corresponding topographic and photoconductive images (Figure 2b). The photoconductive images were collected under +2V sample bias. It was found that the sides of PAH's typically exhibited the largest currents, which implies more efficient charge transport at these locations. This could also be influenced by the high aspect ratio of the AFM tip leading to increased tip-sample contact in this configuration.

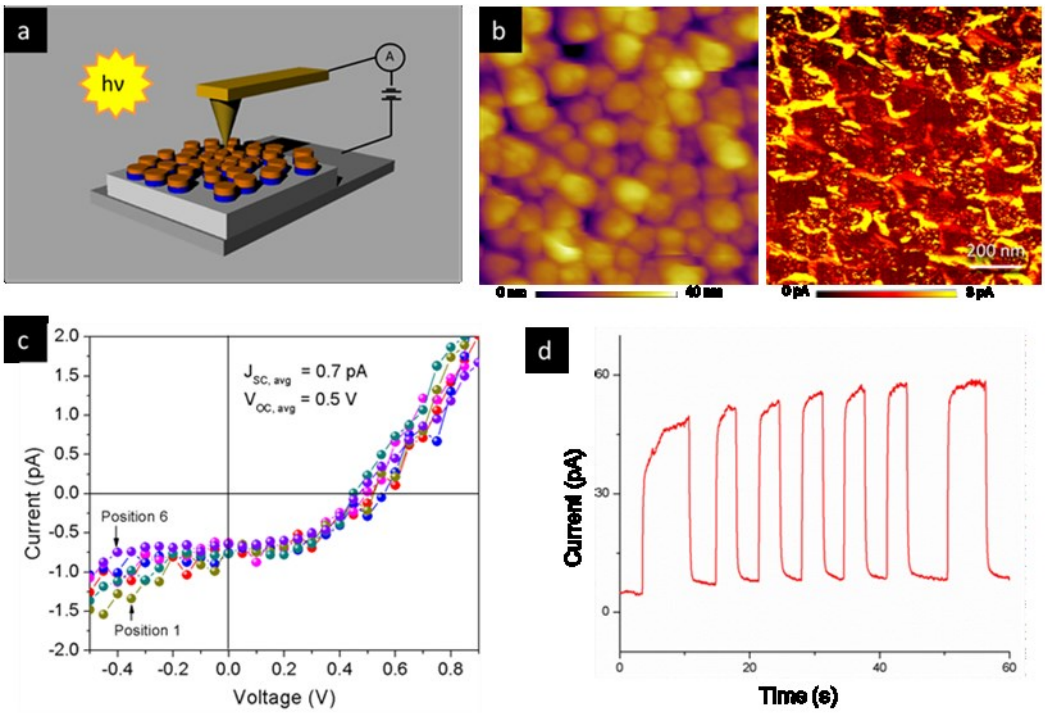

Figure A1.2: Schematic representation of our cp-AFM setup (a) and example topographic and photoconductive AFM images (b). Several I-V curves from individual PAH's are shown in (c) and (d) shows the current flowing through a single PAH held at +3 V while the light source is toggled on and off.

The solid-state current–voltage curves of typical PAHs in the dark and under visible light illumination are presented in Figure 2c. All PAH units showed good rectification behavior with minimal spatial variation (less than 10%) across large area scans. The open-circuit potential (*V*oc) of a typical PAH unit was 0.50 V, with a short-circuit photocurrent (Jsc) of 0.7 pA, and a fill factor (FF) of 0.42. The photocurrents obtained from each PAH unit were very reproducible. Figure 2d shows the current passing through a single PAH at +3V sample bias under chopped light illumination showing the rapid rise of current upon illumination up to a stable value, and the reproducible switching that occurs.

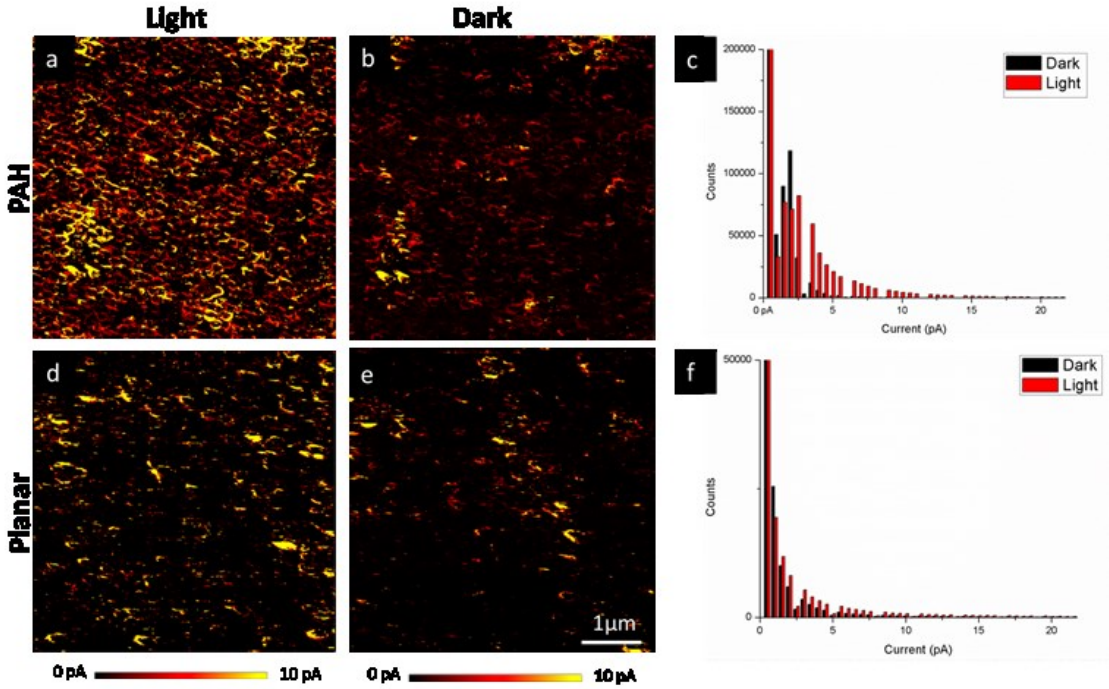

Figure A1.3: Large scale conductive AFM images at a fixed location and +2V sample bias, with (a,d) and without (b,e) illumination for PAH (a,b) and planar (d,e) $CuInSe_2$/Au cells. (c, f) Corresponding histograms showing the distribution of current values in the PAH and planar cells respectively.

By contrast the results of similar measurements carried out on an electrochemically grown $CuInSe_2$/Au thin film device showed very low photovoltages (<0.1V) and low photocurrents (Figure 3) with majority of the areas shorted, likely due to the cracks created as a result of fabrication process. Although such shorting paths might be present for the PAH devices, its autonomous operation (each unit is electronically isolated from one another) makes it extremely fault tolerant whereas a single shorting path might cause bigger problems for thin film based devices during subsequent Schottky barrier metal deposition. Figure 3 shows large scale (5 µm) conductive images in the dark and under illumination of the PAH

cell described previously as well as a planar $CuInSe_2$ device with identical Schottky barrier contacts. These images were collected under a +2V sample bias in order to increase the difference observed between light and dark currents. The topography of the planar cell (not shown) is comparable to previous AFM characterization of planar $CuInSe_2$ samples[29], showing an array of roughly spherical grains with dimensions of ~100nm. Highly conductive areas were scattered unevenly throughout the film, and seemed to generally coincide with grain boundaries in the topographic image. The nanostructured sample, however, saw a larger amount of the surface exhibit photoconductivity, with high current areas localized around almost every PAH. It may be that the nanostructured nature of the PAH's yields similar electronic properties to the grain boundaries in the planar sample and thus maximizes the amount of photoelectrochemically active surface area.

Furthermore, the difference between the current values under illumination and in the dark was greater in the nanostructured sample, as shown in the histograms in Figure 3c and 3f. This implies that the nanostructured sample is less prone to internal shorts and that a greater fraction of the observed current is due to photoconductivity. To assess the photo-electrochemical performance of individual PAH's, we employed conductive AFM with a redox couple in solution phase. For these measurements, we used a $CuInSe_2$ device with a lower etching time such that the PAH's were still below the pore mouths of the alumina substrate. Solid state measurements of this device showed that direct electrical contact of the PAH's with the AFM tip was not possible. A drop of aqueous potassium ferricyanide solution was then placed on the

device and blotted with a Kimwipe™ immediately before AFM measurements. This sample construction and preparation method allowed residual solution to be retained in the pores of the PAH array and in pools on the surface as shown schematically in Figure 4a. This formed a nano-scale electrochemical cell where single or multiple PAH's act as the working electrode and the AFM tip acts as the counter electrode. We found that this technique was sensitive to the amount of solution present; too much and conductivity measurements were delocalized over the entire surface, too little and there were no pathways for ionic conduction and thus no conductivity.

Figure 4b shows an example of a conductive AFM image of the cell taken under illumination and -2V sample bias where individual PAH's can be imaged while figure 4c shows an image of a different area of the sample where the solution formed a pool which contacted multiple PAH's. Under these conditions we obtained delocalized I-V curves where several PAH's are measured simultaneously as shown in Figure 4d. This expectedly caused a large increase in the observed photocurrent to ~100pA due to multiple parallel PAH's being contacted by the solution, if we assume that each PAH exhibits similar photocurrents to those seen in the solid state then this indicates that we are measuring a group of ~100 units. We also observed that the photovoltage decreased to ~300mV likely due to internal shorts or PAH's with lower voltage being averaged into the measurement. To investigate this further, we conducted cyclic voltammetry measurements of the entire device, in an identical Fe^{2+}/ Fe^{3+} solution. This yielded an OCPV value of 310 mV and a decreased fill factor, similar to the delocalized AFM I-V measurement. We attribute this to

defective PAH's in the array which cause a significant voltage drop in the bulk device. This highlights the difference in observed performance when conducting measurements on a single element versus measurements on the ensemble. Comparison to the photovoltage of single elements thus gives an idea of the upper limits to device performance assuming an ideal device fabrication.

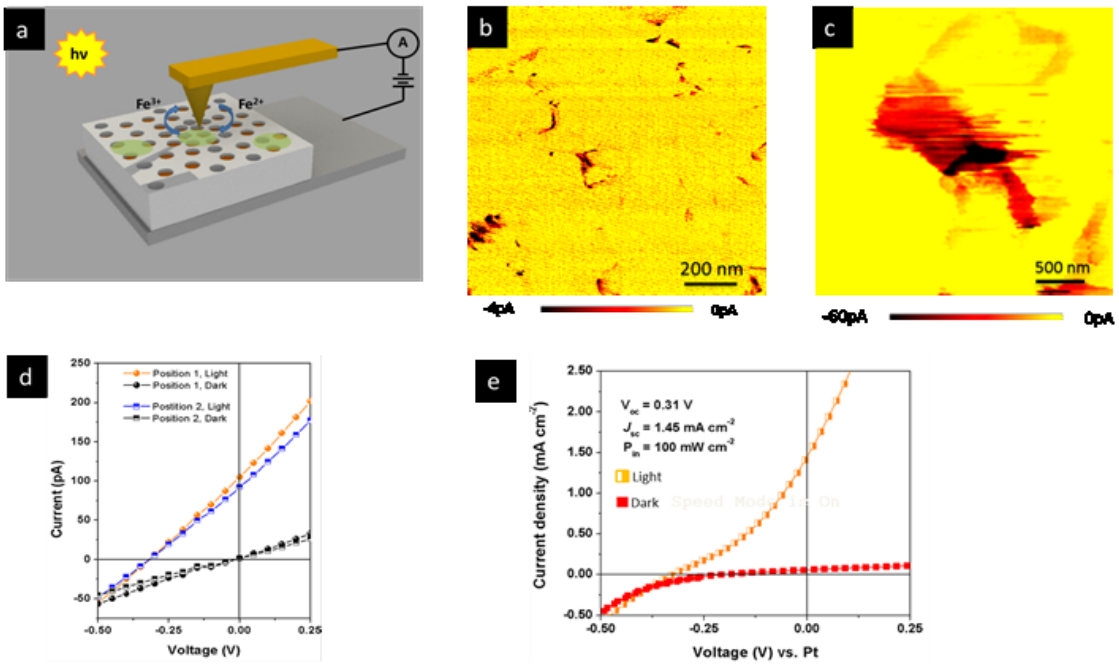

Figure 4: (a) Schematic representation of photoelectrochemical AFM setup. (b) Current image of a region showing single $CuInSe^2$ PAH structures with Fe^{2+}/Fe^{3+} solution present, under -2V bias and illumination. (c) Current image of a region showing Fe^{2+}/Fe^{3+} solution contacting several $CuInSe^2$ PAH structures, under -2V bias and illumination. (d) Solution I-V measurements taken from different locations on the sample in image (c) (e) Cyclic voltammogram of the entire PAH array immersed in Fe^{2+}/Fe^{3+} solution with and without illumination.

A1.4 Conclusions

In summary, we employed cp-AFM to investigate the performance of $CuInSe_2$/Au based photosynthetic electrochemical cells comprised of individual PAH elements (10^9units/m^2) deposited in nanoporous alumina. We found that after etching away the porous alumina, we could contact individual PAH elements and collect solid state photoconductive images and I-V curves. Compared to planar $CuInSe_2$ devices, PAH units showed larger photocurrents and photovoltages, implying fewer short circuit pathways in the PAH cell. A similar PAH device with a lower etch time allowed for PAH's to be contacted indirectly both individually and in small groups via the addition of a liquid electrolyte. We found that individual PAH elements have photovoltages which exceed that of these small groups and of the bulk device, implying that single faulty PAH's reduce device performance from its ideal value. We thus found that cp-AFM is an effective tool to quantify the voltage drop and short circuit current of individual PAH's and that comparison with bulk measurements gives useful insight into the effect of cell design and fabrication on overall performance. Solution-state AFM measurements allow for the investigation of the photoelectrochemical behavior of individual PAH's under conditions closely resembling operating conditions. This allows for different electrolytes to be investigated, and could provide a method to assess the durability of individual PAH elements in a corrosive environment. Future efforts will investigate in greater detail what effect parameters such as PAH dimensions, electrocatalyst and contacting layer composition, have on the spatial distribution of photocurrent in the cell; this will help

to develop a rational framework for increasing the overall solar to chemical efficiency of these devices.

References

(1) Fujishima, A.; Honda, K. Electrochemical Photolysis of Water at a Semiconductor Electrode. *Nature* **1972**, *238*, 37–+.

(2) Heller, A. Conversion of Sunlight into Electrical-Power and Photoassisted Electrolysis of Water in Photoelectrochemical Cells. *Accounts Chem. Res.* **1981**, *14*, 154–162.

(3) Nozik, A. J.; Memming, R. Physical Chemistry of Semiconductor-Liquid Interfaces. *J. Phys. Chem.* **1996**, *100*, 13061–13078.

(4) Khaselev, O.; Turner, J. A. A Monolithic Photovoltaic-Photoelectrochemical Device for Hydrogen Production via Water Splitting. *Science* **1998**, *280*, 425–427.

(5) Gratzel, M. Photoelectrochemical Cells. *Nature* **2001**, *414*, 338–344.

(6) Boettcher, S. W.; Spurgeon, J. M.; Putnam, M. C.; Warren, E. L.; Turner-Evans, D. B.; Kelzenberg, M. D.; Maiolo, J. R.; Atwater, H. A.; Lewis, N. S. Energy-Conversion Properties of Vapor-Liquid-Solid-Grown Silicon Wire-Array Photocathodes. *Science* **2010**, *327*, 185–187.

(7) Cattarin, S.; Guerriero, P.; Dietz, N.; Lewerenz, H. Electrodissolution and Corrosion of Cuins2 Photoanodes with Lamellar Morphology. *Electrochim. Acta* **1995**, *40*, 1041–1049.

(8) Hens, Z.; Gomes, W. P. On the Diffusion Impedance at Semiconductor Electrodes. *J. Phys. Chem. B* **1997**, *101*, 5814–5821.

(9) Mubeen, S.; Lee, J.; Singh, N.; Krämer, S.; Stucky, G. D.; Moskovits, M. An Autonomous Photosynthetic Device in Which All Charge Carriers Derive from Surface Plasmons. *Nat Nano* **2013**, *8*, 247–251.

(10) Malagù, C.; Guidi, V.; Stefancich, M.; Carotta, M. C.; Martinelli, G. Model for Schottky Barrier and Surface States in Nanostructured N-Type Semiconductors. *Journal of Applied Physics* **2002**, *91*, 808–814.

(11) Zhdanov, V. P. Nm-Sized Metal Particles on a Semiconductor Surface, Schottky Model, Etc. *Surface Science* **2002**, *512*, L331–L334.

(12) Oliver, R. A. Advances in AFM for the Electrical Characterization of Semiconductors. *Rep. Prog. Phys.* **2008**, *71*, 076501.

(13) Benstetter, G.; Biberger, R.; Liu, D. A Review of Advanced Scanning Probe Microscope Analysis of Functional Films and Semiconductor Devices. *Thin Solid Films* **2009**, *517*, 5100–5105.

(14) Chu, W.-H.; Chiang, H.-W.; Liu, C.-P. Sub-Band-Gap Photocurrent of an Individual Defective GaN Nanowire Measured by Conductive Atomic Force Microscopy. *Electrochem. Solid-State Lett.* **2011**, *14*, H294–H296.

(15) Masuda, H.; Takeuchi, M.; Takahashi, T. Local Photocurrent Detection on InAs Wires by Conductive AFM. *Ultramicroscopy* **2005**, *105*, 137–142.

(16) Coffey, D. C.; Reid, O. G.; Rodovsky, D. B.; Bartholomew, G. P.; Ginger, D. S. Mapping Local Photocurrents in Polymer/Fullerene Solar Cells with Photoconductive Atomic Force Microscopy. *Nano Letters* **2007**, *7*, 738–744.

(17) Dante, M.; Peet, J.; Nguyen, T.-Q. Nanoscale Charge Transport and Internal Structure of Bulk Heterojunction Conjugated Polymer/Fullerene Solar Cells by Scanning Probe Microscopy. *J. Phys. Chem. C* **2008**, *112*, 7241–7249.

(18) Beinik, I.; Kratzer, M.; Wachauer, A.; Wang, L.; Lechner, R. T.; Teichert, C.; Motz, C.; Anwand, W.; Brauer, G.; Chen, X. Y.; et al. Electrical Properties of ZnO Nanorods Studied by Conductive Atomic Force Microscopy. *Journal of Applied Physics* **2011**, *110*, 052005–052005–7.

(19) Riaz, M.; Song, J.; Nur, O.; Wang, Z. L.; Willander, M. Study of the Piezoelectric Power Generation of ZnO Nanowire Arrays Grown by Different Methods. *Advanced Functional Materials* **2011**, *21*, 628–633.

(20) Wang, Z. L.; Song, J. Piezoelectric Nanogenerators Based on Zinc Oxide Nanowire Arrays. *Science* **2006**, *312*, 242–246.

(21) Zhou, Y. S.; Wang, K.; Han, W.; Rai, S. C.; Zhang, Y.; Ding, Y.; Pan, C.; Zhang, F.; Zhou, W.; Wang, Z. L. Vertically Aligned CdSe Nanowire Arrays for Energy Harvesting and Piezotronic Devices. *ACS Nano* **2012**, *6*, 6478–6482.

(22) Tanaka, I.; Kamiya, I.; Sakaki, H.; Qureshi, N.; Allen, S. J.; Petroff, P. M. Imaging and Probing Electronic Properties of Self-Assembled InAs Quantum Dots by Atomic Force Microscopy with Conductive Tip. *Appl. Phys. Lett.* **1999**, *74*, 844–846.

(23) Zhang, H.; Miller, E. J.; Yu, E. T. Analysis of Leakage Current Mechanisms in Schottky Contacts to GaN and Al0.25Ga0.75N/GaN Grown by Molecular-Beam Epitaxy. *Journal of Applied Physics* **2006**, *99*, 023703.

(24) Warren, S. C.; Voïtchovsky, K.; Dotan, H.; Leroy, C. M.; Cornuz, M.; Stellacci, F.; Hébert, C.; Rothschild, A.; Grätzel, M. Identifying Champion Nanostructures for Solar Water-Splitting. *Nat Mater* **2013**, *12*, 842–849.

(25) Howell, S. L.; Padalkar, S.; Yoon, K.; Li, Q.; Koleske, D. D.; Wierer, J. J.; Wang, G. T.; Lauhon, L. J. Spatial Mapping of Efficiency of GaN/InGaN Nanowire Array Solar Cells Using Scanning Photocurrent Microscopy. *Nano Lett.* **2013**.

(26) Bard, A. J. Photoelectrochemistry. *Science* **1980**, *207*, 139–144.

(27) Macpherson, J. V.; Unwin, P. R. Combined Scanning Electrochemical-Atomic Force Microscopy. *Anal. Chem.* **2000**, *72*, 276–285.

(28) Shen, M.; Ishimatsu, R.; Kim, J.; Amemiya, S. Quantitative Imaging of Ion Transport through Single Nanopores by High-Resolution Scanning Electrochemical Microscopy. *J. Am. Chem. Soc.* **2012**, *134*, 9856–9859.

(29) Pathan, H. M.; Lokhande, C. D. Chemical Deposition and Characterization of Copper Indium Diselenide (CISe) Thin Films. *Applied Surface Science* **2005**, *245*, 328–334.

(30) Mubeen, S.; Singh, N.; Lee, J.; Stucky, G. D.; Moskovits, M.; McFarland, E. W. Synthesis of Chemicals Using Solar Energy with Stable Photoelectrochemically Active Heterostructures. *Nano Lett.* **2013**, *13*, 2110–2115.

(31) Lee, J.; Mubeen, S.; Ji, X.; Stucky, G. D.; Moskovits, M. Plasmonic Photoanodes for Solar Water Splitting with Visible Light. *Nano Lett.* **2012**, *12*, 5014–5019.

(32) Hernandez-Pagan, E. A.; Wang, W.; Mallouk, T. E. Template Electrodeposition of Single-Phase P- and N-Type Copper Indium Diselenide (CuInSe2) Nanowire Arrays. *ACS Nano* **2011**, *5*, 3237–3241.

(33) Leccabue, F.; Seuret, D.; Vigil, O. Sintered N-Cuinse2/Au Schottky Diode. *Appl. Phys. Lett.* **1985**, *46*, 853–855.

Appendix 2: Investigation of Amyloid-β Aggregation Mechanisms by Atomic Force Microscopy

A2.1 Introduction

Amyloids are a group of insoluble fibrous proteins which have been implicated in numerous diseases in the human body, including Alzheimer's disease, Type 2 Diabetes, and Parkinson's disease. The exact peptide varies for each disease, but in each case these peptides aggregate to form β sheets which then stack on top of each other to form fibrils and other larger scale structures. While the exact pathology of each disease is different, the aggregation process and subsequent formation of large structures in the intracellular space is thought to represent a major step in the progression of these diseases and the appearance of their symptoms.

This work focuses on the amyloid-β peptide, and to a lesser extent the tau peptide which are two specific peptides associated with Alzheimer's disease. Alzheimer's disease (AD) is a disease which affects millions of people, predominantly the elderly

and in its later stages leads to extreme memory loss and dementia. It is estimated that one in nine adults above the age of 65 has Alzheimer's, and as the proportion of the US population in this age range increases, the number of expected cases is expected to increase significantly.[1] The need for constant medical care in patients as well as the lost productivity and ability to live independently carries with it an enormous economic cost is in addition to the acute personal cost that this disease carries.

Amyloid-β (Aβ) is a peptide which is created when amyloid precursor protein, a transmembrane protein, is cleaved by secretase enzymes to form chains of 36-42 amino acid residues. The two most common are the 40 and 42 residue peptides, called Aβ-40 and Aβ-42 respectively, which have also been the subject of the majority of studies on the aggregation process. These peptides are then released into the intracellular medium where they can undergo the various aggregation processes which lead to AD symptoms. Once in the intracellular medium, these peptides form soluble oligomers, which are now thought to be the toxic form of the Aβ.[2,3] These oligomers are also thought to seed larger structure (fibril) growth, and possibly induce the formation of additional oligomers but this hypothesis is still being debated. [4–7]

The aggregation process is thought to be highly dependent on the amino acid sequence of the parent peptide, as different variants of the same peptide often show very different aggregation behavior. Much work has been carried out using fluorescent labels to track the aggregation process, circular dichroism to investigate

large aggregates[8,9], and theoretical modeling[10] to predict aggregation patterns. Despite all of this work, there are still many unanswered questions about the aggregation process. These include the exact progression from monomer Aβ, the effect of swapping various residues on the overall aggregation scheme, and how certain inhibitors are involved in slowing down or stopping this process. In addition, the exact nature of the cytotoxicity of soluble Aβ oligomers remains unknown. For this reason, experiments are required to probe various aspects of the aggregation process, with a focus on the early oligomerization events.

Atomic Force Microscopy has previously been demonstrated on Aβ samples and has proven a valuable technique for studying many aspects of the process. The high resolution of AFM and the ability to image the sample in an unaltered form allows for a direct view of the chain of events in the amyloid aggregation cascade.

This work is a collaboration with the Bowers' research group, and our first experiments used AFM to serve as a supporting technique to relate Ion Mobility Mass Spectrometry measurements to solution phenomena. For the relevant IM-MS data and a full analysis of all the work described here, the reader is directed to the relevant published work.[11–13] This appendix is meant to detail the AFM experiments and their role in these studies and provide a cursory description of the results obtained. Later work in this area involving high resolution imaging (A2.7) has employed AFM as a primary technique, and thus a more detailed discussion is provided.

A2.2 Experimental

These AFM experiments used tapping mode in air on our AFM instrument (Asylum MFP-3D). This generally involved a stiff (40 N/m) cantilever such as a MikroMasch XSC11 or NSC15. Samples were prepared by isolating Aß monomer by cleaving with hexafluoroisopropanol and then evaporating solvent and leaving a solid monomer film. This was then re-dissolved in acetate buffer solution to achieve the desired concentration and the resulting solution was incubated at air temperature for the desired amount of time. A 100μL aliquot was then deposited onto a freshly cleaved piece of mica which was then placed in a vacuum desiccator to dry off the solution. Large (20μm) scan sizes were typically used and several images were taken for every sample in order to insure that our images were representative for the entire sample. Later studies employed higher resolution AFM tips (Nanoworld SSS-NCT) in order to image smaller oligomers.

A2.3 Investigation of Molecular Inhibitors on Aβ Oligomer Growth

The first set of experiments we conducted was to investigate the effect of various molecular inhibitors on the Aβ aggregation process.[11] Two primary inhibitors were selected, epigallotechin Gallate (EGCG) and scyllo-inositol (SI). These are both inhibitor molecules which are under clinical trials and have been shown to inhibit some part of the aggregation process, but an understanding of its specific role or a mechanism for how it inhibits aggregation is not currently understood. For these experiments we used a shorter fragment of the Aβ peptide, Aβ 25-35 which has been

shown to be a crucial segment for oligomerization and exhibit similar neurotoxicity[14]. IM-MS experiments revealed that these inhibitors effectively stop the aggregation process selectively at certain stages in the process. By AFM we confirmed these findings by conducting imaging of Aβ samples with each inhibitor which are left incubated. The relative shortening of fibrils in both inhibitors, and especially in EGCG highlights its potential effectiveness as a therapeutic agent.

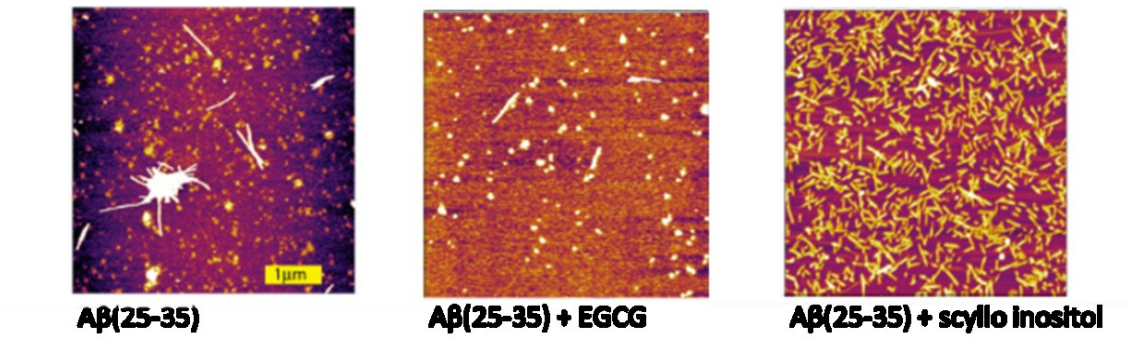

Figure A2.1 Topographic AFM Images of Aβ25-35 incubated with molecular inhibitors EGCG and scyllo-inositol deposited onto mica.

Subsequent experiments on EGCG were aimed at narrowing down the concentration range in which it is an effective inhibitor. We experimented with different ratios from 10:1 to 1:10 EGCG: Aβ25-35. What we determined was that this inhibitor is most effective in a 1:1 concentration and loses effectiveness when the concentration is considerably higher or lower. We interpret this as the need for a single molecule to bind to the β sheet in order to disrupt the packing process and

subsequent growth of fibrils. At high concentrations heterooligomers of EGCG and Aβ form, which we believe we are seeing in the image in figure A2.2d.

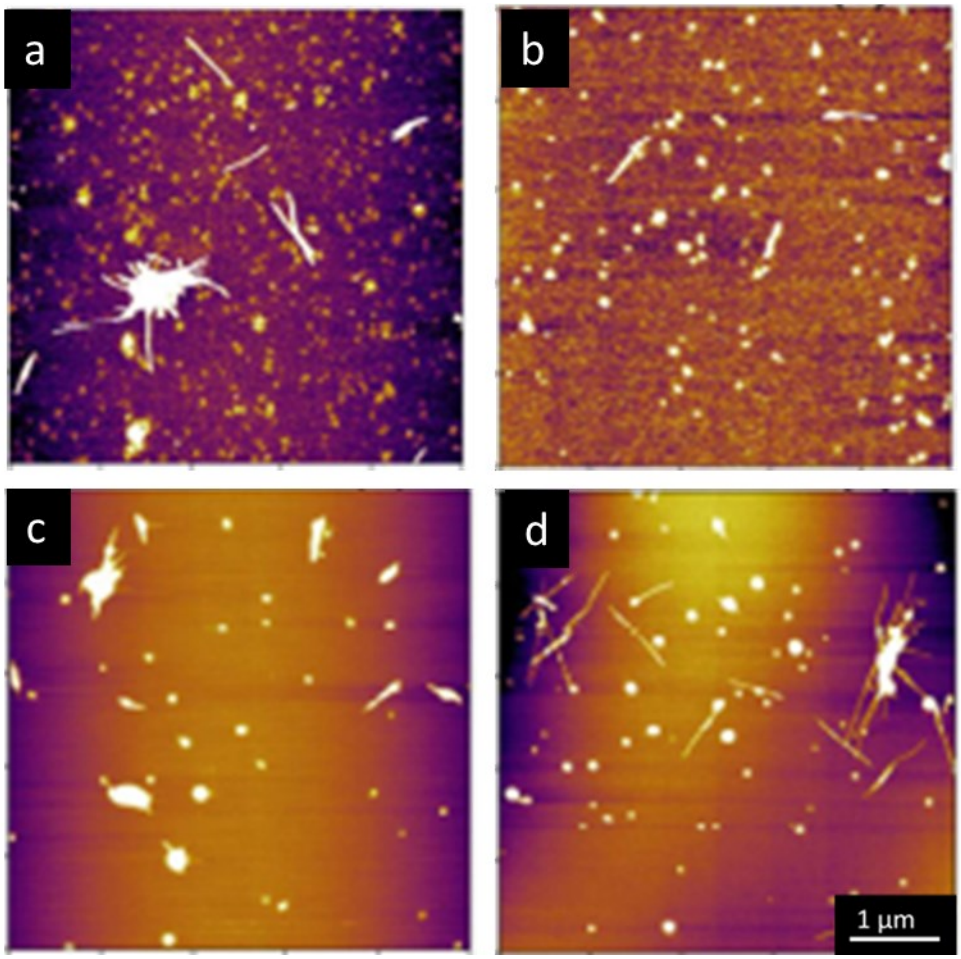

Figure A2.2 Topographic AFM Images of Aβ25-35 and EGCG at various molar ratios. (a) control (b)1:1 Aβ25-35: EGCG (c) 5:1 Aβ25-35: EGCG (d) 1:10 Aβ25-35:EGCG.

We next investigated the reversiblity of this effect by adding EGCG to a solution of Aβ which was already allowed to aggregate. Our studies showed that this process

actually does shift the equilibrium slightly towards shorter fibrils, as evidenced by our AFM observations.

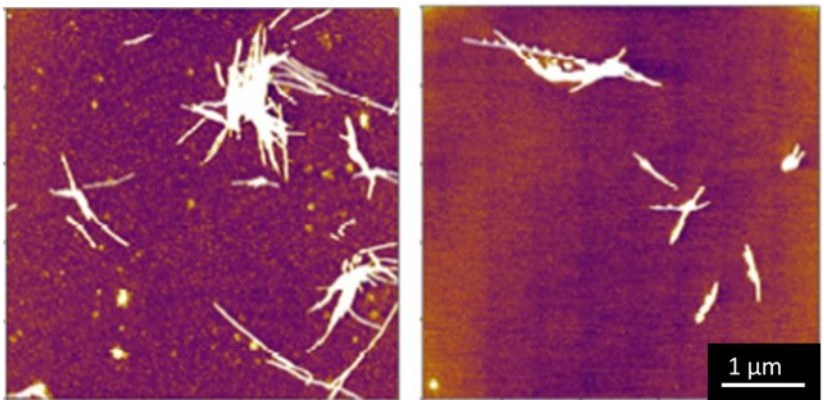

Figure A2.3 Topographic AFM Images of Aβ25-35 without (a) and with (b) EGCG added in a 1:1 ratio post-aggregation

Through our AFM experiments we have been able to show, alongside Mass spectrometry and simulation work that these two molecular inhibitors are highly effective at inhibitng Aβ fibrillation. We have also been able to learn a good deal about the exact mechanism by which this takes place and the concentrations of inhibitor necessary to achieve it.

A2.4 Examining the Effect of Mutations in the "Steric Zipper" by AFM

Towards more generally understanding oligomerization and fibrillization in amyloid proteins, we investigated the steric zipper motif, which is common in many such aggregation processes. This structure was first discovered by Nelson and

coworkers[15–17] and has been studied as a model system for amyloid aggregation. In this study we took the original peptide, NNQQNY, which is known to form the steric zipper and promote aggregation, and made a series of mutants where single or multiple amino acid residues are altered. Through these studies, we can see which residues are crucial to forming the zipper, and probe the nature of the interactions between residues which lead to this structure. Figure A2.4 shows the mutants which were examined in this study.

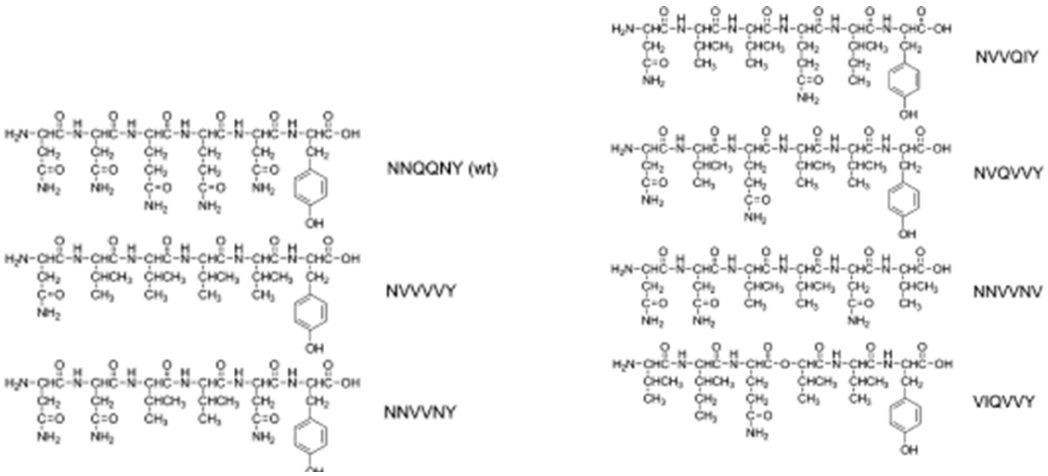

Figure A2.4 Chemical structures of NNQQNY and the six mutants used in this study

These mutants were chosen in such a way as to tune the hydrophobic interactions in each case. Since the steric zipper forms from hydrophobic interaction of this segment, varying the number and position of valine, asparagine, and glutamine residues provided a good way to vary hydrophobicity. All mutants maintained the tyrosine at the terminal position, as this is known to bind water and form the outside of the zipper.

By conducting AFM imaging on samples of each mutant that were allowed to aggregate in solution, we were able to see which residues are crucial to forming the steric zipper and thus allow for fibril formation. What we found is that asparagine and glutamine: the amide residues are necessary for fibrils to occur.

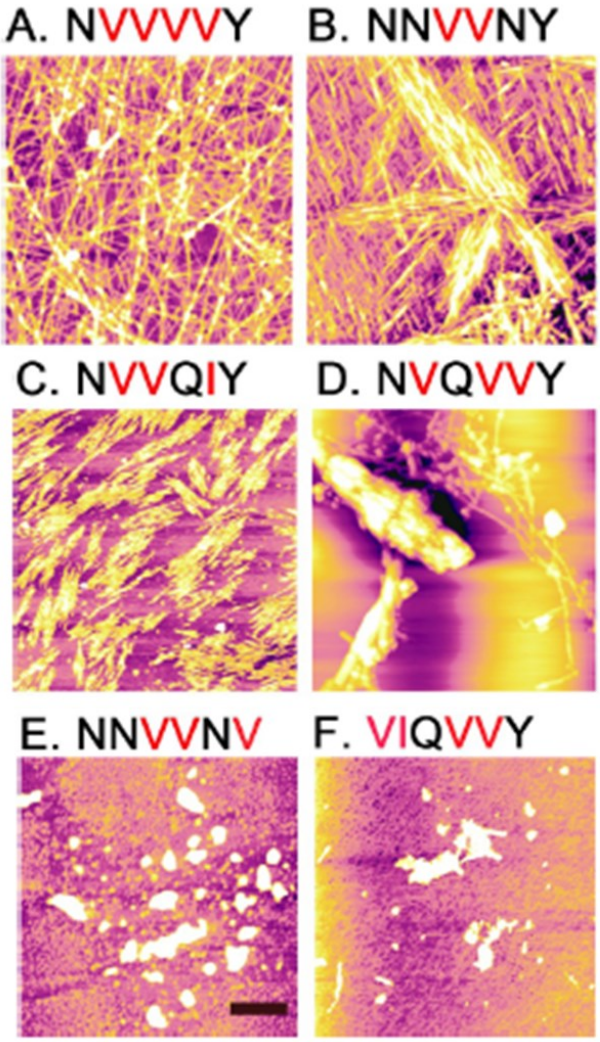

Figure A2.5 Representative topographic AFM images of each mutant deposited on mica from a 400 µM solution. The most prone to aggregation are shown on top, and the least prone are shown on bottom.

The aggregation we observe by AFM shows only moderately good agreement with modeling programs that were used to predict aggregation behavior. This may indicate that these models are oversimplifying the nature of the interaction between these peptides.

A2.5 Studies of co-aggregation between Aβ and tau

Another series of experiments was aimed at understanding the interplay between Aβ and tau, another protein which is implicated in Alzheimer's disease. Tau's function in a cell is to regulate microtubule formation, but in AD it is found to form neurofibrillary tangles in the intracellular medium. Work by other groups have suggested that these two peptides might co-aggregate or undergo some type of cooperative aggregation mechanism.[18–20]

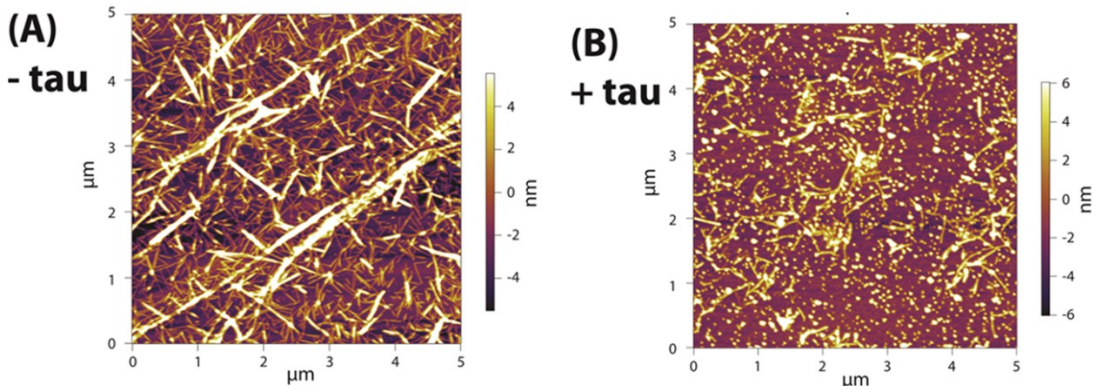

Figure A2.6 Topographic images of a 200µM Aβ solution, incubated with (A) and without (B) tau and deposited onto mica.

We found that introducing tau into a solution of Aβ greatly reduced the average size of fibrils, and increased the number of granular aggregates, implying

that tau actually works to prevent the formation of Aβ. The mechanism we think is responsible is the combination of Aβ and tau to form heterooligomers. This does decrease the average size of aggregates, but may serve as a further source of toxicity as tau which is bound in heterooligomers is no longer available to regulate microtubule growth. This could cause the overexpression of tau and the subsequent growth of neurofibrillary tangles. We also determined that tau could not de-aggregate Aβ fibrils once formed, likely due to the irreversibility or limited reversibility of this process.

A2.6 High Resolution Imaging of Aβ Oligomers

As mentioned in the introduction, the early stages of Aβ aggregation involve the formation of oligomers which are thought to be toxic and also play a role in the further aggregation into fibrils and large, quaternary structures. As such, there is great interest in unravelling the complex mechanism from Aβ monomers up to oligomers of several dozen units before the point at which fibril formation occurs. It has been theorized by other AFM studies that small, misfolded Aβ oligomers act as a seed which induces further misfolding and oligomerization, similar to a prion disease.[4,5] Previous AFM work has shown evidence of this type of behavior, and other studies have attempted to address exactly which types of oligomers are acting as seeds and what the mechanism is by which they seed further growth.

AFM represents a great tool to look at large Aβ structures such as fibrils,[6,21,21–29] and can also be used to gain information on the mechanical properties of these

structures. Using AFM as a technique to image smaller structures such as monomers and dimers carries with it significant challenges. AFM techniques by their nature have excellent vertical resolution, but their horizontal resolution is completely dependent on the radius of the AFM tip. Aβ monomers fold into a horseshoe shape and have an extremely small size (~3nm) in their folded conformation which makes them difficult to resolve unless extremely sharp AFM tips are used. The Smith group at SUNY Stony Brook used super sharp tips to collect images of Aβ 1-42 at the earliest stages of aggregation.[30] They were able to discern between various oligomers, such as monomers, dimers, tetramers, and hexamers and come up with a model for how their growth occurs. They theorize, in simple terms that dimers are what causes the growth of extended protofibrils(single β sheets) and subsequently fibrils (stacked β sheets), and that this proceeds independently of the formation of hexamers, dodecamers and higher MW oligomers. While they are able to achieve good resolution AFM images, some of their conclusions in this study do not agree well with other predictions for oligomer aggregation behavior.

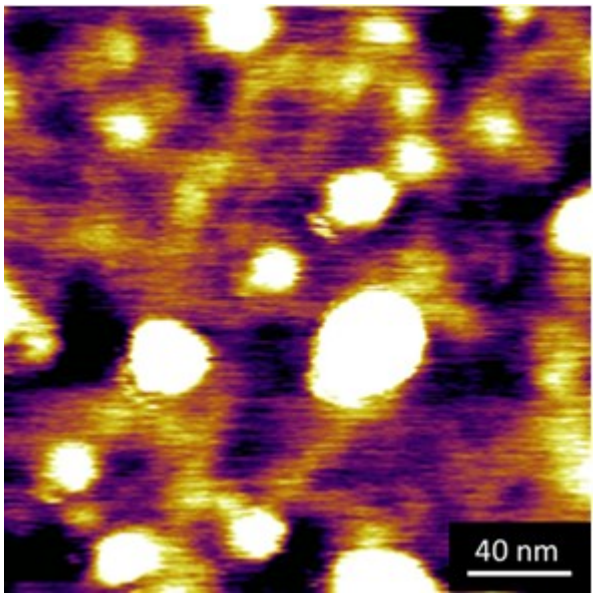

Figure A2.7 Topographic AFM image of Aβ 1-42 1μM solution incubated for 10 minutes and deposited onto mica. Image was collected using an XSC11 tip with nominal 10 nm radius.

For our first series of measurements, we sought to reproduce the experiments that this group conducted. In their work they imaged with a super sharp tip in buffer solution with a special scan loop designed to minimize contact forces. The first question we wanted to answer was if we could get similar resolution images in air, and if a super sharp tip was necessary. For these experiments, an Aβ 1-42 solution was prepared as described in the experimental section. For all experiments low concentrations (1-10 μm) were used as this has been shown to slow the aggregation process and allow for the earliest stages to be probed effectively. For our first images we used a standard XSC11 cantilever with a nominally 10nm radius tip, and discovered that while we could approach the resolution of these images, we were falling slightly short due to tip broadening. For the next batch, we used an identical

preparation and used a super sharp silicon tip. Optimization of imaging conditions was required in order to achieve high resolution and reduce tip wear, this included using a low drive amplitude to minimize contact forces and using careful tip engage procedures.

For these experiments we began with extremely short incubation times in order to determine the relative abundance of different types of oligomers initially. At times of 5 minutes or below, we see only small circular aggregates whose height is often 500 pm or 1 nm tall, correspond to 1 and 2 molecular layers of Aβ.

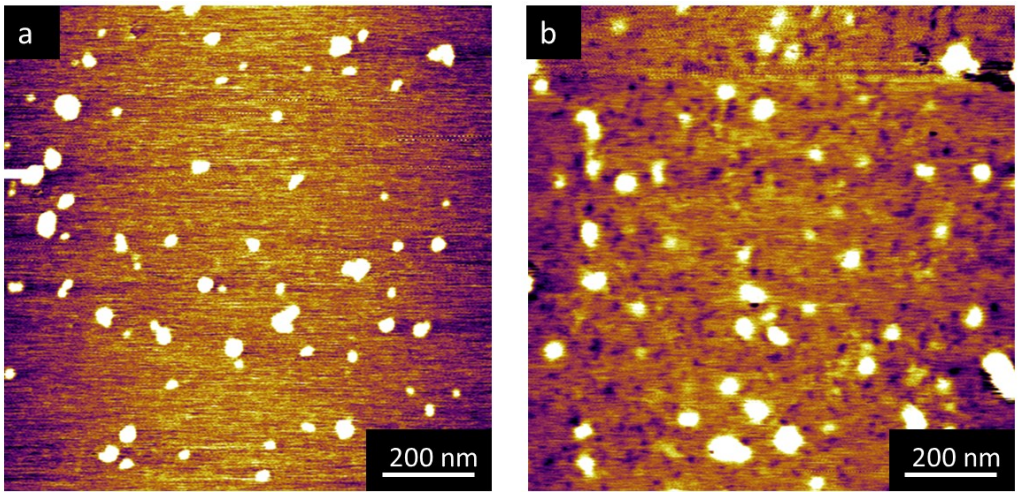

Figure A2.8 Topographic AFM image of Aβ 1-42 1μM solution incubated for 0 minutes (a) and 5 minutes (b) and deposited onto mica. This was collected using an SSS_NCT tip with nominal radius of 3 nm.

Figure A2.10 shows incubation times of 0 and 5 minutes, and shows there is no qualitative difference in oligomer size or distribution. It is also shows a limitation of our sample preparation technique; the buffer solution is allowed to dry off in the vacuum desiccator which was determined to take 2-3 minutes. This means that the nominally zero minute incubation is actually around 2 minutes and allows some small amount of oligomerization to occur.

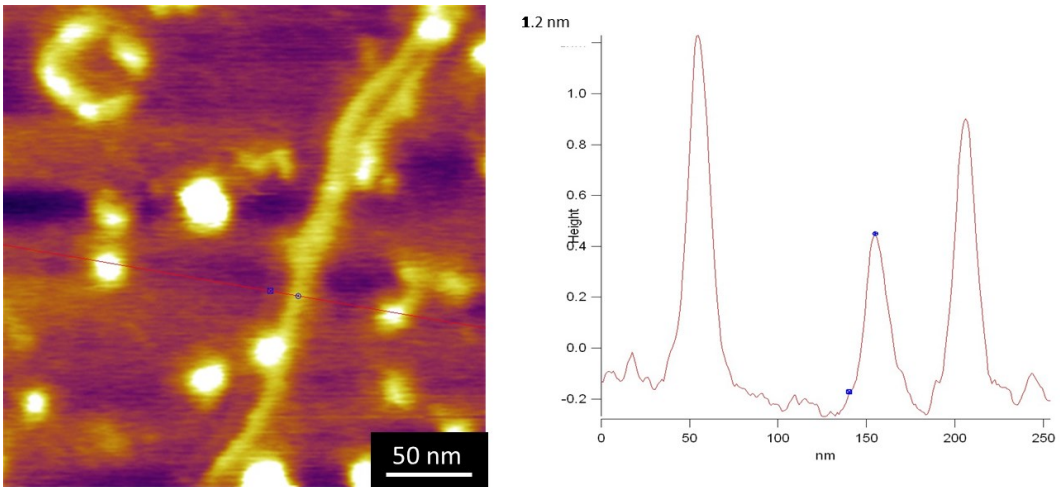

Figure A2.9 Topographic AFM image of Aβ 1-42 1μM solution incubated for 10 minutes and deposited onto mica. This was collected using an SSS_NCT tip with nominal radius of 3 nm. A corresponding line cut is shown which illustrates the height of various oligomers.

The image shown here used an extremely short aggregation time of 10 minutes and a low concentration of 1 μm. Under these conditions we see numerous circular features as before which appear to correspond loosely in size to monomers and dimers. We also see a feature whose height and width correspond to the expected dimensions of a protofibril; a collection of folded monomers which pack together end to end and form a single β sheet. Using the excellent vertical resolution of the

AFM, we are able to effectively discern how many monomer layers each feature has. We see that the minimum size is around 500 pm, which corresponds roughly to the expected height of a single beta sheet. This is lower than the Smith group's measurements, but this could be due to the difference in hydration state of these oligomers during imaging.

Another interesting feature, which we frequently observe in these images is a stacked oligomer (1 nm height) packed off center along the side of a protofibril (500 pm height) this is surprising, as these two forms of aggregation follow separate paths according to the model set forth by the Smith group. This may, however, indicate that these taller oligomers are seeding protofibril growth.

We next made a series of samples at different aggregation times from 0 to 60 minutes in order to view the time evolution of this process in its earliest stages. We see that whereas at 10 minutes we see a mixture of monomers, dimers, and protofibrils, at 20 minutes there is extensive protofibril growth, which covers much of the surface. At the same time we see the formation of tall, globular structures which are a few nm in height. Despite the continued growth of these new larger structures, there is still a large concentration of monomers, dimers and tetramers in solution as evidenced by the numerous small circular aggregates. This is consistent with the equilibrium that is supposedly established between these phases in solution

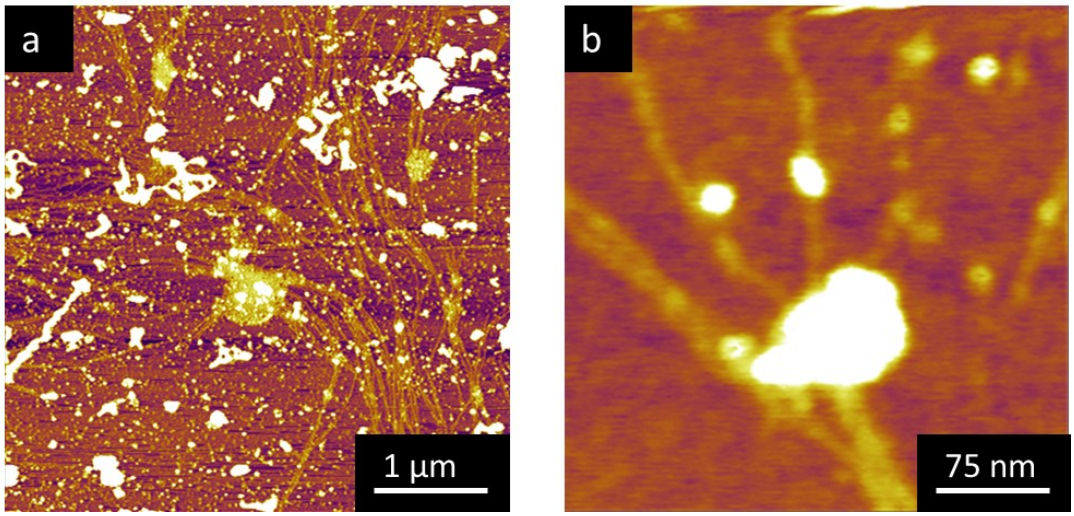

Figure A2.10 Topographic AFM image of Aβ 1-42 1µM solution incubated for 20 minutes and deposited onto mica. (a) large scale and (b) small scale.

At 60 minutes we see that the large globular aggregates are greatly increased in size and occurrence, and that there still exists numerous protofibrils across the surface. At this point, however, there are almost no isolated monomers or dimers visible implying that equilibrium has now shifted heavily in favor of larger structures. This is in sharp contrast to the Smith group which noticed predominantly hexamers and dodecamers at longer aggregation times.

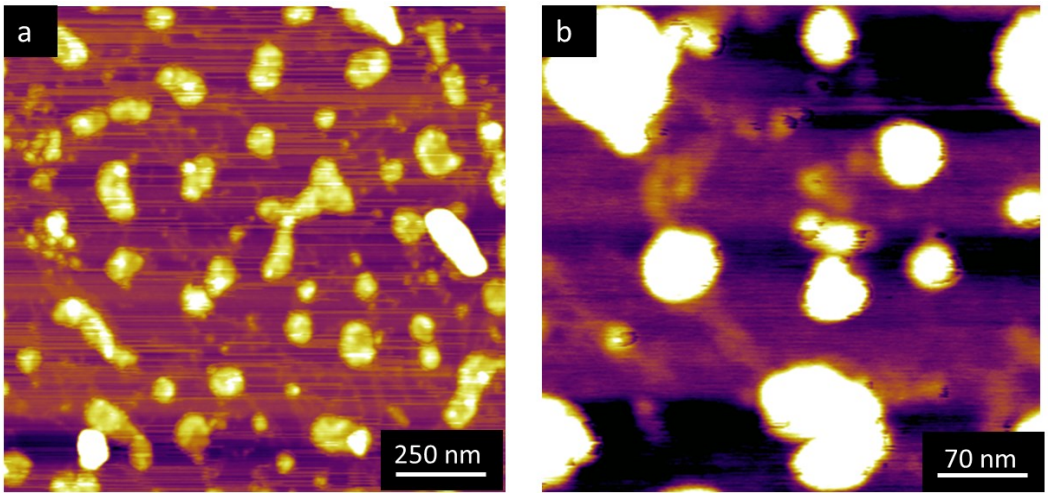

Figure A2.11 Topographic AFM image of Aβ 1-42 1μM solution incubated for 60 minutes and deposited onto mica. (a) large scale and (b) small scale

An effective way to visualize this data is to conduct a particle analysis of each image. If we take our 5 minute Aβ 1-42 image and graph the area of each particle versus its perimeter, we can get an index of how circular the particle is as shown in the scatter plot below. We see that at low sizes, all particles are essentially circular, while an increase in size causes a spreading between more rod-like oligomers and more circular oligomers. We can further see that rod-like aggregates reach a certain maximum area likely due to their small width and low resulting area. Most of the higher area aggregates we see are almost circular in shape. This type of plot represents an excellent way to compare AFM to Ion Mobility data, as IM-MS data determines the cross-sectional area of molecules in the gas phase and plots them against molecular weight. This gives a similar but complementary way to quantitatively analyze the shapes of oligomers.

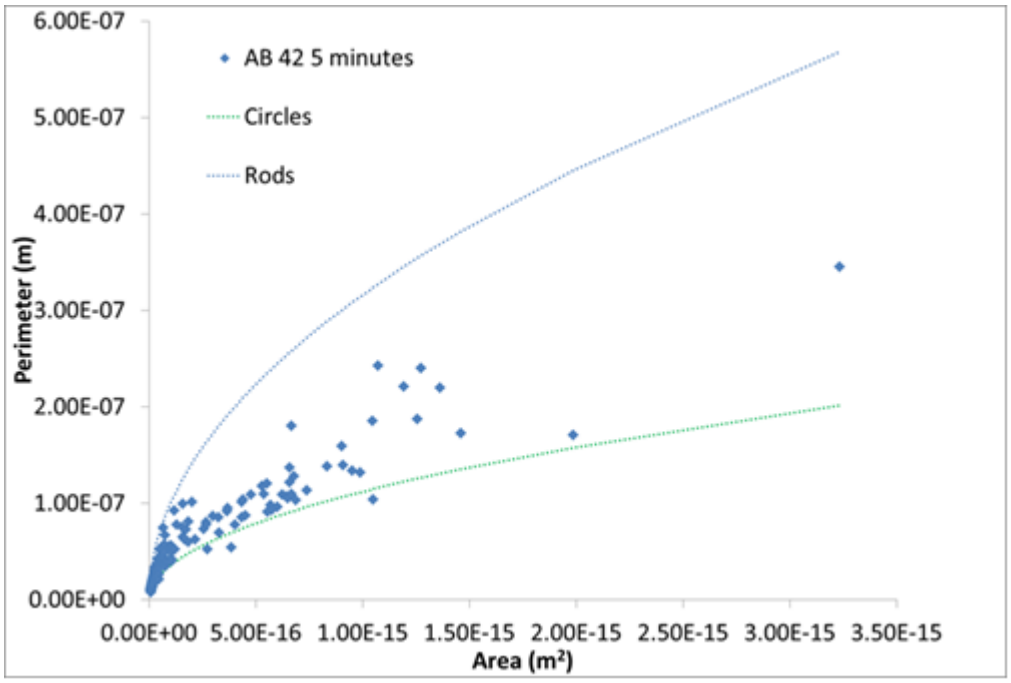

Figure A2.12 Plot of Perimeter versus Area for oligomers from an Aβ 1-42 image with a 5 minute incubation time. Lines corresponding to circular aggregates and 1:10 rods are plotted for comparison.

If we compare the average height of features in each image, we see an interesting progression. At 5 minutes there is a sharp peak around 500 pm representing the single beta sheet oligomers with a tail going out to higher heights caused by a small number of stacked oligomers. By 20 minutes this peak has shifted to 2 nm, indicating that stacked oligomers and large globular aggregates now make up the majority of the solution species. At 60 minutes, this peak is still at 2 nm, but we see that a short broad peak emerges at around 6 nm. This shows that there is an initial 2-D growth phase which is very rapid and that 3-D growth starts to happen slightly later in the process.

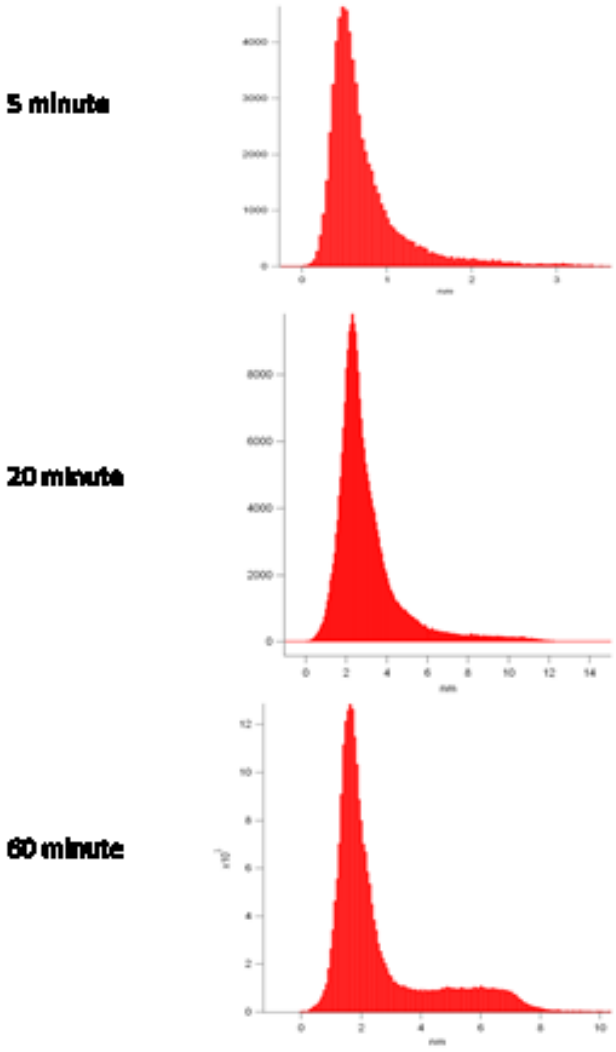

Figure A2.13 Histograms of height values from topographic AFM images of Aβ 1-42 at varying incubation times.

We next carried out a parallel set of experiments investigating the Aβ 1-40 oligomer. This oligomer has been shown to aggregate much more slowly in solution despite being only differing by missing two terminal residues.[31–33]

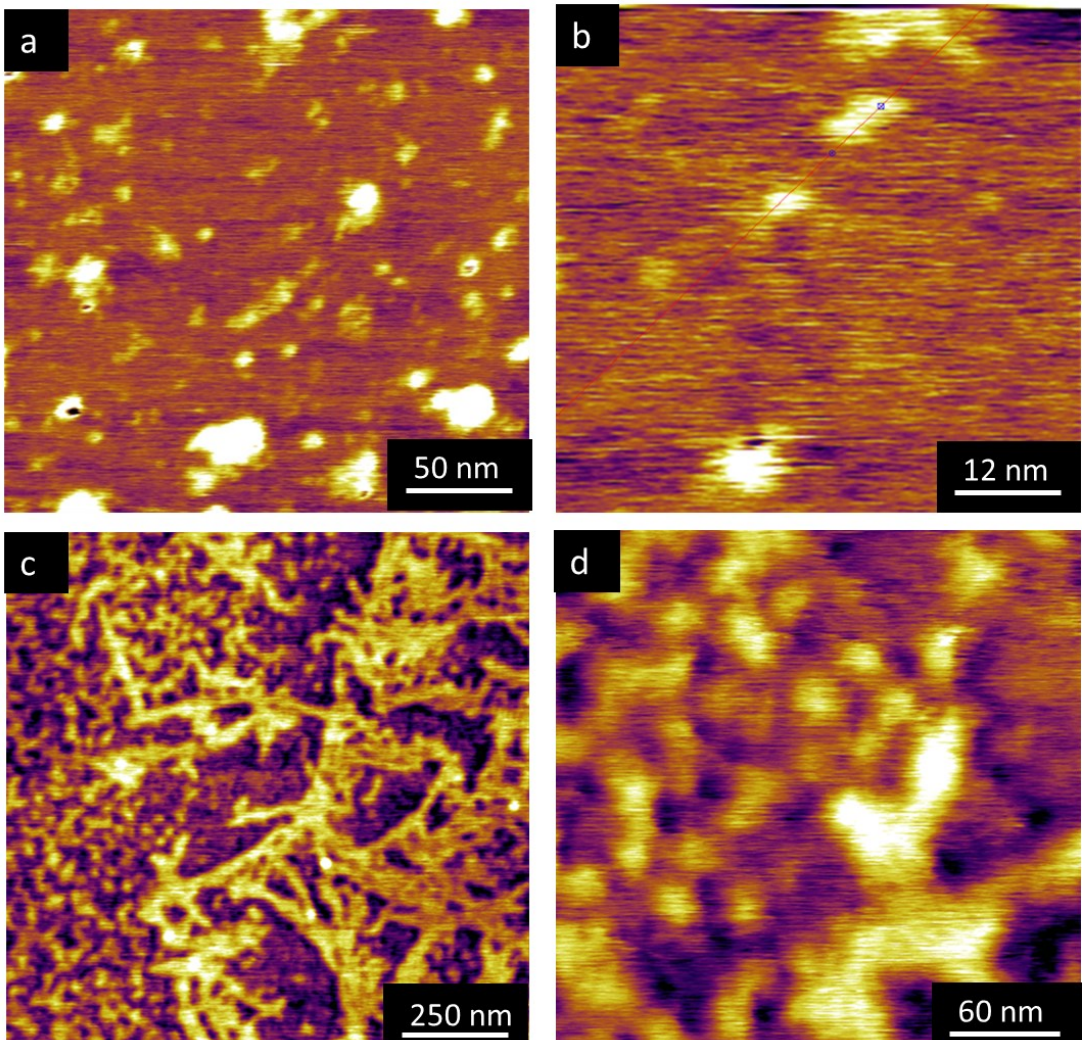

Figure A2.14 Representative topographic AFM images of 1μM Aβ 1-40 at 5 minutes (a,b) and at 30 minutes (c,d) incubation at different length scales.

What we see is that under identical conditions to Aβ 1-42, Aβ 1-40 undergoes a different type of growth. At 5 minutes, we see that there are almost exclusively single molecular layer oligomers (500 pm height) with a small number of 2 layer (1 nm) oligomers interspersed. It also appears that monomers and dimers are the most prevalent form, as opposed to the Aβ 1-42 sample where tetramers and higher MW

oligomers were common. At 30 minutes, this difference continues. Instead of forming tall globular aggregates, there is the formation of numerous protofibrils and extended β sheet structures. These facts all point to a slower aggregation process, and possibly one which favors 3-D growth less than Aβ 1-42.

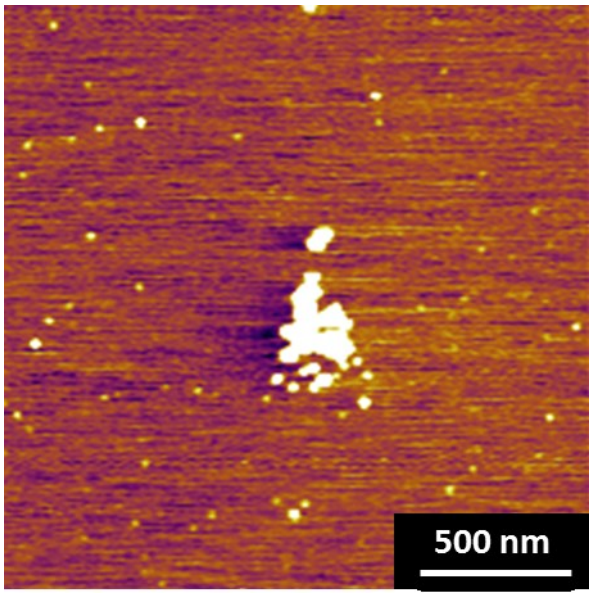

Figure A2.15 Topographic Image of 1μM Aβ 1-42 after 30 minutes where sample was subjected to a washing step post-deposition.

One key difference between our experiments and those conducted by the Smith group is that the Smith group washed residual solution off of their sample after allowing it to sit for 2 minutes. In our experiments, we simply dried the solution in a vacuum desiccator. This has its advantages and disadvantages; not washing the solution gives us a complete picture of soluble and insoluble oligomers without

selecting for their affinity for the mica surface, however, the drying process effectively concentrates the sample towards the end of drying which could alter the environment that monomers and oligomers see. To compare the two more directly, we made a series of samples using the Smith method and compared them to previous runs. Surprisingly, it appears that while small oligomers and large globular aggregates are still present, there are no protofibrils present when using this sample preparation. It may be that the unique shape of protofibrils causes them to stay suspended in solution, while more spherical oligomers are deposited on the mica. This apparent selection against protofibrils during the washing step indicates that this is not a preferred method for sample construction, and likely explains the lack of extended protofibrils in the Smith group's study.

A2.7 Conclusions and Future Directions

In this section, we have shown that AFM is an effective tool for imaging Aβ oligomers and fibrils. In combination with ion mobility mass spectrometry, it can obtain detailed conformational information on the early oligomerization events in a way that is difficult using other techniques. High resolution imaging is not without its challenges, but with careful control of imaging parameters allows a wealth of information to be extracted. Future experiments may employ imaging inside of buffer solution or under different pH conditions in order to more accurately observe the peptide in conditions resembling the intracellular medium. Another interesting avenue would involve depositing oligomers onto a lipid bilayer and observing this

interaction as it would more closely model in vivo aggregation. Imaging oligomerization in situ, while challenging, would provide an excellent view into the time-dependence of this process and shed new light into the kinetics of these processes.

There are also numerous other amyloid systems to investigate via AFM, and each system has its own characteristic aggregation behavior. Islet amyloid polypeptide (IAPP) which is implicated in type 2 diabetes represents one such system. The investigation of common motifs such as the steric zipper via high resolution imaging represents an interesting possibility by allowing us to understand mechanisms which are common in all amyloid proteins. Through better understanding of the aggregation process, it should be possible to design inhibitors and other treatments which can effectively delay or prevent the onset of these diseases.

References

(1) 2013 Alzheimer's Disease Facts and Figures - facts_figures_2013.pdf.

(2) Demuro, A.; Mina, E.; Kayed, R.; Milton, S. C.; Parker, I.; Glabe, C. G. Calcium Dysregulation and Membrane Disruption as a Ubiquitous Neurotoxic Mechanism of Soluble Amyloid Oligomers. *J. Biol. Chem.* **2005**, *280*, 17294–17300.

(3) Podlisny, M.; Ostaszewski, B.; Squazzo, S.; Koo, E.; Rydell, R.; Teplow, D.; Selkoe, D. Aggregation of Secreted Amyloid Beta-Protein into Sodium Dodecyl Sulfate-Stable Oligomers in Cell-Culture. *J. Biol. Chem.* **1995**, *270*, 9564–9570.

(4) Serem, W. K.; Bett, C. K.; Ngunjiri, J. N.; Garno, J. C. Studies of the Growth, Evolution, and Self-Aggregation of B-Amyloid Fibrils Using Tapping-Mode Atomic Force Microscopy. *Microsc. Res. Tech.* **2011**, *74*, 699–708.

(5) Bernhardt, N. A.; Berhanu, W. M.; Hansmann, U. H. E. Mutations and Seeding of Amylin Fibril-Like Oligomers. *J. Phys. Chem. B* **2013**, *117*, 16076–16085.

(6) Harper, J. D.; Lieber, C. M.; Lansbury Jr, P. T. Atomic Force Microscopic Imaging of Seeded Fibril Formation and Fibril Branching by the Alzheimer's Disease Amyloid-B Protein. *Chemistry & Biology* **1997**, *4*, 951–959.

(7) Wu, J. W.; Breydo, L.; Isas, J. M.; Lee, J.; Kuznetsov, Y. G.; Langen, R.; Glabe, C. Fibrillar Oligomers Nucleate the Oligomerization of Monomeric Amyloid Beta but Do Not Seed Fibril Formation. *J. Biol. Chem.* **2010**, *285*, 6071–6079.

(8) Kirkitadze, M. D.; Condron, M. M.; Teplow, D. B. Identification and Characterization of Key Kinetic Intermediates in Amyloid Beta-Protein Fibrillogenesis. *J. Mol. Biol.* **2001**, *312*, 1103–1119.

(9) Uversky, V. N.; Fink, A. L. Conformational Constraints for Amyloid Fibrillation: The Importance of Being Unfolded. *BBA-Proteins Proteomics* **2004**, *1698*, 131–153.

(10) Friedman, R. Aggregation of Amyloids in a Cellular Context: Modelling and Experiment. *Biochem. J.* **2011**, *438*, 415–426.

(11) Bleiholder, C.; Do, T. D.; Wu, C.; Economou, N. J.; Bernstein, S. S.; Buratto, S. K.; Shea, J.-E.; Bowers, M. T. Ion Mobility Spectrometry Reveals the Mechanism of Amyloid Formation of Aβ(25-35) and Its Modulation by Inhibitors at the Molecular Level: Epigallocatechin Gallate and Scyllo-Inositol. *J. Am. Chem. Soc.* **2013**.

(12) Do, T. D.; Economou, N. J.; LaPointe, N. E.; Kincannon, W. M.; Bleiholder, C.; Feinstein, S. C.; Teplow, D. B.; Buratto, S. K.; Bowers, M. T. Factors That Drive Peptide Assembly and Fibril Formation: Experimental and Theoretical Analysis of Sup35 NNQQNY Mutants. *J. Phys. Chem. B* **2013**, *117*, 8436–8446.

(13) Do, T. D.; LaPointe, N. E.; Economou, N. J.; Buratto, S. K.; Feinstein, S. C.; Shea, J.-E.; Bowers, M. T. Effects of pH and Charge State on Peptide

Assembly: The YVIFL Model System. *J. Phys. Chem. B* **2013**, *117*, 10759–10768.

(14) Mattson, M.; Cheng, B.; Davis, D.; Bryant, K.; Lieberburg, I.; Rydel, R. Beta-Amyloid Peptides Destabilize Calcium Homeostasis and Render Human Cortical-Neurons Vulnerable to Excitotoxicity. *J. Neurosci.* **1992**, *12*, 376–389.

(15) Sawaya, M. R.; Sambashivan, S.; Nelson, R.; Ivanova, M. I.; Sievers, S. A.; Apostol, M. I.; Thompson, M. J.; Balbirnie, M.; Wiltzius, J. J. W.; McFarlane, H. T.; et al. Atomic Structures of Amyloid Cross-Beta Spines Reveal Varied Steric Zippers. *Nature* **2007**, *447*, 453–457.

(16) Nelson, R.; Sawaya, M. R.; Balbirnie, M.; Madsen, A. O.; Riekel, C.; Grothe, R.; Eisenberg, D. Structure of the Cross-Beta Spine of Amyloid-like Fibrils. *Nature* **2005**, *435*, 773–778.

(17) Nelson, R.; Eisenberg, D. Recent Atomic Models of Amyloid Fibril Structure. *Curr. Opin. Struct. Biol.* **2006**, *16*, 260–265.

(18) Miller, Y.; Ma, B.; Nussinov, R. Synergistic Interactions between Repeats in Tau Protein and A Beta Amyloids May Be Responsible for Accelerated Aggregation via Polymorphic States. *Biochemistry* **2011**, *50*, 5172–5181.

(19) Raz, Y.; Miller, Y. Interactions between A Beta and Mutated Tau Lead to Polymorphism and Induce Aggregation of A Beta-Mutated Tau Oligomeric Complexes. *PLoS One* **2013**, *8*.

(20) Wasiak, T.; Ionov, M.; Nieznanski, K.; Nieznanska, H.; Klementieva, O.; Granell, M.; Cladera, J.; Majoral, J.-P.; Caminade, A. M.; Klajnert, B. Phosphorus Dendrimers Affect Alzheimer's (A beta(1-28)) Peptide and MAP-Tau Protein Aggregation. *Mol. Pharm.* **2012**, *9*, 458–469.

(21) Adamcik, J.; Jung, J.-M.; Flakowski, J.; De Los Rios, P.; Dietler, G.; Mezzenga, R. Understanding Amyloid Aggregation by Statistical Analysis of Atomic Force Microscopy Images. *Nat Nano* **2010**, *5*, 423–428.

(22) Parbhu, A.; Lin, H.; Thimm, J.; Lal, R. Imaging Real-Time Aggregation of Amyloid Beta Protein (1–42) by Atomic Force Microscopy. *Peptides* **2002**, *23*, 1265–1270.

(23) Knowles, T. P. J.; Buehler, M. J. Nanomechanics of Functional and Pathological Amyloid Materials. *Nat Nano* **2011**, *6*, 469–479.

(24) Adamcik, J.; Berquand, A.; Mezzenga, R. Single-Step Direct Measurement of Amyloid Fibrils Stiffness by Peak Force Quantitative Nanomechanical Atomic Force Microscopy. *Applied Physics Letters* **2011**, *98*, 193701.

(25) Qiang, W.; Kelley, K.; Tycko, R. Polymorph-Specific Kinetics and Thermodynamics of B-Amyloid Fibril Growth. *J. Am. Chem. Soc.* **2013**, *135*, 6860–6871.

(26) Kurouski, D.; Lu, X.; Popova, L.; Wan, W.; Shanmugasundaram, M.; Stubbs, G.; Dukor, R. K.; Lednev, I. K.; Nafie, L. A. Is Supramolecular Filament Chirality the Underlying Cause of Major Morphology Differences in Amyloid Fibrils? *J. Am. Chem. Soc.* **2014**, *136*, 2302–2312.

(27) Zhou, X.; Zhang, Y.; Zhang, F.; Pillai, S.; Liu, J.; Li, R.; Dai, B.; Li, B.; Zhang, Y. Hierarchical Ordering of Amyloid Fibrils on the Mica Surface. *Nanoscale* **2013**, *5*, 4816–4822.

(28) Harper, J. D.; Wong, S. S.; Lieber, C. M.; Lansbury Jr, P. T. Observation of Metastable Aβ Amyloid Protofibrils by Atomic Force Microscopy. *Chemistry & Biology* **1997**, *4*, 119–125.

(29) Adamcik, J.; Mezzenga, R. Study of Amyloid Fibrils via Atomic Force Microscopy. *Current Opinion in Colloid & Interface Science* **2012**, *17*, 369–376.

(30) Mastrangelo, I. A.; Ahmed, M.; Sato, T.; Liu, W.; Wang, C.; Hough, P.; Smith, S. O. High-Resolution Atomic Force Microscopy of Soluble Aβ42 Oligomers. *Journal of Molecular Biology* **2006**, *358*, 106–119.

(31) Hou, L. M.; Shao, H. Y.; Zhang, Y. B.; Li, H.; Menon, N. K.; Neuhaus, E. B.; Brewer, J. M.; Byeon, I. J. L.; Ray, D. G.; Vitek, M. P.; et al. Solution NMR Studies of the A beta(1-40) and A beta(1-42) Peptides Establish That the met35 Oxidation State Affects the Mechanism of Amyloid Formation. *J. Am. Chem. Soc.* **2004**, *126*, 1992–2005.

(32) Jarrett, J.; Berger, E.; Lansbury, P. The Carboxy Terminus of the Beta-Amyloid Protein Is Critical for the Seeding of Amyloid Formation - Implications for the Pathogenesis of Alzheimers-Disease. *Biochemistry* **1993**, *32*, 4693–4697.

(33) Snyder, S.; Ladror, U.; Wade, W.; Wang, G.; Barrett, L.; Matayoshi, E.; Huffaker, H.; Krafft, G.; Holzman, T. Amyloid-Beta Aggregation - Selective-

Inhibition of Aggregation in Mixtures of Amyloid with Different Chain Lengths. *Biophys. J.* **1994**, *67*, 1216–1228.